DESIGN AND DEVELOPMENT OF COMPOSITE ENCLOSURE WITH VARIABLE THERMAL CONDUCTIVITY FOR LI-ION BATTERY MODULE

Thesis submitted in accordance with the requirements of
Brunel University London for the Degree of Doctor of Philosophy

By

Thamasha Samarasinghe

College of Engineering, Design and Physical Sciences,
Brunel University London
June 2024

ABSTRACT

Thermal management of batteries can be accomplished through active or passive built in cooling sources. Air, liquid (mainly water) and phase-changing materials or a combination of these three methods are used in existing thermal management systems.

Current solutions with active cooling are adding weight and complexity to EV and HEV batteries. The involvement of phase-changing materials (PCMs) as a passive cooling technique is also adding to the complexity, weight, and the additional thermal resistance in the heat dissipation process of batteries.

An innovative idea for a composite casing for car batteries is considered in this project. The composite casing will have variable thermal conductivity, defined by the local volume fraction of carbon fibres and other conductive elements (including copper pins) within the composite. The selectively high thermal conductivity in areas of the casing will create "thermal avenues" close to the hot areas of the battery in order to provide passive heat dissipation in the areas needed the most. The composite casing will provide a low weight, simple thermal management solution that requires minimum maintenance.

A 3D model of a Li-ion battery single cell was developed and used to evaluate several geometries of a battery module currently being used by battery manufacturers. Heat transfer simulations are validated by experimental results from a custom jig that emulates the battery module arrangement. Heating elements of similar size and power/heat output to individual cells have been used for the experiments.

The composite casing was manufactured using the resin infusion method, and copper pins were inserted into the significant locations of the enclosure during the process of resin infusion. The metallic pin arrangement was validated experimentally with the bespoke test rig. Simulation and experimental results are in better agreement with each other for the scenarios of the composite enclosure and the composite enclosure with the copper pin arrangement.

Furthermore, the simulation results, IR thermography results, and experimental results confirmed that the copper pins arrangement is an effective solution to conduct the heat that is accumulated inside the enclosure to the outside without the use of any kind of active cooling methods such as air-cooling or water cooling.

To my Parents, in gratitude

ACKNOWLEDGEMENTS

TABLE OF CONTENTS

List of Tables

List of Figures

Abbreviations

Abbreviation	Description
EV	Electric Vehicles
HEV	Hybrid Electric Vehicles
Li-ion	Lithium-ion
SLI	Starting, Lighting and Ignition
PCM	Phase Changing Materials
CFD	Computational Fluid Dynamics
ECM	Equivalent Circuit Modelling
OCV	Open Circuit Voltage
SoC	State of Charge
LCM	Liquid Composite Molding
RTM	Resin Transfer Molding
RI	Resin Infusion
SRIM	Structural Reaction Injection Molding
CNT	Carbon Nanotubes
ANOVA	Analysis of Variance
CFRP	Carbon Fibre Reinforced Polymer
CI	Confidence Interval
PTFE	Polytetrafluorethylene
RH	Relative Humidity

1 Introduction

Interest in electric vehicles (EVs) and hybrid electric vehicles (HEVs) is being fuelled by global worries about reducing reliance on fossil fuels and, ultimately, emitting less harmful emissions. The energy storage system used by EVs and HEVs, such as batteries, affects how well they function. In EVs and HEVs, battery performance affects a number of characteristics, including travel distance, acceleration, and charge acceptance during regenerative brake recovery. It is vital to maximise the factors that affect a battery-powered vehicle's efficiency because the cost of the batteries, their life cycle, and their durability have an impact on the vehicle's performance.

Due to its many benefits, including its low self-discharge rate, high efficiency, and high power-to-weight and energy-to-weight ratios, the lithium-ion (Li-ion) battery is regarded as the top candidate for an EV and HEV power source. [1]. Li-ion batteries are frequently used in portable electronics and other devices, in addition to EVs and HEVs. However, a Li-ion battery's thermal performance restricts its long-term stability and safety features because the battery's ideal temperature is normally between 30-40°C [2]. Since an uneven temperature distribution results in electrically imbalanced modules and reduces battery life, battery modules must be operated at a constant temperature. In addition, improper heat regulation in a cell might result in thermal runaway. Uncontrolled heat dispersion poses significant fire and explosive risks.

The impact of temperature on battery packs is a topic of extensive research. More than 5 million automobiles were used in Anderson's research on starting, lighting, and ignition (SLI) batteries. [3]. His research shows that temperature and charge efficiency have an adverse relationship with the life cycle of SLI lead-acid batteries. Furthermore, even at temperatures close to ambient, both Li-ion and lead-acid battery systems require thermal regulation, according to studies by Gomez et al. [4]. Dickinson and Swan [5] examined the performance and lifespan of many Li-ion battery packs and discovered that the temperature difference between modules lowers the capacity of the entire pack. The inverse link between charge acceptance rates and temperature was corroborated by Sharpe and Conell [6] in their study of the impact of temperature on the charging of both Li-ion and lead-acid batteries. The efficiency and maximum working power of lead-acid and lithium-ion batteries both rise in the 30°C to 40°C and -26°C to 65°C temperature ranges, respectively, according to Wicks and Doane [7] . According to the findings of the aforementioned investigations, a battery pack's performance must be increased through precise temperature regulation.

An integrated source that offers cooling can be active or passive to manage the thermal state of the batteries. Active control techniques compel cooling media to circulate around the battery pack using built-in devices. Heat is transported from the battery pack's surrounding ambient environment when passive cooling techniques are used. Air, liquids (mostly water), phase-changing materials (PCMs), or a combination of these three are used in existing temperature-control systems.

Batteries for EVs and HEVs today are heavier and more complicated due to active cooling systems. Mainly the active systems utilise mechanisms such as coolant pumps, radiators, hoses, and sometimes even additional heat exchangers or chillers to actively regulate the temperature of the battery pack. These components add weight to the vehicle compared to passive systems. In addition to that, the coolant itself also contributes to the weight of the system too. Furthermore, the structural reinforcement needed to support the additional weight of the active cooling components can also contribute to the overall weight of the vehicle.

Although the Phase -changing material (PCM) are used in battery enclosures as the passive cooling technique, those enclosures present challenges due to their limited thermal conductivity and the heat absorption capacity, potentially hindering rapid heat dissipation during high-demand scenarios. Also, maintaining a precise temperature control can be difficult, as PCM systems operate within specific temperature ranges and may struggle to adapt to varying ambient conditions or usage patterns. Additionally, the added weight and volume of PCM materials impact vehicle design, and thermal cycling over time can lead to material degradation.

By considering the limitations which are associated with the existing battery cooling technologies, the current study offers a fresh concept for a battery pack with greater control: depending on the volume proportion of carbon fibres and other conductive materials inside the composite, a composite case with variable thermal conductivity. In order to offer passive heat dissipation where it is most needed, the selectively high conductivity in certain portions of the casing will form "thermal avenues" close to the hot areas of the battery. The composite casing will offer a lightweight, straightforward thermal management solution that needs no upkeep.
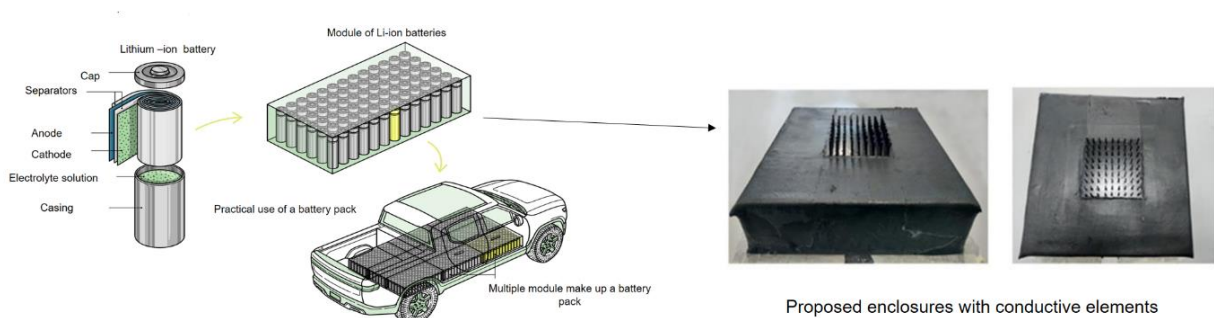
Figure 1.1. Schematic diagram of EV battery pack and corresponding cooling system

As indicated in Figure 1.1, in the research it is mainly discussed about the cylindrical battery cell and a single battery module. Mainly the external enclosure with the conductive elements for the battery module design and development is discussed in detail.

Real-world statistics on thermal dissipation efficiency in EV Li-ion batteries vary based on factors like battery pack design, vehicle type, and operating conditions. Generally, Li-ion battery materials exhibit thermal conductivities ranging from 1 to 5 W/(m·K), with higher values indicating better heat conduction [2]. Heat transfer coefficients between battery cells and cooling systems can span 10 to over 500 W/(m^2·K), with liquid cooling systems typically offering superior efficiency. Thermal resistance in battery packs typically falls between 0.1 to 1 K/W, reflecting the pack's resistance to heat flow [2]. Ongoing research aims to enhance thermal dissipation efficiency through advanced cooling materials, optimised designs, and active temperature management systems. These improvements are crucial for maintaining battery temperature within safe limits during normal driving and fast charging, ensuring optimal performance, longevity, and safety of EV Li-ion batteries.

1.1 Research hypothesis

A composite casing with areas of high thermal conductivity can provide adequate passive cooling to a Li-ion battery module.

1.1.1 Aim

Design and develop a composite enclosure with variable thermal conductivity to transfer the heat generated from the battery module to the outside.

1.1.1.1 Objectives

- Develop a heat transfer model for a Li-ion battery module which has a composite casing with variable thermal conductivity.

- Design and build an experimental rig that emulates the operation of a Li-ion battery module in order to validate the heat transfer model.
- Design and fabricate composite enclosures with variable thermal conductivity.
- Use the experimental rig to test the research hypothesis.

1.2   Thesis outline

The thesis is structured in 5 chapters. Chapter 2 reports current state of the art on the topics of heat transfer models for battery cells, heat transfer through composite materials and methods to improve the thermal management of battery casings. Chapter 3 describes the development of a heat transfer model for Li-ion battery module. Chapter 4 presents the experimental setup and tests performed for the validation of the heat transfer model for Li-ion battery module using a metallic enclosure. Chapter 5 describes the design and manufacturing of the novel composite enclosure with and without additional conductive elements for improved thermal conductivity. In the same chapter, the experimental results from the tests of the composite enclosure and comparison with the simulation of the composite enclosure performance is reported. In every chapter, a dedicated section where results are discussed is provided. Finally, the overall discussion and conclusions are summarised in Chapter 6 alongside recommendations for further research in the field.

1.3   Contribution to the new knowledge

The contribution to new knowledge in this study lies in the exploration and development of a novel concept for improving the thermal management of battery packs in electric vehicles (EVs) and hybrid electric vehicles (HEVs). By addressing the limitations of existing battery cooling technologies, the study proposes the use of a composite battery pack enclosure with variable thermal conductivity. This composite casing is designed to create "thermal avenues" with selectively high conductivity in areas where heat dissipation is most needed, offering a lightweight and maintenance-free solution for passive heat management. The research aims to develop a comprehensive understanding of heat transfer dynamics in Li-ion battery modules, validate the proposed concept through experimental testing, and provide insights into the design and fabrication of composite enclosures. The study's findings have implications for enhancing the thermal efficiency, performance, and safety of EV and HEV battery systems, ultimately contributing to advancements in electric vehicle technology and sustainable transportation.

2 Literature review

2.1 Heat transfer models for battery cells

Due to enthalpy changes, resistive heating inside the cell, and electrochemical polarisation, batteries produce heat during charge and discharge. Entropic heat is the name given to the heat because it results from the entropy that is brought on by electrochemical reactions. The difference between the operational potential and the cell-open circuit potential is known as the polarisation. The charge transfer process is hampered by a resistance at the solid electrolyte interface. "Active polarisation heat" is the term for the energy required to break through the barrier during the intercalation and de-intercalation of lithium. The transport resistance in the solid and electrolyte phases is what causes the energy loss known as the ohmic, or resistance heat. [8]. The basic structure of a battery cell consists of four main components. [9]

- Electrodes (Anodes and cathodes)
- A current collector on the outside of each electrode
- A separator which prevents electron flow between the electrode
- A case

Through the current collector tabs, electrons move into and out of the current collectors. The external circuit, which houses the load to be powered, is connected to the battery by the tabs. The tabs can also be used to recharge batteries. Simulations and validation experiments are used to determine the temperature distribution and the heat generating rates of the cells.

Through the use of a twin-type heat conduction calorimeter, Onda et al.'s [8] studies measured the battery heat capacity and created a linear function of temperature. The heat production of battery cells has also been determined experimentally using calorimeters by Drake et al. [10] and Chen et al. [11] . However, modelling methodologies are becoming more significant as a tool to design better battery cells due to the rise in computer power and the need to investigate the thermal management of batteries in more detail.

The first equation relating to the heat transfer in a single Li-ion battery cell was published by Carolyn and Newman in 1995 [12]. The following is a presentation of Newman's [12] equation for heat production. Newman's [12] equation of heat generation can be presented as follows.

$$mC_p \frac{dT}{dt} = I^2 R + T\Delta S \frac{1}{nF} + Ah(T - T_{amb}) \tag{1}$$

where m is the cell mass (kg) and I denote the discharge current (A). The entropy change is denoted by ΔS and F is the Faraday constant (96485 s A/mol). R denotes the internal resistance of the battery cell (Ω). C_p is the heat capacity and T denotes the absolute temperature. In addition to that, t, n A, h and T_{amb} represent the time, number of moles, surface area, convection heat transfer coefficient and the ambient temperature.

This work can be seen as an extension of the work reported by Fuller et al. [13] even though Newman et al. [12] first reported on single cell heat transfer and thermal modelling. It is constructed on the premise that the cell temperature is uniform even though the temperature was allowed to vary over time. Additionally, the model created by Newman et al. [12] is an iso-thermal 1 D model, and iso-thermal modelling is significant since it aids in understanding how the battery functions at various temperatures. The iso-thermal model often assumes that heat created inside the cell is transmitted outside the system without taking heat transfer transferring techniques into account. Moreover, by establishing a heat transfer coefficient for each cell in the cell stack, Newman's 1 D model was utilised to examine the behaviour of a cell stack under heat transfer conditions. Heat is transported in a direction perpendicular to 1D cell layers, as indicated in [12].

As a result, when the cell stack temperature gradient can be omitted, the 1 D cell model put forth by Newman et al. [12] could be used to estimate the temperature and discharge behaviour of the battery. The results also showed that increasing the per cell heat transfer coefficient decreases the cell potential and temperature because more heat is transmitted from the cell stack to the surroundings as the heat transfer coefficient rises, resulting in a fall in cell temperature.

In addition to the Newman's 1 D model, three main methods are used for the heat transfer modelling and simulations of Li-ion battery cells. The lumped-parameter (LP) model, the Equivalent Circuit Model (ECM) and the self-learning neural network method can be identified as the modelling techniques for a single cell.

2.1.1 Lumped parameter (LP) model of single cell

Due to its simplicity in parameterisation and ease of implementation, the Lumped Parameter (LP) model is typically regarded as the most effective approach in real-time thermal

management applications. [14]. Using only a few factors, it illustrates how mass transport, charge transfer, and ohmic process effect the potential loss for a battery cell. [15].

There are several different LP battery model types suggested in the literature. Three alternative lumped models were constructed by Ekström et al. [16] for the purpose of predicting the voltage of lithium-ion battery cells under dynamic loads. Based on the difference between the open circuit voltage and the over potentials caused by the linear ohmic resistance, non-linear charge transfer resistance, and a diffusion impedance, those models produce time-dependent formulas for the cell voltage [16].

However, Benjamin Ng et al. [17] later reduced Ekström et al.'s [16] lumped model using Laplace transformation and transfer functions.

Additionally, Coman et al. [18] used a reduced-order lumped model to determine how much the temperature would rise when cylindrical Li-ion cells were discharged at high currents in a battery pack subscale. The model can only be used at lower discharge rates, as it was stated [18].

Wang et al.'s [19] simulations of heat transmission also made use of the lumped model for a single cell. The battery module's thermal behaviour is unaffected by the specific cell structure; hence it was assumed in the model that each cell is a homogenous cylinder with an internal heat source. Each cell in the battery module is viewed as a homogeneous unit with ideal thermo-physical characteristics, despite the fact that the cell is composed of various layers with distinct thermo-physical properties, such as density and heat conductivity. The data that the battery cell manufacturer also includes in the model is used to determine these properties. The lumped model considers both the momentum conservation equation and the energy conservation equation [19].

Continuity equation;

$$\nabla \vec{v} = 0 \tag{2}$$

Momentum conservation equation;

$$\frac{\partial v}{\partial t} + (\vec{v}\vec{\nabla})\vec{v} = -\frac{\nabla p}{\rho} + \frac{\mu\nabla^2\vec{v}}{\rho} \tag{3}$$

Energy conservation equation;

$$\rho C_P\left(\frac{\partial E}{\partial t} + v_x\frac{\partial E}{\partial x} + v_y\frac{\partial E}{\partial y} + v_z\frac{\partial E}{\partial z}\right) = k_T\left(\frac{\partial^2 E}{\partial x^2} + \frac{\partial^2 E}{\partial y^2} + \frac{\partial^2 E}{\partial z^2}\right) \tag{4}$$

These governing equations were numerically solved [19] using the commercial Ansys Icepak 14.5 software, which supports Computational Fluid Dynamics (CFD) for heat management.

By accounting for heat generation resulting from electrochemical activity and Joule heating, Ismail et al. developed a simplified [9] model for the Li-ion battery cell. Together with Newman's 1D model, the model was made [12]. To avoid the complexity of battery chemistry and composition, the model was also made under a number of other assumptions, including the following: (i) ambient conditions were constant; (ii) the discharge process was treated as being 100% efficient regardless of the discharge current used; and (iii) the cell temperature is constant [9].

Therefore, referring to Ismail et al. [9], a lumped capacitance model must be assumed in order to apply the equation correction and validated the assumption through the use of Biot number (B_i) which compares heat transfer occurring inside a body and its surface [9].

$$B_i = \frac{hL_c}{k} \tag{5}$$

The heat transfer model was built up using the MATLAB software [20]

The battery pack from the PROTON electric drive vehicle prototype served as the foundation for the simulation work. Because of its clear design and the simplicity, the lumped modelling approach is preferred for transient thermal management simulations. To increase the modelling accuracy for time-varying model parameters, such as the time-varying convective heat dissipation coefficient under diverse cooling conditions, an online parameterisation method is necessary.

2.1.2 Equivalent Circuit Modelling (ECM)

ECM is a favoured method for simulating EV battery cells as electrochemical models, which mimic the internal processes of these cells, demand significant computational resources. Electrical components (such as capacitors, resistors, or phased elements, for example) are included in ECM circuits that describe the many physicochemical processes that control heat generation and transmission within the battery cell.

A typical equivalent circuit for lithium cells is a one- or two-RC-block model without a parasitic branch. The key benefits of the ECM method are its ease of use and versatility in combination with other techniques, such as Coulomb counting with an Open Circuit Voltage (OCV) and State of Charge (SOC) correlation for periodic recalibration during testing.

A multi-temperature lithium cell simulation model including thermal dependence on the battery surface was published by Tauran et al. [21] .

The general ECM has been simplified by the model to an ECM with a single RC block, which can account for all dynamic features, including nonlinear open-circuit voltage, average discharge current, and cell inner temperature. The general ECM originally had n blocks. Tauran et al. [21] used MATLAB Simulink and Simscape for the modelling.

The cell temperature was calculated by solving the heat equation of a homogenous body exchanging heat with the environment as follows [9].

$$C_p \frac{dT}{dt} = \frac{-T - T_{amb}}{R_T} + P_s \qquad (6)$$

where, T is the inner cell temperature (K), T_{amb} is the ambient temperature (K) and R_T is the convection resistance (W/m²K). Power dissipated inside the cell is indicated in P_s (W). Applying a Laplace transformation, the inner cell temperature T can be denoted as follows [9].

$$T(s) = \frac{P_s R_T + T_a}{1 + R_T C_T S} \qquad (7)$$

Furthermore, as mentioned earlier, SOC also depends on the inner cell temperature. The *SOC* can be denoted as the function of exacted charge Q_e and the cell capacity C_Q of as follows [9].

$$SOC = 1 - \frac{Q_e}{C_Q} \qquad\qquad (8)$$

Each element of the equivalent circuit can be defined as a function of SOC and temperature.

2.1.3 CFD modelling of the battery cell

Kim et al. [22] employed two-dimensional thermal modelling to predict the thermal behaviours of a lithium-ion battery cell during the discharge and charge. Utilising the potential and current density distributions they obtained the temperature distribution over the Li-ion battery cell and followed the same research methods as Kwon et al. [23]'s study. Yi et al. [24] and Kim et al. [22] updated their thermal model to more effectively account for the discharge behaviour's dependence on the surrounding temperature.

Three-dimensional modelling was utilised in Yi et al.'s study [24] to explore the impact of operation conditions on the thermal behaviour of a lithium-ion battery module. The non-uniform distribution of the heat generation rate in a lithium-ion battery cell within the module made up of eight lithium-ion battery cells is calculated using the modelling strategy for a single cell developed by Kim et al. [21] [22]. In order to predict the electro-thermal behaviour of Li-ion battery cells with varied geometries using Abaqus, Kim et al. [21] constructed 2D Finite Element Analysis (FEA) models.

2.2 Heat transfer through composite material

2.2.1 Overview- manufacturing of composites

Composite material can be defined as a combination of two or more materials with different chemical and physical properties, and which remain separate and distinct on a macroscopic level within the finished structure. Reinforcement arrangements are the name given to composite materials that are contained in a matrix. The matrix guarantees the load's cohesion and direction [23]. Furthermore, the composite may transmit the stresses it experiences to the load. As a result, the majority of composite materials are heterogeneous and anisotropic. The three primary categories of composites are fibrous composites, laminated composites, and particle composites. Composites made of fibre in a matrix (or resin) are referred to as fibrous composites. The resin maintains the fibre together in the composite while the fibre aids in load transfer [24]. Different layers of materials can be seen in laminated composites. The

term "particulate composite" refers to materials that contain particles embedded in a matrix [25]. Composites materials have several benefits over the unreinforced matrix material, including superior stiffness and strength, good corrosion resistance etc. Therefore, the composites materials are used in a variety of industries, including packing, automotive, light structures, aircraft, thermomechanical components, etc.

Composite manufacturing involves processing two basic ingredient elements in order to create the finished product. The matrix and fibre materials are among the constituents, as was previously indicated [24] [26] . A strong link between the matrix and the fibre must be created during processing, and the finished item must have greater dimensional control. The processing should also possess the following qualities in order to produce the best results [27]

- Suitable amount of volume fraction of fibres
- Proper orientation of the fibres
- Uniform distribution of fibres between the matrix material
- Proper solidification process for the resin
- Limited number of voids and defects

In composite materials, the fibres contribute to the load transfer process and provide stiffness and strength [19]. Both stiffness and strength are affected by other fibre architecture parameters such as fibre length, fibre orientation and bundle size etc. The amount of fibres is usually expressed in terms of fibre volume fraction v_f , which can be defined as follows [22].

$$v_f = \frac{V_f}{V_c} \qquad (9)$$

where, V_f is volume of fibre and V_c denotes the volume of composite material [13].

$$1 = V_f + V_m + v_v \qquad (10)$$

The Equation (10) indicates the relationship between the fibre volume fraction and the matrix volume fraction (V_m) (in the composite). Generally, for a composite to be acceptable, the volume fraction of voids (v_v) should be less than 1%, and therefore, the simplified equation for the relationship between fibre volume fraction and the matrix can be defined as follows [13]:

$$1 = V_f + V_m \qquad (11)$$

The stiffness and strength of the composite material are also significantly influenced by the fibre orientation. However, it is noted that [22] the layer's incorrect positioning during the lay-up setup or the liquid resin's flow, which pushes the fibres during the filling in Liquid Composite Moulding (LCM) can cause the fibre orientation to vary from the planned orientation. Additionally, the resin is liquid during manufacturing process and it should have higher Yong's modulus and strength after curing to ensure the effective stress transfer through the reinforcement. During the production of composites, voids and flaws may emerge as a result of inadequate compaction of several layers or low resin pressure during curing [22].

In general, it can be said that the filament winding method, hand lay-up method, pultrusion method, LCM method, fibre placement method, and prepreg method are the most widely used mechanisms for producing composites in the market.

Manufacturing cylindrical goods with high tensile strengths, such as pressure vessels, pipes, and fuel storage tanks, mostly uses the filament winding method. This process has been found to produce laminates with a high strength-to-weight ratio and to help provide a high level of control over consistency and fibre orientation [23] .

Furthermore, the earliest and most basic open moulding technique for creating composites is the hand lay-up technique. In the initial step of the procedure, dry fibres in the form of knitted, sewn, woven, or bonded fabrics are manually inserted into the mould. The resin matrix is applied with a brush on the reinforcing materials. Hand rollers are utilised in the procedure to produce a uniform resin dispersion as well as to ensure an improved contact between the reinforcement and the matrix. The laminates are then allowed to cure under typical ambient conditions as the last step [24]. Although the procedure is straightforward and quick to carry out, the laminate is typically produced by including a lot of voids in the process. In addition, experienced staff is necessary to ensure good production quality. For air intake duct, wing stubs, and tail sections, the hand layup approach is typically employed extensively in naval and aerospace applications [25].

The only genuinely continuous processing method for moulding composites can be defined as the pultrusion method. The procedure is linked to low labour intensity, good raw material utilisation, and reliable final product quality [25]. In a variety of composite formulations (i.e., resin and fibre combinations), this approach is utilised to produce a wide range of cross-section forms [25] .

LCM is primarily employed in the production of fiber-reinforced polymeric composites. It encompasses wet compression moulding, Structural Reaction Injection Moulding (SRIM), Resin Transfer Moulding (RTM), and Resin Infusion moulding (RI) [26]. In comparison to other composite manufacturing techniques, the procedure has a low-to-average cost and is frequently used to create complicated, high-quality products. Furthermore, reproducibility can be attained via LCM. The reproducibility of the approach, however, may be constrained by the uncertainties in the LCM process inputs, such as shape, circumstances, and materials [26].

The fibre placement technique is a fully automated method used to create intricate, superior, advanced air vehicle structures that are lightweight [27]. A robotic device with an attached fibre placement head is used in the procedure, which makes it possible to lay several strips of composite material or tows on a tool surface. The adhesion between arriving tows and substrate is guaranteed by the proper process conditions, which include heating, tensioning, and compaction. In the procedure, tows are connected to make a course, which is then joined to produce a ply. A laminate is made up of several plies [27].

In the prepreg process, the prepregs are impregnated with resin prior to manufacturing. Carbon, glass, or aramid are often infused, layered, or coated with resin during the prepreg manufacturing; the choice of resin and fibre depends on the intended purpose of the material [27]. The prepreg composite is cured using a mix of heat and pressure after being cut and moulded, often in an autoclave with a vacuum pump. Prepreg is used in the aerospace, energy, and automotive industries because it eliminates the need to store and apply resin separately because the resins are added mechanically [27]. It is impossible to alter the fiber/matrix ratio when utilising prepregs.

2.2.2 Thermal conductivity mismatch of composites

Thermal conductivity refers to the intrinsic property of a material that determines its ability to conduct heat. It quantifies how efficiently heat transfers through a substance when there is a temperature gradient present. Higher thermal conductivity implies better heat transfer capability. This phenomenon can be understood through the atomic or molecular level interactions within a material. In materials with high thermal conductivity, such as metals, heat is transferred through the lattice vibrations of atoms. On the other hand, in insulating materials like plastics or ceramics, heat transfer is less efficient due to weaker atomic interactions and the presence of air pockets. In essence, thermal conductivity dictates the rate at which heat

energy moves through a material, impacting various aspects of heat management and thermal performance in engineering and scientific applications.

Fourier's law in thermal conductivity states that "for a homogenous solid, the local heat flux is proportional to the negative local temperature gradient" [28]. Fourier established the theory of thermal conductivity in 1822. The formula for thermal conductivity for a one-dimensional steady state heat transport is as follows [28]:

$$q^n = -k \frac{dT}{dx} \qquad (12)$$

where q is the heat flux (W) and k denotes the thermal conductivity of the material (W/mK). $\frac{dT}{dx}$ represents the change of temperature across the thickness (K/m) and negative sign indicates the temperature reduction from hotter surface to the cold surface.

From equation (12), it is possible to derivate the thermal conductivity is as follows [28].

$$k = (Q/A)/(\Delta T/\Delta L) \qquad (13)$$

where, Q is the heat flux (W) and A is the cross-sectional area of the specimen (m^2). ΔT denotes the temperature difference (K) and ΔL is the overall distance (m). Therefore, when the temperature gradient is normal to the given cross-sectional area, the thermal conductivity of a material can be defined as a rate at which heat is transferred by conduction through a given unit area of a given material.

While CFRP and GFRP exhibit higher thermal conductivity compared to many thermally insulated materials, the overall thermal conductivity of composite materials remains relatively low in comparison to other substances. This property is influenced by various factors including the type of fiber and resin used, the volume fraction of components, their orientation, operating temperature, and the direction of heat flow [28] . A composite material's thermal conductivity is also anisotropic.

Additionally, in the presence of heat flow, dispersions with thermal conductivity values that are different from those of the matrix phase would form near localised temperature distributions and associated thermal stresses and displacements [29]. As described in [30] this effect is known as the thermal conductivity mismatch effect in composites and is characterised by the

fact that such stresses and displacements are inversely proportional to the strength of the temperature gradient.

According to the literature [30], numerical methods can be used to calculate the magnitude of the thermal stresses, including those brought on by the thermal conductivity mismatch effect, for any given composite material with a predetermined geometry subjected to any particular thermal environment. Using the computational method, Hasselman et al. [30] examined how thermal conductivity mismatch affected the thermal stresses in composite material under the steady state heat transfer. As mentioned in the literature [31] the thermal conductivity of composites was studied using a variety of models, including the "Molecular dynamics" and "Finite element" approaches.

2.2.3 Insertion of through thickness reinforcements in composites

In general, the manufacturing process and the reinforcing architecture influence the production of composite structures with excellent mechanical performance. The choice of reinforcement also influences the optimisation and management of thick constructions with complicated geometries.

Noobing, knitting, braiding, and weaving can be recognised as the primary reinforcing processes based on the thickness of the reinforcements. However, because the primary goal of this research is to improve thermal conductivity in the Z direction, the through-the-thickness reinforcing technique is covered in more detail later on in this Chapter.

 Z-pinning, stitching, and tufting can be identified as the three most widely used technologies of through the thickness reinforcement.

- Z-pinning

Z-pinning technology is the process of locking laminate piles together by inserting rigid rods or pins that function as tiny nails [32]. According to the literature [33], Z-pinning technology specifies positioning over the layer of foam containing the pins. The pins are typically inserted into the laminate using an ultrasonic impactor. The compressed foam is taken out at the end of the treatment, and any superfluous Z-pins are sheared away.

Z-pins are often made of high stiffness and high strength materials, such as carbon/epoxy, steel, or titanium, and their diameter ranges from 0.2 to 1.0 mm [32]. Due to the stiffness of the rods, this approach enables the reinforcing of pre-impregnated laminates.

Both the volume fraction and the diameter of pins in Z-pinning composite reinforcement play significant roles in determining the resistance to delamination. Published data suggests that the areal density typically ranges from 0.5% to 4.0%, equivalent to 8 to 70 Z-pins/cm^3, aiming to improve mechanical performance.[34]. This method is also the simplest and most dependable method for composites' three-dimensional reinforcing. Furthermore, it provides versatility in the location of through-thickness reinforcement by allowing for adjustments to stitching factors including pattern, thread type, and stitch density. [36].

- Stitching technology

The stitching technology has been cited as one of the most effective methods for through-thickness reinforcement by Mouritz et al. [32] , Dransfield et al. [35], and Tong et al. [36] . The sewing process, which employs a dual-threading system that combines bobbin and needle threads, is the main inspiration for this method.

Typically, stitching involves threading high-performance yarns through the thickness of the laminate, utilizing materials like Kevlar, glass, carbon, or other fibres known for their high strength. The mechanical characteristics of the resulting structure are primarily determined by the properties of these fibres and the density of stitches employed [33].

Stitching technology enables the creation of intricate 3D designs, unlike Z-pinning, which is primarily limited to two-dimensional planes.

- Tufting technology

Tufting technology, which was formerly employed in the manufacture of carpet and warm clothing, is currently acknowledged as one of the most cutting-edge techniques for thickness reinforcement [36]. Tufting technology is also known as single-sided stitching technology and is especially made for the dry preform or liquid composite moulding processes [36].

The loops are not tied, and the tufts are inserted with a hollow needle. The inherent friction between the fabric and the thread keeps the tufting yarns in place.

The technology only requires single sided access to the preform because this stitching method only stitches one side of the preform.[34].

However, tooling modifications are required in order for the needle to completely pierce the stack and create the required loops during the tufting. Without the loops, the method is much less effective.

Z-pinning technique

https://en.wikipedia.org/wiki/Z-pinning

a) Lock stitch

b) Chain stitch

Stitching technique

https://www.researchgate.net/figure/7-Types-of-stitching-used-for-through-thickness-reinforcement_fig3_24297988

Tufting technique

https://www.researchgate.net/figure/Tufting-process-description_fig1_262222241
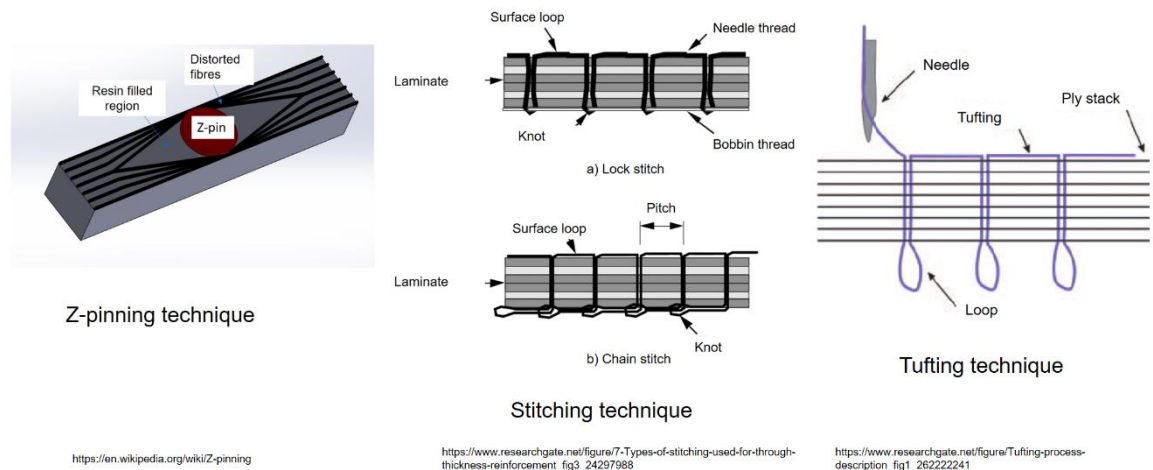
Figure 2.1. Different types of through thickness fabrication methods

The use of conventional unidirectional and fibre-based composites in thermal management applications is constrained by their low heat conductivity in the through-thickness direction, as was already mentioned. Therefore, maintaining the structural integrity of laminates is necessary to maintain the through-thickness heat conductivity of composite materials. [37].

The combination of high thermal conductive parent materials [38], some high thermal conductive fillers [39], and three-dimensional weaving technique are the three main methods utilised to boost the through thickness thermal conductivity of composites [40].

When cost and structural stability are considered, it is discovered that the industry is more interested in adding some high thermal conductivity fillers. Many materials with high thermal conductivity have been used as fillers in composites to boost their thermal conductivity, including carbon nanotubes (CNTs), aluminium oxide, diamond, boron nitride, and graphene. Among all of these filler materials, graphene stands out as being particularly promising due to its outstanding thermal conductivity, unusual two-dimensional structure, strong electron mobility, and zero-gap ban structure. The above-mentioned materials have relative thermal conductivities of 72, 2200,751, and 3000-5000 W/mK.

The thermal conductivity of suspended single-layer graphene is proven to be around 5000 W/mK by Li et al. [41]. Graphene has been discussed and used as a filler material for polymer composites in a number of researches [42], [43] [44].

Although three-dimensional weaving can dramatically boost through-thickness thermal conductivity, it is noted that the process' complexity is significantly higher than that of the other two processes . [45] [46], [47].

2.3   Methods to improve thermal management of battery casing

Temperature control and thermal management can be achieved by active or passive means built into the battery packs, which provide cooling. Convective cooling is achieved by blowing air across the cell modules. Both natural convection (i.e., passive) and forced convection (i.e., active) are utilised in air cooling techniques. Since the convective heat transfer coefficient of natural air cooling ($0.5W/m^2K$) is lower than that of forced air cooling ($10 W/m^2K$), natural convection cooling is only effective for low energy batteries. Park [48] [49] investigated the influence of geometrical layouts with various forced airflow intake and exit duct types through creating thermal resistance models.

Mohammadian and Zhang [50] presented a unique design of air-cooled thermal management approach for prismatic Li-ion cells by incorporating pin fins into the airflow channels. In the study of Yu et al. [51], they created a temperature-controlling technique that uses separate air channels and fans to provide bidirectional airflow. Fan et al. [52] [53] examined the effects of gap spacing and fan size on the forced air-cooling.

Heat transfer with liquids instead of air can be achieved in a number of ways:

- •   Through discrete tubing around each module, with a jacket around the module
- •   Through submerging modules in a dielectric fluid for direct contact
- •   By placing the modules on a liquid cooled plate

The most frequently employed heat transfer mediums are water, glycol, or refrigerants if the liquid is not in direct contact with the modules. The heat transfer liquid, on the other hand, must be dielectric if the modules are immersed in it, like silicon oils or mineral oils. A water-ethylene glycol solution was utilised by Chen and Li [54] to regulate the temperature over the

battery packs and Lan et al. [55] created discrete flat aluminium tubes that are entangled around prismatic cells.

In the study by Zhang et al. [56], prismatic cells were arranged in a staggered fashion with an encircled aluminium tube. To improve thermal conductivity, a flexible graphite sheet was inserted between the tubes and the cell wall. A prismatic bipolar Li-ion battery pack with sandwich structure Li-ion cells was modelled by Tong et al. [57]. A cold plate made of aluminium that has straight minichannels was also examined by Huo et al [58] [59].

Although liquid cooling is preferable than air cooling in terms of battery thermal management, using such cooling systems has a few drawbacks. Liquid cooling systems add additional parts to the battery, complicate the geometry and arrangement of the battery cells, increase the battery's overall weight, and run the risk of leaks that could cause the battery to fail. Convective heat transfer is used by active air and liquid cooling techniques to move heat produced during operation. The added weight and complexity could, however, result in higher parasitic power costs, which would reduce cooling efficiency.

The focus of current research is on passive cooling techniques that might be as effective as active cooling techniques. Utilising the latent heat created when Phase Changing Materials (PCMs) undergo phase shift is one approach currently being tested. Experimental research on the thermal management of battery modules with PCMs was conducted by Duan and Naterer [60]. Kizilel et al.'s [42] investigation into PCMs' benefit over traditional active cooling.

While dramatically lowering the heat gradient inside the battery pack, PCMs have several disadvantages. For instance, the PCM increases the size and weight of the complete battery pack. Additionally, the PCM matrix may fully melt after numerous charges or discharge cycles. When the phase change material (PCM) fully melts, various solutions are implemented to address this issue. One common approach involves integrating secondary materials or additives within the PCM to modify its melting point or enhance its thermal properties. Additionally, encapsulation techniques are utilised to confine the PCM within a structure, preventing leakage or spreading upon complete melting. However, despite these measures, challenges persist. The temperature difference among cells arises due to the latent heat absorption or release during the PCM's phase change process. This phenomenon leads to variations in temperature distribution across the battery pack, where some cells experience higher temperatures while others remain cooler. Factors contributing to this discrepancy include differences in PCM distribution, varying heat dissipation rates, and thermal conductivity variations within the battery pack materials. Consequently, optimising the design

and placement of PCMs, improving thermal insulation, and implementing advanced control strategies are essential for effectively regulating heat distribution and mitigating the temperature disparity among cells within the battery pack.

2.4 Discussion and conclusion

Given the aforementioned considerations, it is better to represent the heat transmission of a Li-ion battery cell using a three-dimensional CFD model. The reason for this is that, as compared to other models, the 3D CFD method is that it offers a good compromise between computational efficiency and accuracy. Additionally, because to the little usage of experimental and parametric data, it is relatively simple to utilise. Additionally, because the phenomena that need to be modelled are non-linear and the spatial distribution of the battery cell is a key factor in the thermal performance of the battery, the 3 D model will be more accurate in simulating real-world situations. Additionally, a 2D model will be unable to accurately capture the spatial differences in heat transmission through the composite casing because the research will examine composite casing with varied thermal conductivity. The quantity of heat produced inside the battery cell and battery module will also be determined using the modified Newman's equation. This necessitates simulating each cell's quasi-steady-state heat output.

It is advised to employ the LCM method as the fabrication approach for the composite casing because it is straightforward and inexpensive. Although the hand lay-up approach is much simpler than the LCM method, it is not advised because of the subpar surface. Due to its low cost and superior surface polish, the vacuum-assisted resin infusion method under the LCM method will be employed to fabricate composite enclosures.

Graphene, boron nitride, and other materials with high thermal conductivity have all been employed as fillers to increase the thermal conductivity of composite materials. But in addition to all of those elements, composites made of copper and copper alloys are frequently utilised in the industry and are advised for this study. This is so that copper, a material with high electron mobility and particularly high thermal conductivity, can be detected. Despite being a better option, graphene is not advised due to its high cost, requirement for expert labour, and inability to be placed at exact spots using the LCM approach. Therefore, it is advised to use the Z-pinning technique to insert the copper pins through the thickness.

A completely new idea for a composite casing is considered in this project. The composite casing will have a variable thermal conductivity, depending on the volume fraction and other conductive elements (including Copper pins). The selective high conductivity in areas of the casing will create "Thermal avenues" close to the hot areas of the battery in order to provide passive heat dissipation in the areas needed the most.

The study will include the effect of adding features to the inner and outer surface of the composite casing, such as tapered surface with fins, in order to increase the surface area for the purpose of higher-level heat transfer.

3   Development of heat transfer model for Li-ion battery module

3.1   Analytical model for Li-ion battery cell heat transfer

During charge and discharge, batteries primarily produce heat as a result of enthalpy changes, resistive heating within the cell, and electrochemical polarisation. The energy balance equation is based on the energy conservation law and the heat generation can be expressed using cylindrical coordinates as follows.

$$\rho C_p \frac{\partial T}{\partial t} = \frac{1}{r}\frac{\partial}{\partial r}\left(k_r r \frac{\partial T}{\partial r}\right) + \frac{1}{r^2}\frac{\partial}{\partial \varphi}\left(k_a \frac{\partial T}{\partial r}\right) + \frac{\partial}{\partial z}\left(k_z \frac{\partial T}{\partial z}\right) + \dot{Q} \qquad (14)$$

where, ρ is the density of active battery material (kg/m³) and C_p is for specific heat capacity (J/kgK). T denotes the absolute temperature (K) and r represents the radius of the battery cell (m). k_r , k_a and k_z denote the thermal conductivity for radial, axial and z directions respectively (W/mK). Furthermore, $\dot{Q}$ denotes the volumetric heat generation rate for the battery cell (W).

The variables on the right-hand side, meanwhile, are an expression for the volumetric heat generation rate and three-dimensional heat conduction, respectively. The term on the left-hand side denotes the energy stored inside the battery. The cathode, separator, current collector, and anode layers of the battery cell are coiled spirally into a cylindrical shape. Each battery cell is viewed as a homogenous body with useful thermo-physical qualities, despite the fact that individual components have distinct thermo-physical characteristics. Therefore, the effective value of density and heat capacity of each battery cell is calculated as follows.

$$\rho C_p = \frac{\sum_i \rho_i C_{p,i} v_i}{\sum_i v_i} \qquad (15)$$

where, v_i denotes the volume of each component. In addition to that, the thermal conductivity of the cell is anisotropic and therefore the thermal conductivity in radial and axial direction is defined as follows.

$$k_r = \frac{\sum_i L_i}{\sum_i {L_i}/{k_{T,i}}} \qquad (16)$$

$$k_a = \frac{\sum_i L_i k_{T,i}}{\sum_i L_i} \qquad (17)$$

where, L_i is the thickness of each component.

For the investigation of the heat transport in the battery cell, the lumped capacitance model is taken as given. Lumped capacitance thermal modelling typically takes a transient conduction approach and assumes that a solid's temperature is spatially homogeneous and solely a function of time, *t*. This suggests that a solid has virtually zero temperature gradients and an infinite thermal conductivity, *k*. Although this is not the case in reality, it can be approximated if there is a large difference between the thermal resistance to convection between the solid and its surroundings and the thermal resistance to conduction within the solid.

$$\frac{L_c}{k} \ll \frac{1}{h} \qquad (18)$$

where, *k* represents the overall heat conduction coefficient (W/mK), *h* is the convection heat transfer coefficient (W/m²K) and L_c is the characteristic length (m).

$$L_c = \frac{V}{A} \qquad (19)$$

V and A are the volume (m³) and the surface area (m²) of the solid respectively. For the cylindrical battery cell $L_c = \frac{r}{2}$. Also, the premise in Equation (20) formulates the dimensionless Biot (Bi) number.

$$Bi = \frac{h L_c}{k} \ll 1 \qquad (20)$$

Bi physically represents the ratio of the heat transfer resistances inside and at the surface of the battery cell. *Bi* has to be significantly less than 1 to be applied in this lumped capacitance model. It is because, when the *Bi* number is much less than 1, it implies that the thermal resistance within the object is much smaller compared to the thermal resistance at the surface of the object. In addition, it implies that the characteristic time for heat conduction within the

object is much smaller than the characteristic time for heat conduction at the surface [28]. According to literature [28], a *Bi* value less than 0.1 would yield an error of less than 5% in a transient heat transfer model. Therefore, it is assumed that the lumped capacitance method is acceptable for situations with *Bi* < 0.1.

When considering the parametric values related to this research which were taken from measurements, manufacturer data and calculations, {i.e. Characteristic length for the battery cell L_C= 0.009 m, convection heat transfer coefficient of air h=10 W/m²K and thermal conductivity of battery material k=29.56 W/mK} the Bi is less than 0.1. Therefore, it is possible to apply the lumped capacitance model for the Li-ion battery cell heat transfer analysis.

3.1.1 Model Assumptions

The temperature gradients in one or two directions can be disregarded by the lumped capacitance model without sacrificing simulation precision because the temperature is a spatially dependent function of time. Additionally, thermal models of lumped capacitance with confinement in three directions are frequently used. Therefore, by considering the above assumptions and assuming a uniform temperature distribution, Equation (14) can be simplified as follows.

$$\rho C_p \frac{\partial T}{\partial t} = \frac{1}{r}\frac{\partial}{\partial r}\left(k_r r \frac{\partial T}{\partial r}\right) + \frac{1}{r^2}\underset{0}{\cancel{\frac{\partial}{\partial \varphi}}}\left(k_a \frac{\partial T}{\partial r}\right) + \frac{\partial}{\partial z}\left(k_z \cancel{\frac{\partial T}{\partial z}}\right) + \dot{Q}$$

$$\frac{1}{r}\frac{\partial}{\partial r}\left(k_r r \frac{\partial T}{\partial r}\right) = -hA(T_{amb} - T) \qquad (21)$$

$$\rho C_p \frac{\partial T}{\partial t} = hA(T - T_{amb}) + \dot{Q} \qquad (22)$$

The equation confirms the Newman's equation of heat transferring in Li-ion battery cell. According to literatures, $\dot{Q}$ can be denoted as follows.

$$\dot{Q} = i^2 R_i - \frac{iT\Delta s}{nF} \tag{23}$$

3.2   Finite element model for Li-ion battery cell and module

The simulation model for the Li-ion battery cell was developed as a CFD model in COMSOL Multiphysics software.

A 3D model for transferring heat in the battery module and a 1D model for calculating the heat generation in individual cells are coupled in the simulation model. The essential battery cell chemistry is made possible by the 1D model, which also generates the temperature distribution at each cell's outer surface. The temperature profile of the battery cell and module is modelled using a 3D model. It was created using the heat transfer model proposed by Newman.

3.2.1   1 D model

The 1D cell model is created using the Lithium –Ion battery interface and consists of three domains [53]

- Negative porous electrode ($Li_x C_6 MCB$))
- Separator
- Positive porous electrode ($LiMn_2 O_4$))

According to COMSOL libraries, the model was developed to cover the following processes of electronic current conduction in the electrodes, ionic charge transportation between the electrodes and the separator and the material transportation in the electrolyte.

For the electronic current balance in the model, *V*=0 is put on the current collector of the negative electrode. The current density is specified at the collector for the positive electrode. Current density cycles via three stages: a discharge, a period of no current, and a concluding charging stage. The inside perimeters that the separator can see are insulated. To keep the electrolyte's ionic charge equilibrium, the current collector is additionally insulated. The material balance is also subject to the insulating conditions [53].
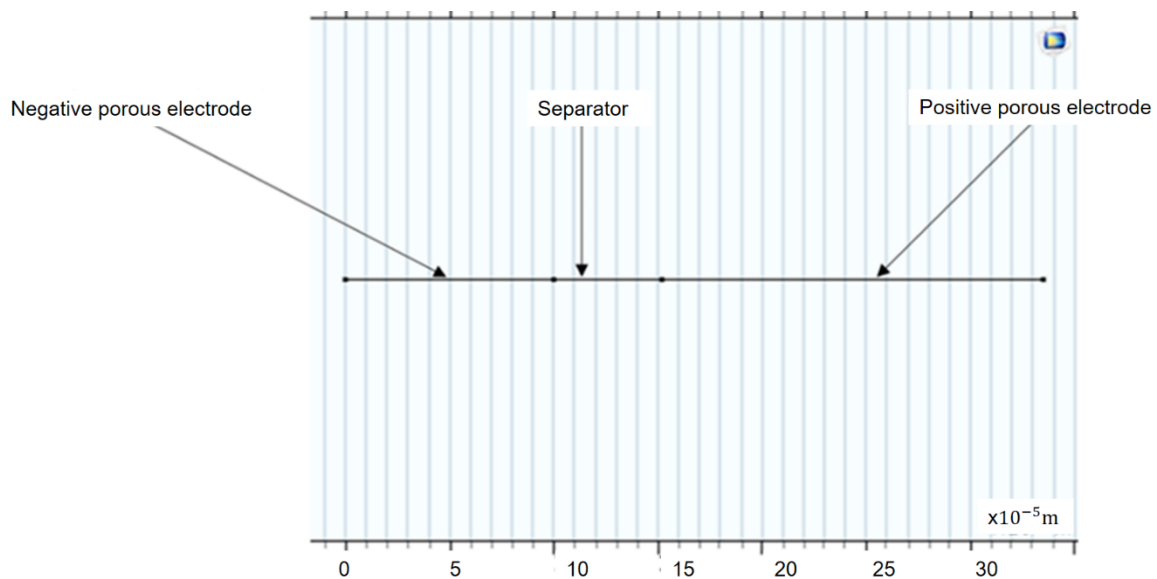
Figure 3.1. 1D model for Li-ion battery cell [53]

As indicated in the Li-ion battery interface, the electrolyte consists of 2M $LiPF_6$ salt in 1:2 EC: DMC (by volume) solvent and P (VDF-HEP). The electrode materials are carbon based for the negative electrode and $Li_yMn_2O_4$ for the positive electrode.

3.2.2 3 D model

The 3D model is developed using the Heat Transfer in Solids and Fluids Interface. The geometry consists of four domains:

- Active battery material domain
- Cylindrical battery connector
- Mandrel
- Flow compartment

The active battery material domain is made up of wound sheets of cell material. The heat source is coupled to the active battery material. Due to the spiral winding of the battery cell layers, the active battery material's thermal conductivity is anisotropic. The simulation considers the thermal conductivity, density, and heat capacity of the active battery material as effective values as they are stated in the literature [53]. In battery cells, particularly those with spiral winding configurations commonly found in cylindrical lithium-ion battery cells, the thermal conductivity, density, and heat capacity of the active battery material (such as electrodes and electrolytes) can exhibit anisotropic behavior. This anisotropy arises from the

structural arrangement of the battery cell layers, where heat transfer may occur more readily along certain directions (e.g., parallel to the winding direction) than others [53].

To accurately model heat transfer in such battery cells, researchers often resort to simplifications or effective values for these thermal properties. These effective values are typically derived from experimental measurements or theoretical analyses and represent averaged or homogenised properties that capture the overall behavior of the material within the battery cell.

For example, the literature [53] state that the thermal conductivity of the active battery material is considered an effective value because it varies depending on the direction of heat flow within the cell. Similarly, density and heat capacity may also be treated as effective values to simplify simulations while still capturing the essential heat transfer characteristics of the battery.

In order to account for the orthotropic heat conductivity of the active battery material, the model has been expanded using a cylindrical coordinate system. The steel cylindrical battery connector, which is positioned on top of the battery, is cylindrical in shape. The mandrel is the nylon isolator that the battery cell sheets are wrapped around. Air fills the space around the battery cells. Interfacial properties were modelled by applying a heat transfer coefficient at each interface.

To identify the heat source, two factors are multiplied by the volumetric heat source from the 1D Li-ion battery model. The area of the overall 1D model where heat is created is the first factor. The fraction of the overall 1D model can be determined by dividing the total of the lengths of the negative electrode, separator, and positive electrode by the length of the entire battery cell. The second factor is the part of the total 3D cylindrical cell design that produces heat. The volume that produces heat is calculated by deducting the total volume of the cell from the sum of the volumes of the mandrel and outer can. This then divided the heat source's entire volume.

$$Q_{h,3D} = Q_{h,1D} \frac{L_{neg} + L_{sep} + L_{pos}\left(\left((r_{batt} - d_{can}))^2 - r_{mandrel}^2\right)\right)}{(r_{batt}^2 - r_{mandrel}^2)h_{batt}} \qquad (24)$$

The 3D model's inlet and start temperatures are both set to 25°C as boundary conditions. A pressure of 1 atm is set at the outlet, and an inlet velocity of 0.1m/s is applied to the flow. The symmetry planes are subjected to symmetry boundary conditions. The battery walls are not subjected to slide situations. The alternating charge and discharge current at 7.5 C rate with a cycle duration of 600s and a relaxing period after 1500s is represented by a square wave function based on literature [53]. The State of Charge (SoC) of the cell is initially set to 10%.
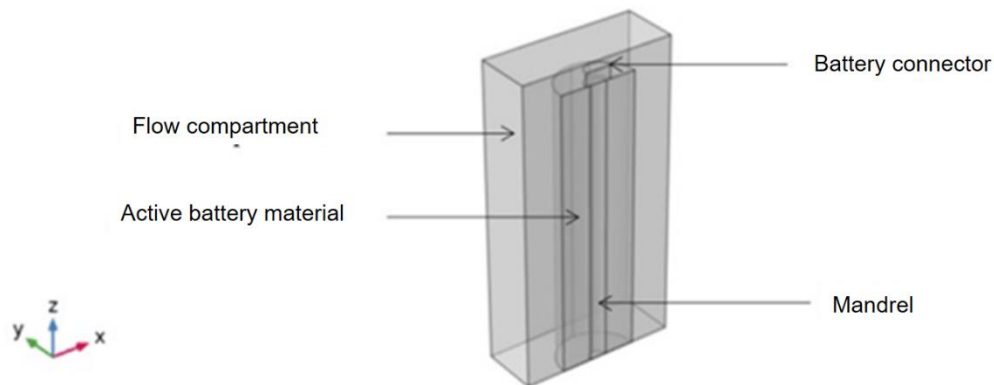

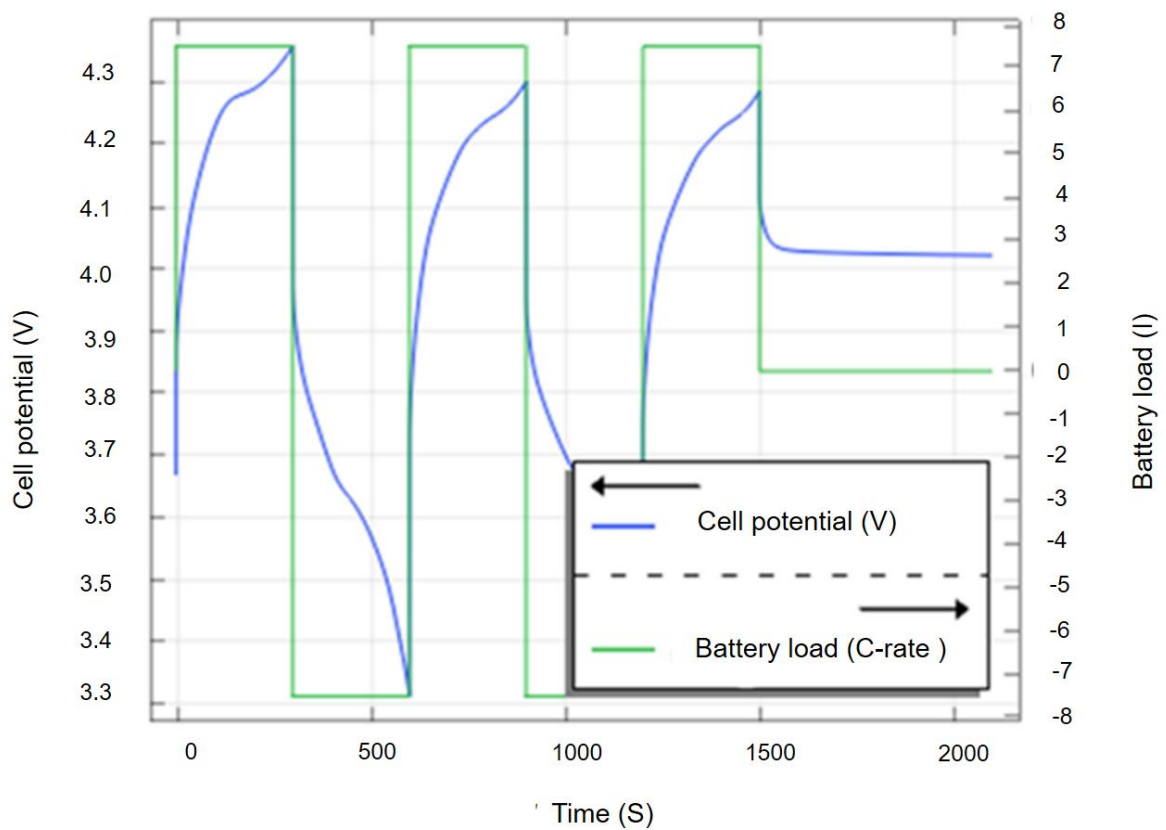**Figure 3.2**. 3D model for Li-ion battery single cell

Figure 3.3.Cell potential and load [53]

The mesh comprises 45,000 tetrahedral elements, with each element sized at 1 mm. Initially, the mesh size was adjusted from its default setting to 0.5 mm, transitioning from a coarse mesh to an exceptionally fine one in an effort to optimize simulation accuracy. However, it was observed that as the element size decreased to 0.5 mm, simulation convergence was hindered. Upon comparison between the coarse mesh and the final mesh (element size: 1 mm), a 5% enhancement in results was noted.

The simulation consists of three steps. The steady state flow at 25 °C is solved in the first stage. The potentials for each cell are solved at t=0 in the second phase. The steady state answers from the first two steps are utilised to set the initial values for the potentials in the third step, which is a time-dependent analysis of the entire problem.

The results reveal that the maximum temperature within the battery cell surpasses 62.5°C, with surrounding air temperatures fluctuating between 26°C and 42°C. Notably, peak temperatures are concentrated in core areas, including the mandrel and active battery material. These findings closely align with actual temperature distributions reported in previous literature [53], which cite a maximum cell temperature of 65°C. This indicates a minor deviation of 3.8% between the actual and simulated results, suggesting good agreement overall.
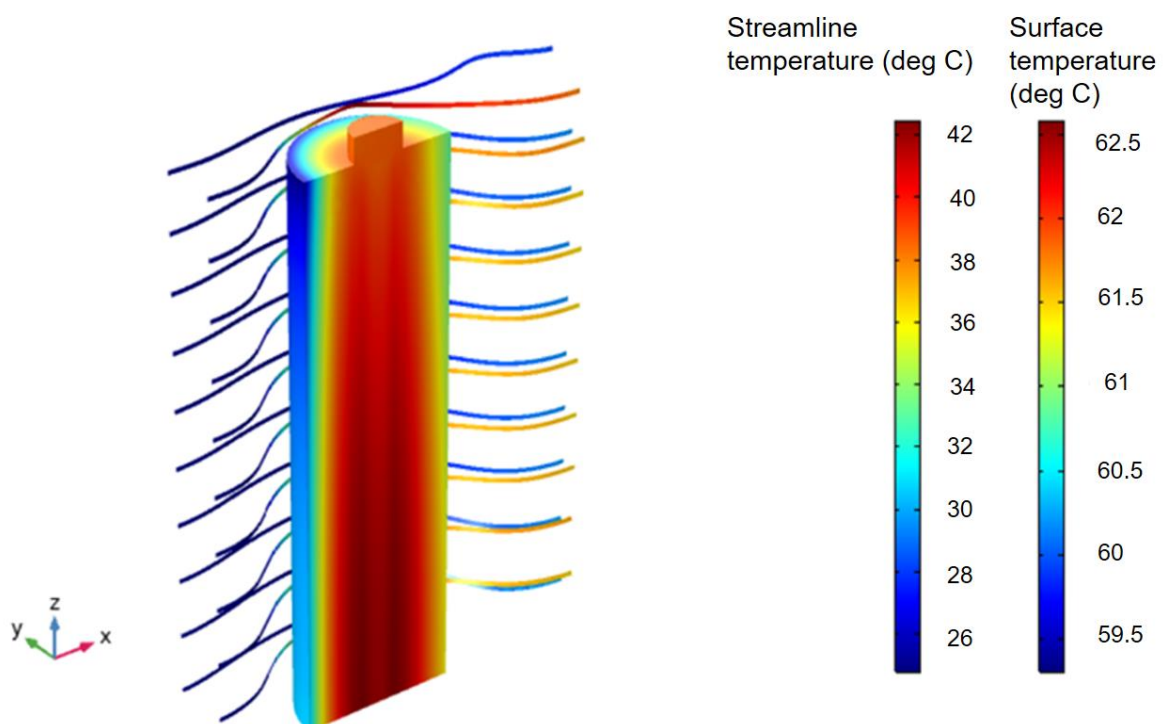
Figure 3.4. Temperature distribution of a single cell

3.3 Effect of the battery canister in the heat transfer of a Li-ion battery cell

To investigate the effect of the battery canister, the 2D axisymmetric model of a Li-ion battery cell was used. In a battery cell, the battery canister serves as a cover for the active battery material of the cell. According to the general battery manufacturer's data, the battery canister is a steel cylindrical can with a thickness of 0.25 mm [69].

The COMSOL Lumped Battery Interface is used to construct the 2D axisymmetric cell model. Battery capacity and the initial state of charge are inputs needed by the interface. The interface is also related to ohmic, activation, and concentration as specified in a real battery cell by the manufacturer. Coupled with the COMSOL Heat Transfer in Solids Interface, the lumped model is resolved. [69].

In addition, the Electrochemical Heating Multiphysics Node is used to couple the temperature and the generated heat source between the lumped battery and heat transfer in solids interfaces.

The thermal model of 2D with axial symmetry is employed to ignore heat conduction in the spiral direction of a spirally wound battery. To avoid simulating the heat conduction in each layer of the wound sheets in the radial direction, the wound sheets are once again treated as one active battery material domain. The simulation accuracy was unaffected by the assumptions made for the simulation's simplicity because accurate thermophysical properties were tested during the simulation.

The overall geometry has a radius of 9mm and 65mm height. The geometry contains three domains.

- Battery canister (Steel, 0.25mm thick)
- Active battery material domain (Wound sheets of cell material)
- Mandrel (2 mm radius)

The effective thermal conductivity, density and the heat capacity are considered in the simulation.

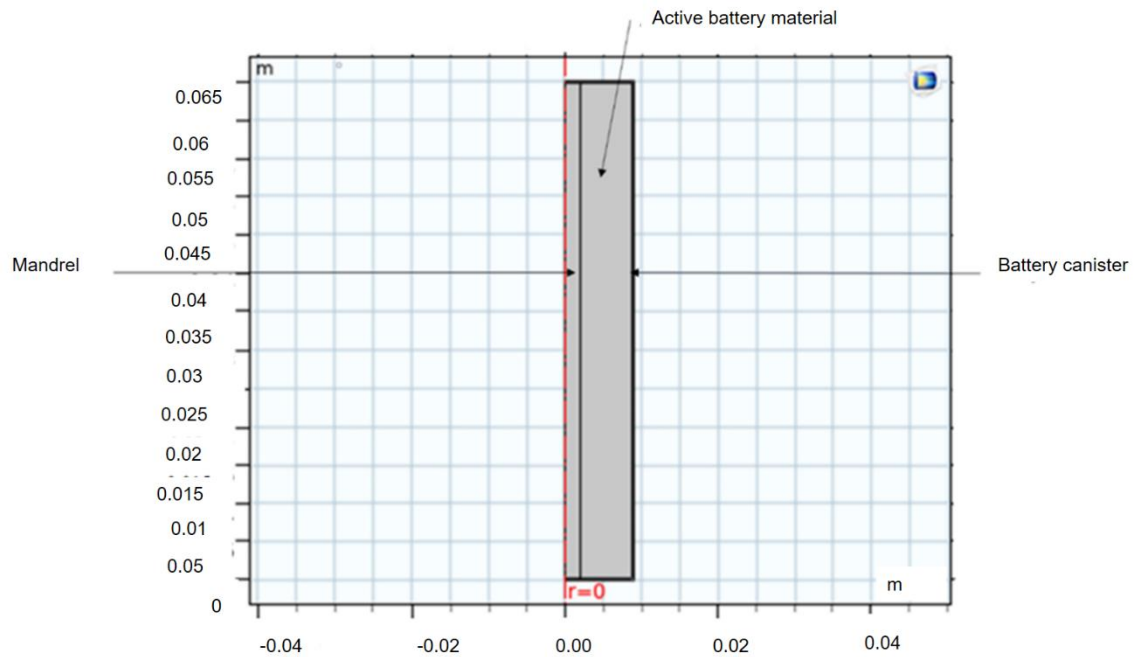**Figure 3.5**. 2D battery cell model

On the battery canister surface, a heat flux boundary condition is specified using a heat transfer coefficient of $h = 10$ W/m²K and an external temperature of 25 °C. This would typically correspond to air cooling by low velocity of 0.1 m/s forced convection. The initial temperature of the battery is set to 25 °C.
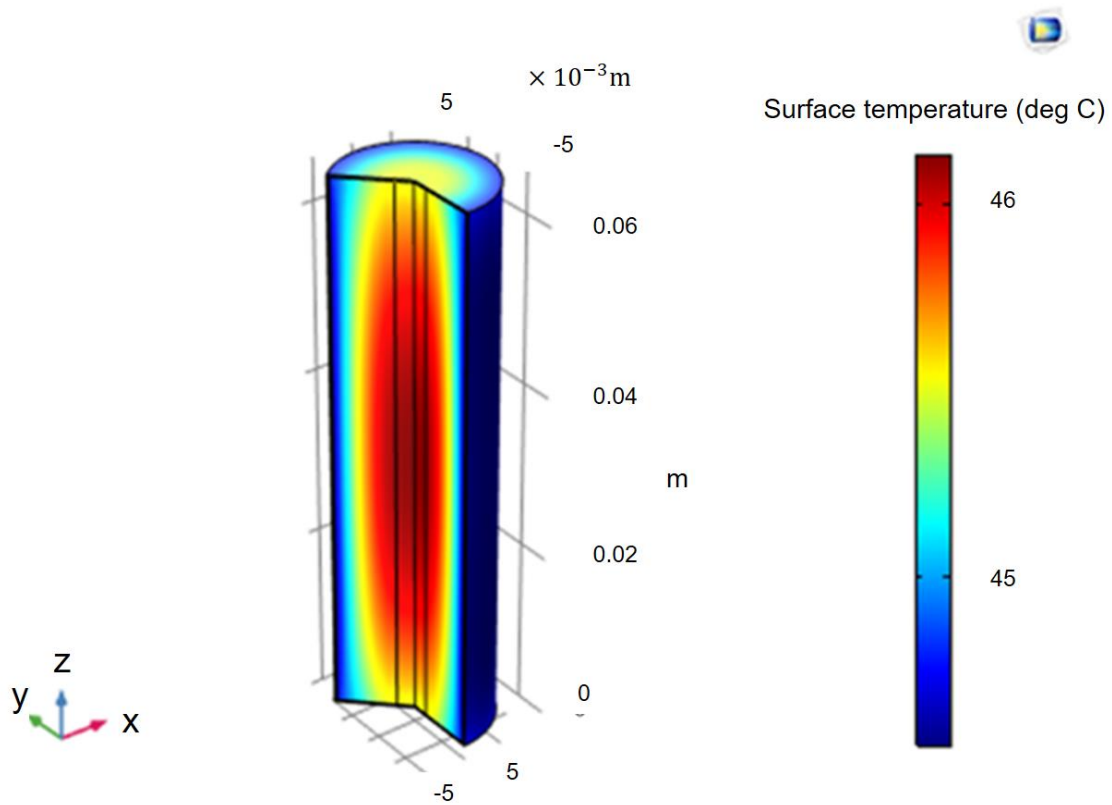

Figure 3.6. Temperature distribution after 1500 s

The analysis indicates that the primary locus of temperature elevation within the battery cell resides in its active material core, with negligible impact observed from the surrounding battery canister. This finding underscores the dominant influence of internal heat generation and dissipation mechanisms on the overall thermal profile. The recorded maximum temperature of 46°C at the core underscores the significance of internal thermal management strategies for enhancing both performance and safety. By emphasising the internal dynamics of heat generation and dissipation, this analysis highlights the imperative for optimising internal thermal management strategies to mitigate temperature-related risks and enhance the overall efficiency and safety of battery systems.

3.4   Heat transfer analysis of Li-ion battery cell module

In order to investigate the temperature distribution and the heat transfer of a battery module, initially a matrix which contains 9 (3×3) cylindrical battery cells is used.
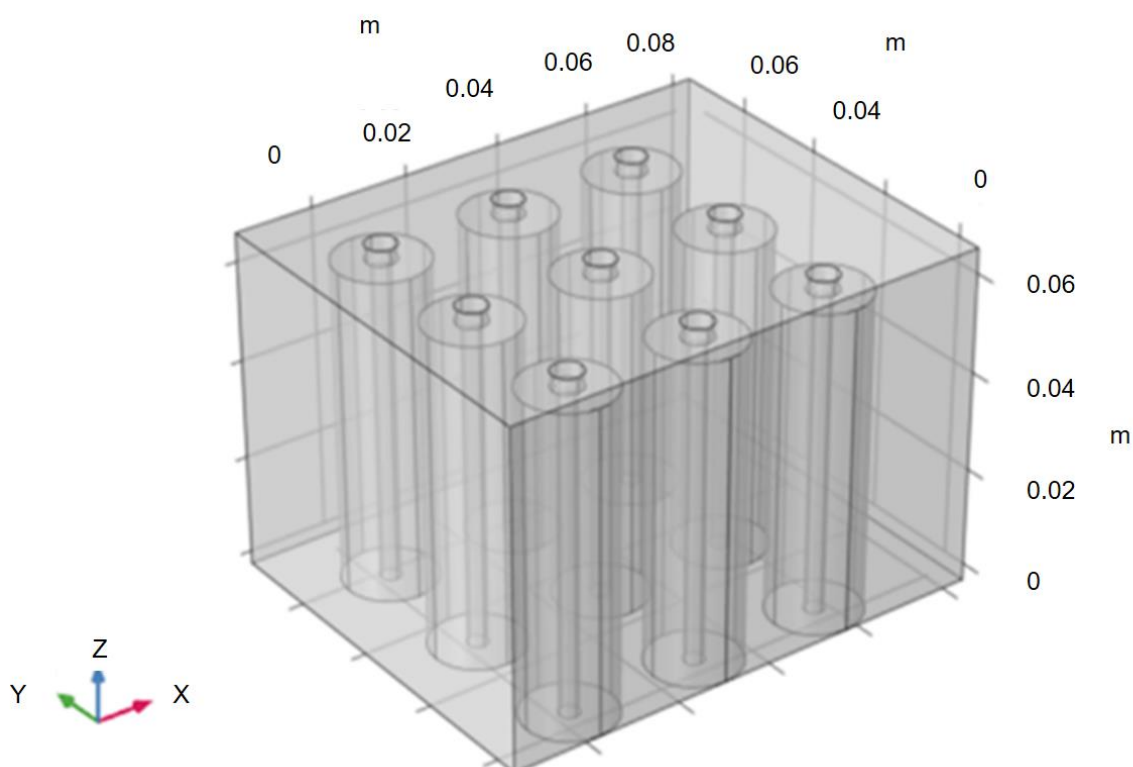
Figure 3.7. 3D model of a battery cells matrix

Four domains (active battery material, battery connector, mandrel and the flow compartment) are associated with the matrix model. Since it was confirmed that the effect of the battery

canister on the heat transfer of a cell is negligible, the canister domain is not used with the 3D model.

The 1D model and the 3D model are coupled. Boundary conditions as in the previous modelling are applied to the battery matrix. The properties (air density, the volumetric flow rate and etc.) of the air flow are not assumed to vary with temperature. However, the fluid flow is allowed to influence the heat transfer rate.

The temperature distribution within the system exhibits a range between 49°C and 73°C, indicating significant thermal variations. Surrounding air temperatures fluctuate between 25°C and 54°C, illustrating the dynamic thermal environment. Notably, the battery cells positioned farthest from the inlet register the highest temperatures within the matrix, suggesting localized heat accumulation (i.e. gathering the heat to a certain zone or the region) in these regions. This observation underscores the importance of considering spatial heat transfer dynamics and thermal gradients when analysing the system's thermal performance.
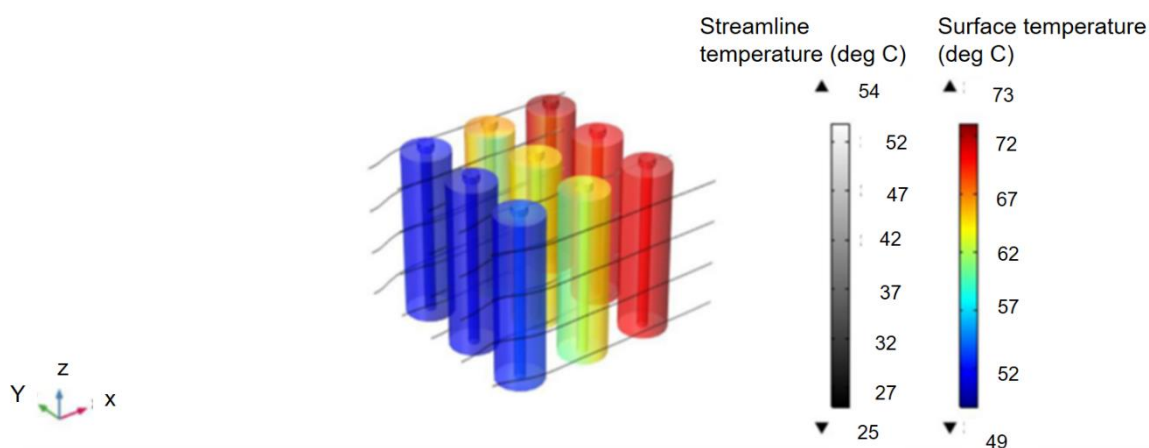
Figure 3.8. Temperature distribution results at 1500 s

The matrix was then extended for a battery module. Generally, a Li-ion battery consists of repeated modules, and the virtual analysis is only focused on the elementary cell array. A linear layout, where cells are ordered in parallel rows, is widely used. In another layout, the cells are arranged in a zigzag pattern, as shown in Figure 3.9. According to industry and the related literature, it is mentioned that the offset structure is commonly used for cylindrical elements while the parallel shape is mostly used for the soft pouch type cells.

The CFD simulation was conducted using a module containing 59 cells, and the space dimension of the battery cell unit is fixed. Moreover, the inlet and outlet sections have already been defined. The airflow go towards to the positive X direction and the simulation reproduces

the thermal behaviour of a battery module under the same operating conditions as mentioned above.
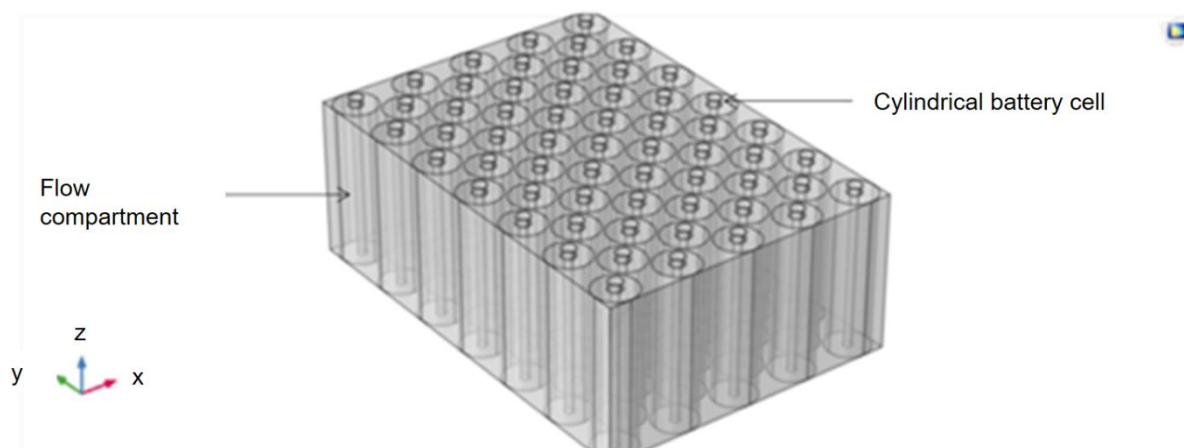
Figure 3.9. Battery module with 59 battery cells
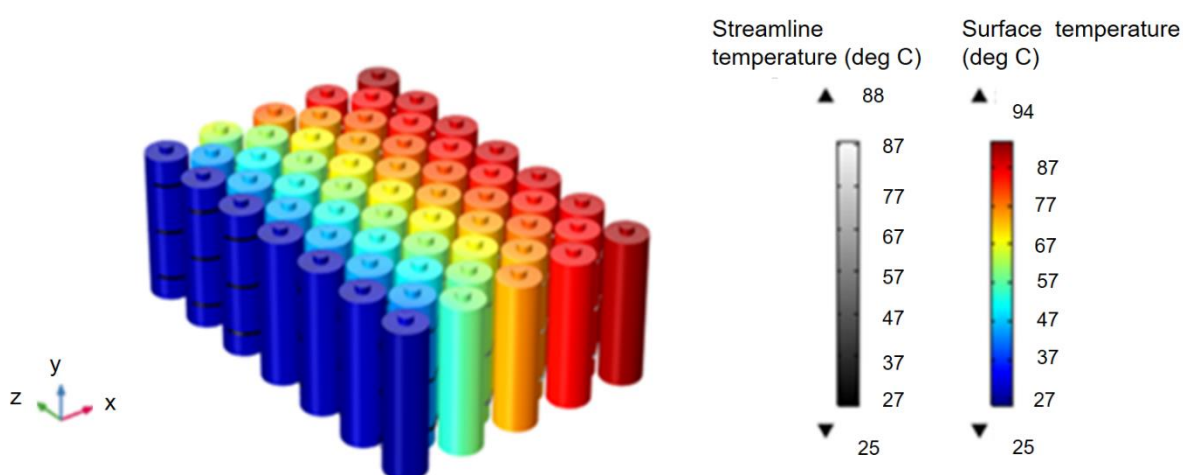
Figure 3.10. Temperature distribution results of a battery module at 7.5C discharge rate after 1500s

Figure 3.10 shows the temperature profile related to the simulation with discharge rate of 7.5 C. The maximum cell temperature simulated after 1500s is 94 °C while the maximum value of stream line temperature is 88 °C.

3.4.1 Effect of cell geometry configuration

It was decided to investigate the variety in the battery cell geometries that are currently used in the automotive industry in terms of both cooling capacity and space utilisation effect [19]. In order to investigate this, simulations were conducted considering 24 battery cells in different arrangements. In the automobile industry, a battery module typically consists of between 12 to 24 battery cells [70], [71]. Four different cell structures were considered: 1×24, 3×8 and 4×6 rectangular arrays and a hexagonal arrangement [19], [72], [73]. The hexagonal

arrangement did not comprise of 24 cells as was the case with the three rectangular arrangements but instead it comprised of 19 cells. The 19-cell hexagonal arrangement considers the space utilisation effect [19], [72]. It is because, literatures indicate that hexagonal arrangements (honeycomb structures) are considered as most efficient arrangements in automotive, aerospace and energy industries [19], [72], [74]. Since there is a 20% reduction in number of cells when compare to the 24 cells arrangement, it was checked that whether it was caused for the temperature reduction in 19 cells hexagonal arrangement by conducting simulations for 18 cells rectangular array and by comparing with 19 cells hexagonal arrangement. Then the results reported that even with 18 cells rectangular array has a maximum temperature (91.2 $^\circ$C) which is larger than the maximum temperature of 19 cells hexagonal structure (82.3 $^\circ$C).

Furthermore, the difference in cooling performance between rectangular and hexagonal packing arrangements can be attributed to several factors inherent to their respective geometries. Hexagonal packing typically results in a more compact configuration, exposing a greater surface area to the surrounding environment and facilitating more efficient heat transfer through convection. Additionally, the uniformity of hexagonal packing minimizes air gaps between cells, reducing thermal resistance and enhancing heat transfer efficiency. The interconnected pathways formed by adjacent cells in a hexagonal arrangement allow for more even and rapid heat dissipation throughout the structure compared to rectangular arrangements, which may have less direct pathways and are prone to localized hotspots. Moreover, the rounded edges and irregular boundaries of hexagonal arrangements promote smoother airflow and reduce the likelihood of thermal stagnation, while the optimised packing density ensures efficient space utilisation and enhances thermal conductivity. These combined factors contribute to the superior cooling performance observed in hexagonal packing arrangements, underscoring the importance of geometric considerations in optimising thermal behavior.

The same boundary conditions and assumptions which were previously made were applied for all simulations in different cell structures as well.

Figure 3.11 shows the different cell arrangements and the temperature distributions of the battery module at 1500 s. During discharge heat generated of each cell is considered as constant. The self and mutual heating contribute to the rise of battery module temperature.

It is observed that the maximum cell temperature for all four scenarios falls outside the optimal range of 30-40℃, the temperature range that the Li-ion batteries require for better performance [75].

When the cells in the model are arranged in 3×8 structure, the results are almost equal as in the structure of 1×24. The results indicate that the furthest batteries acquire the highest temperature resulting from the combination of heat flux which is flowing with the airflow and the heat generated by neighbouring batteries.

Compared with 1×24 cells arrangement, the cooling capability of 3×8 structure is better as reflected from the maximum temperature difference of 43.7 ℃. The main difference of these two structures is the length of airflow path.

Although the cooling air is heated up as well, the stream flow temperature is less than when compared to 1×24 cell arrangement and which implies that the longer the airflow path, the poorer the airflow cooling ability is. It is because, when airflow paths are extended, air encounters greater resistance due to increased surface contact, resulting in higher pressure drops and reduced airflow velocity. This diminished velocity, coupled with the thickening of the boundary layer along longer pathways, decreases the effective heat transfer coefficient, impeding heat exchange between surfaces and air. Longer paths also disrupt airflow distribution, leading to variations in velocity and temperature across the system, which can result in localised hotspots and overall decreased cooling performance. Furthermore, the prolonged contact time within the system allows air to absorb more heat before exiting, further diminishing cooling effectiveness. While other dimensions of the battery module may also influence airflow patterns and cooling efficiency, the emphasis on airflow path length underscores its significant impact on cooling ability, necessitating careful optimisation for efficient thermal management.

To improve airflow cooling ability, the airflow path should be shortened and for this purpose 4×6 cubic structure was designed. Although the maximum temperature difference of 4×6 arrangement is equal to 45.8 ℃, the temperature distribution pattern follows the same rule as both 3×8 and 1×24 cell arrangement structures.
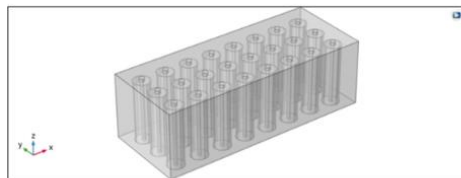
Although the hexagonal arrangement has more free volume than the 4×6 cubic module, the 19-cell hexagonal arrangement demonstrates that the cooling effectiveness of the module is similar to that of 4×6 cubic module.
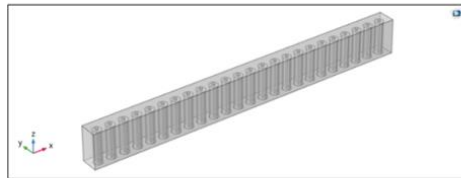
1x24 cells arrangement
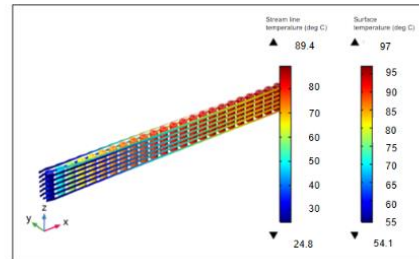
Temperature distribution results at 7.5C discharge rate at 1500s

3x8 cells arrangement
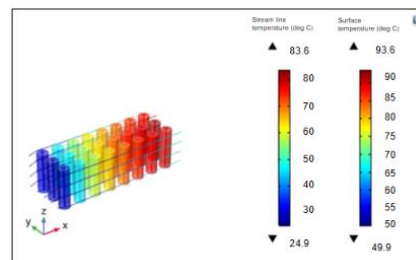
Temperature distribution results at 7.5C discharge rate at 1500s
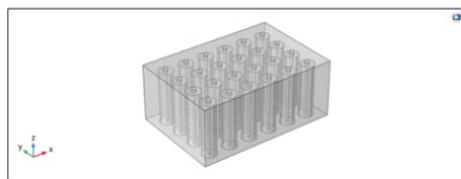
4x6 cells arrangement
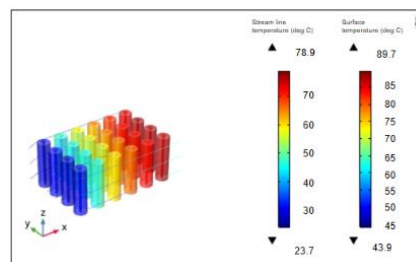
Temperature distribution results at 7.5C discharge rate at 1500s
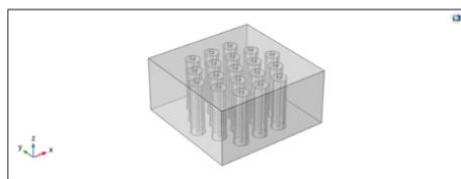
19 Cells hexagonal arrangement
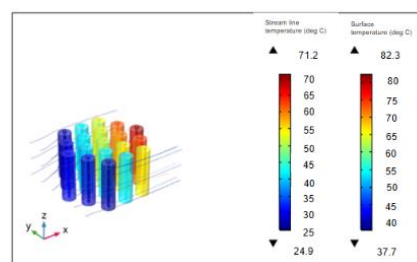
Temperature distribution results at 7.5C discharge rate at 1500s

Figure 3.11. Different cell structures and the temperature distribution results of each at 1500 s

The higher temperatures observed in the simulation, reaching around 60-80°C, are despite the presence of a 0.1 m/s air velocity, which is insufficient for effective cooling. In this case, the focus is on passive cooling rather than active cooling. The datasheet values for Li-ion

battery cells, specifically 18650 cells, assume the presence of active cooling systems that maintain the cells within an optimal operating temperature range of 30-40°C. These active cooling systems typically use liquid or air cooling with much higher velocities, often around 2-5 m/s for air cooling or advanced liquid cooling techniques [19], to effectively dissipate the heat generated by the cells during high power demands and dense packing configurations. The limited air velocity in the simulation highlights the inadequacy of passive or low-velocity cooling methods and underscores the critical role of robust thermal management systems in ensuring battery cells operate within their optimal thermal range, thereby enhancing their performance, safety, and longevity.

Generally, the temperature distributions of batteries are quantitatively dependent on both cell arrangement type and the inter–cell distance. However, when designing a battery module, it is required to consider the space utilisation as well since the space occupation rate is another important scenario for a battery module[19]. The space occupation rate is calculated using following formula and can be defined as the ratio of used space from the battery cells to the total amount of space that is available.

$$Space\ occupancy\ rate(\zeta)$$
$$= \frac{space\ occupied\ by\ battery\ cells}{Total\ space} \quad (25)$$

The total volume of each module is determined using the outer box dimensions (length, width, and height) that enclose all the cells. For the 19-cell hexagonal design using 18650 Li-ion cylindrical battery cells, the outer box has dimensions of 30 cm x 30 cm x 10 cm, resulting in a total volume of 9000 cm³. Each 18650 cell, with a diameter of 1.8 cm and height of 6.5 cm, occupies 16.6 cm³. With 19 cells, the total volume occupied by cells is 315.4 cm³, leaving 8684.6 cm³ of vacant space. The occupancy rate is calculated as the ratio of the cell volume to the total volume, which for the 19-cell design is approximately 3.5%. Despite a higher occupancy rate, the hexagonal arrangement results in a larger vacant space due to the geometry of the outer box.

The characteristics of all structures of battery module mentioned above with the airflow are summarised in Table 3.1

Table 3.1. Thermal and volumetric characteristics of different cell arrangements battery module with the airflow at 1500 s

Cell arrangement strategy	Highest temperature T_{max} (ºC)	Lowest temperature T_{low} (ºC)	Maximum temperature difference ΔT (ºC)	Average temperature $\tilde{T}$ (ºC)	Space occupancy rate ζ (100%)
1x24 cells	97.0	54.1	42.9	75.6	2.399
3x8 cells	93.6	49.9	43.7	71.8	2.802
4x6 cells	89.7	43.9	45.8	66.8	2.836
19 cells hexagonal	82.3	37.7	44.6	60.0	3.543

The results indicate that when considering the cooling efficiency with X- directional flow, 4×6 cubic arrangement is a good choice. However, 19 cells hexagonal arrangement is better when considering both cooling capacity and the space utilisation since hexagonal arrangement shows the highest occupancy rate.

3.4.2 Effect of inter-cell distance

In order to investigate the effect of inter-cell distance, a 19-cell hexagonal arrangement was used. The inter-cell distance of the cell arrangement was changed from 0.054 to 0.027 m to a no-gap situation by keeping all other boundary conditions constant, and simulations were conducted. The 19-cell hexagonal arrangement with no-gap is presented in Figure 3.12 . When conducting the simulation for the no-gap situation, in addition to the convection heat transfer and the heat generation inside the cell, the thermal conductivity from adjacent cells with both convection heat transfer and heat generation was considered. As indicated in results (Figure 3.13), when there is no gap between cells, the average temperature is higher when comparing to the structure which has the gap between battery cells.
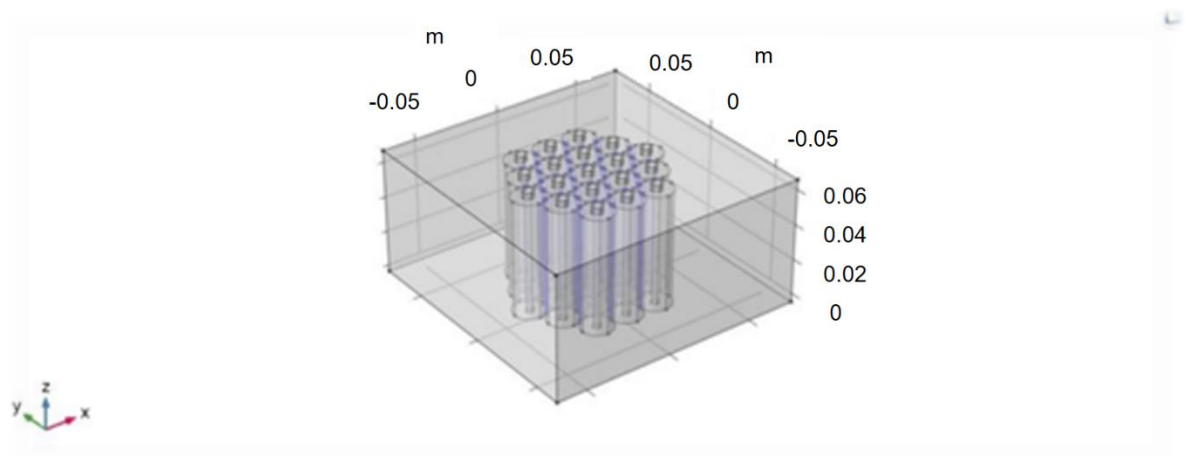
Figure 3.12. 19 cells-hexagonal arrangement with no gap between cells
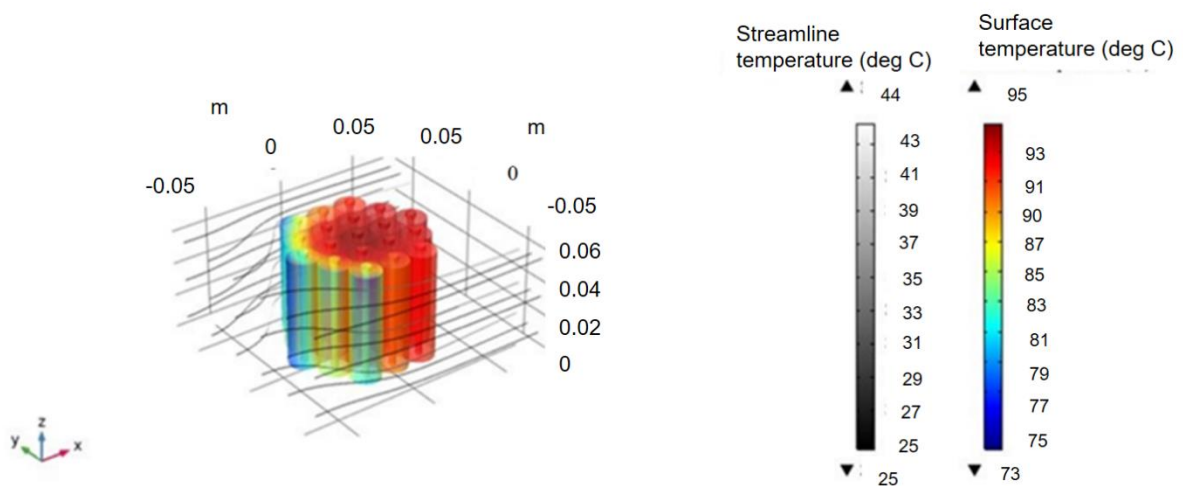
Figure 3.13. Temperature distribution results at 1500s

In order to further analysis, the temperature distribution was mapped (red line in the figure) along with the line between x=-0.045 m and x=0.045 m as shown in Figure 3.14.

Temperature distribution along with the line of x=-0.045 and x=0.045 m

The inter cell distance =0 m at 1500 s with surface edge to surface edge thermal conductivity
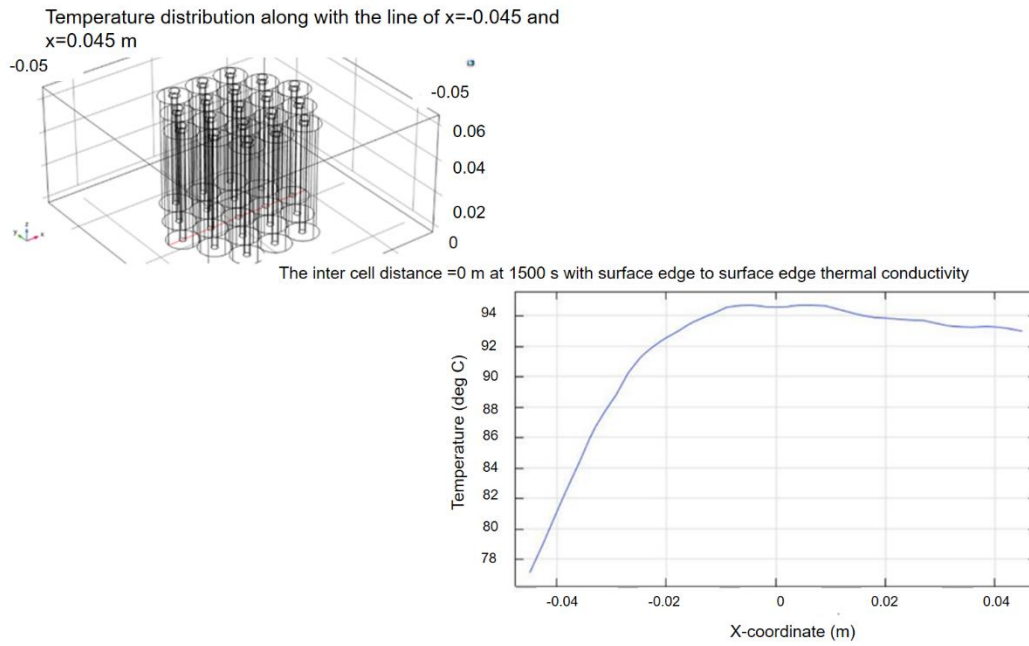
Figure 3.14. Temperature distribution mapping along the x-axis at z=0 and y=0.02 planes

When the gap demonstrates the standard gap of 0.027m, the maximum temperature is lower than the maximum temperature of no gap scenario. The results with the temperature mapping along the X-axis for gap of 0.027 m can be presented as follows.
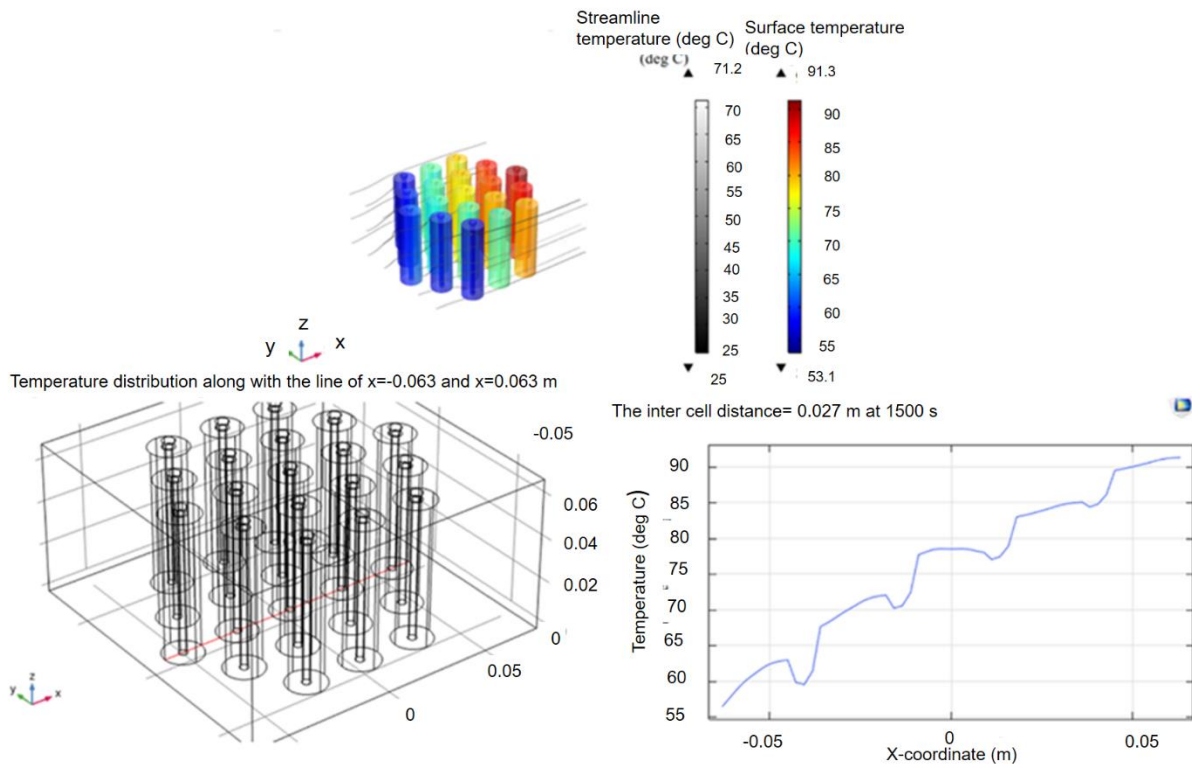
Figure 3.15. Temperature distribution results for gap 0.027m

As indicated in Figure 3.16, the gap of 0.054 m has the lowest average temperature of three scenarios and those results confirms that when there is the gap, more air occupies the space and it will reduce the mutual heating between battery cells.
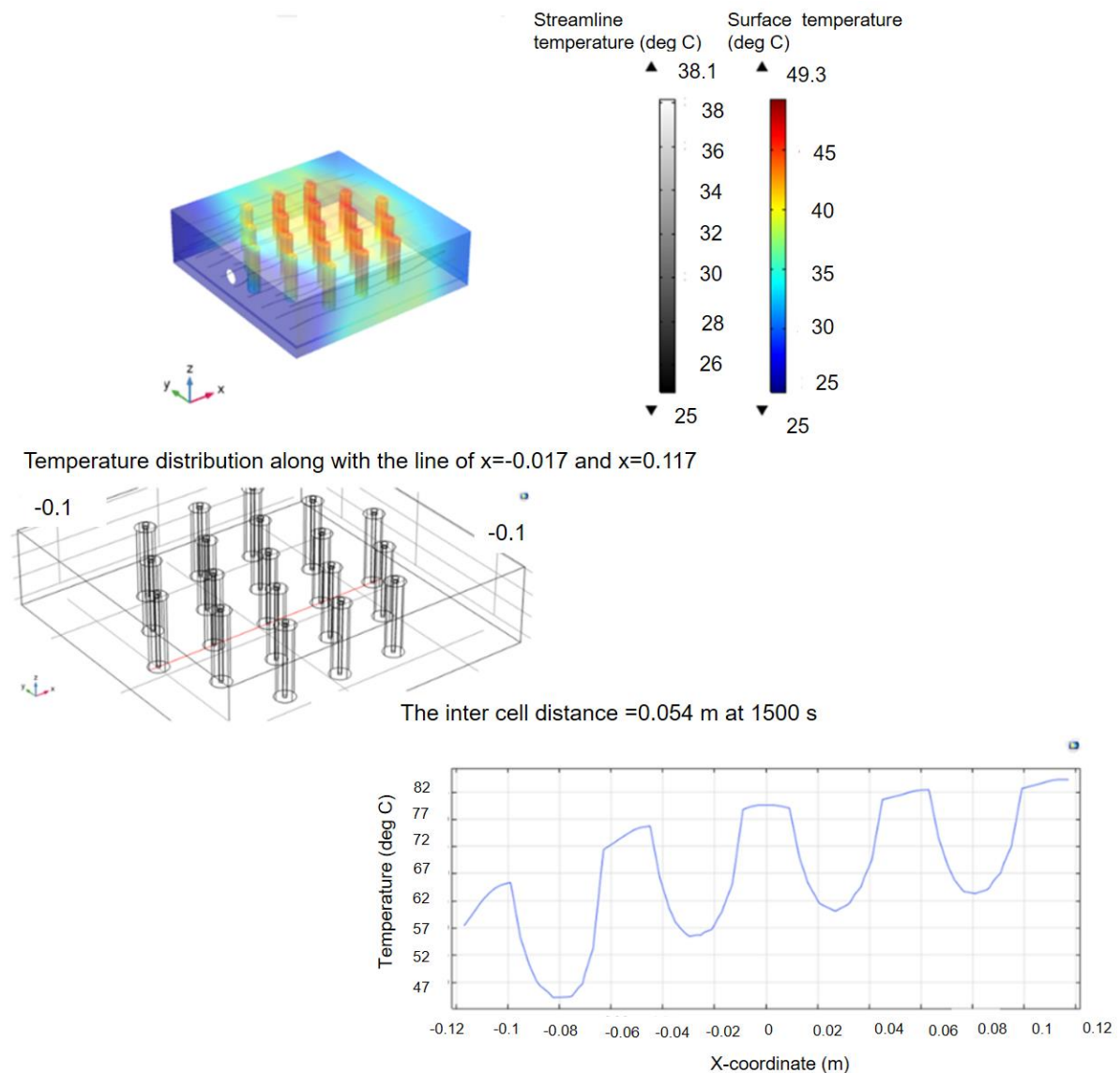
Figure 3.16. Temperature distribution results for 0.054 m

3.5 Discussion and conclusion

In this study, the thermal performance of Li-ion battery module is discussed by considering both analytical and simulation methods. Assumptions of the lumped model are applied in the analytical method of a single cell. Simulations are conducted by coupling both 1 D and 3 D model. In addition, thermal performance analyses are performed for different cell structures and the arrangement and structures include 1×24, 3×8, 4×6 arrays rectangular arrangements and 19 cells hexagonal arrangement. Among all structures discussed in the study 4×6 cubic

structure is identified as the best choice in terms of the cooling capability although the inlet and outlet size of the specified arrays are slightly different from each other. However, 19 cells hexagonal arrangement is identified as the best choice in terms of both cooling capability and space utilisation effect. Therefore, it is selected for further investigations throughout the project and the effect of inter-cell distance is also investigated. Results confirmed that the having a gap between battery cells reduces the mutual heating effect and increases the cooling effectiveness.

4 Experimental validation of heat transfer model for Li-ion battery module using a metallic enclosure

4.1 Experimental rig

### 4.1.1 Rig design and implementation

Since the heat transfer model and the custom jig are supposed to be used in the process of validating the composite enclosure, initially the heat transfer model was validated with the custom jig experimentally.

As stated in the previous section, and since it is confirmed by the literature [19], [72], and [73], the 19 cells hexagonal arrangement was considered the optimal solution in terms of both space utilisation and cooling capacity. Therefore, it is used in the experimental validation process.

The custom jig has the capability of handling three main scenarios for 19 cells hexagonal arrangement including no gap scenario, the gap =0.027 m and the gap =0.054 m. These gaps are equivalent to the gaps used in the commercially available battery module. Here, those three scenarios are considered to investigate the effect of inter cell distance on the heat transfer, and in the situation the effect which will occur due to the changing space on space occupation rate is not considered. The jig consists of main 5 components as shown in Figure 4.1 :

- A Corderite material base, as it has extremely low thermal conductivity (2.5 W/mK) leading to minimum heat loses through the base
- A steel support, in order to contain all the electrical components (relays and wires) for the heating element
- A 24 V DC bench power supply. This was selected since each heating elements are connected in parallel and the rated voltage of a heating element is 24 V DC,
- The main power supplies
- 19 cylindrical heating elements. They have the same dimensions of Li-ion batteries including the 18 mm diameter and 65 mm height.

Experimental validation of heat transfer model for Li-ion battery module using a metallic enclosure
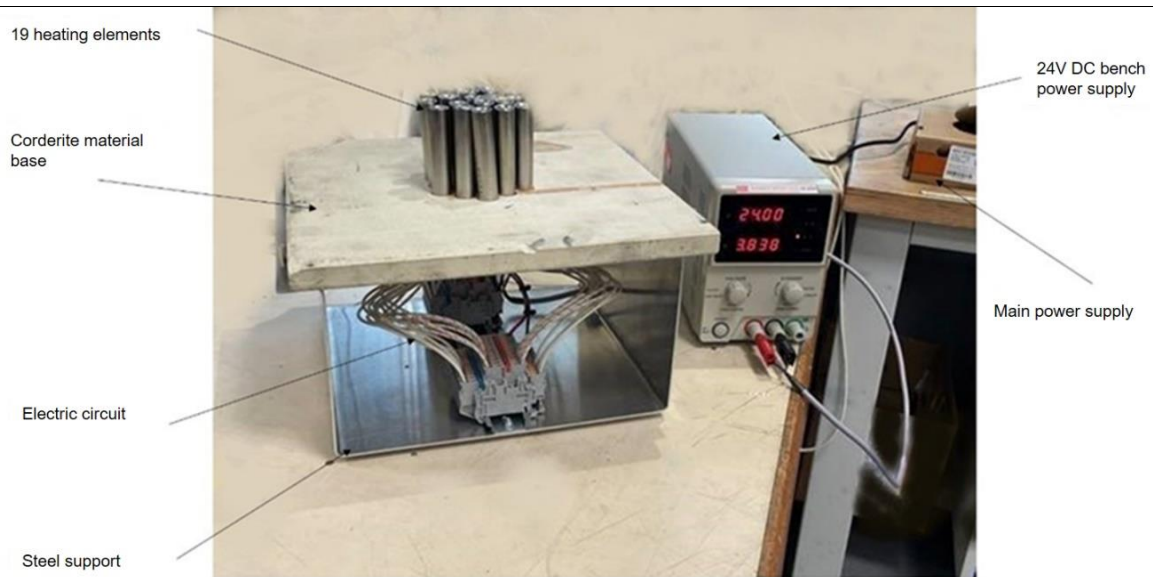
Figure 4.1. Experimental rig

In the custom jig, two bases were fabricated to handle the three different gap scenarios as shown in Figure 4.2.

Corderite material base for no gap scenario
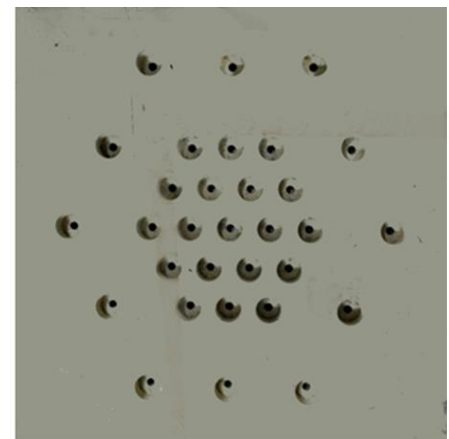
Corderite material base for standard gap scenario and double gap scenario

Figure 4.2. Corderite material base for custom jig

Under the benchmark study, experiments were performed to measure the temperature rise and distribution in a real battery cell during typical charge and discharge cycles using precise thermocouples, following methodologies established in relevant literature [81], [82]. These experiments were complemented with thermal simulations to model the battery cell's thermal behaviour accurately, aligning with approaches used by Chen et al [83]. Following this, the cartridge heaters were calibrated to replicate the observed temperature profiles by adjusting power input and employing techniques like pulse-width modulation, similar to the techniques

described by Prada et al. (2012). Temperature rise tests were then conducted, comparing the thermal responses of the battery cell and the cartridge heater to ensure that the heater could mimic the cell's heating characteristics effectively. This comprehensive approach, grounded in established research, validated the use of cartridge heaters as accurate surrogates for battery cells in the studies.

4.1.2 Power distribution to emulate the battery operation

The DC heating element has the rated voltage of 24 V and a rated wattage of 5W. Generally, an 18650 Li-ion battery cell generates 2W-3.5W and it was planned to conduct experiments at 0.14 ,0.56,1.26 and 2 and 3.5 W powers. Since the recommended heaters are dealing with DC rather than AC, it is not required to be concerned about the reactive component of the power supply. Therefore, the basic equation (see Equation (26)) can be used for the electric current calculation.

$$P = VI \qquad\qquad (26)$$

where, P is denoted as power (W) and V is for voltage (V), I represents the current (A).

The required maximum current is 3.5 W/24 V=0.15 A. However, the heaters are rated for 5W /24 V=0.21. Therefore, since the maximum current which is required by the circuit is less than the rated current, the proposed heaters are safe for the application. The relevant electrical circuit is shown in Figure 4.3.

Experimental validation of heat transfer model for Li-ion battery module using a metallic enclosure

The maximum current through heating element (I)=0.21 A
The resistance of the heating element (R) = 115.2 Ω
Rated power for a heating element (P)= 5W
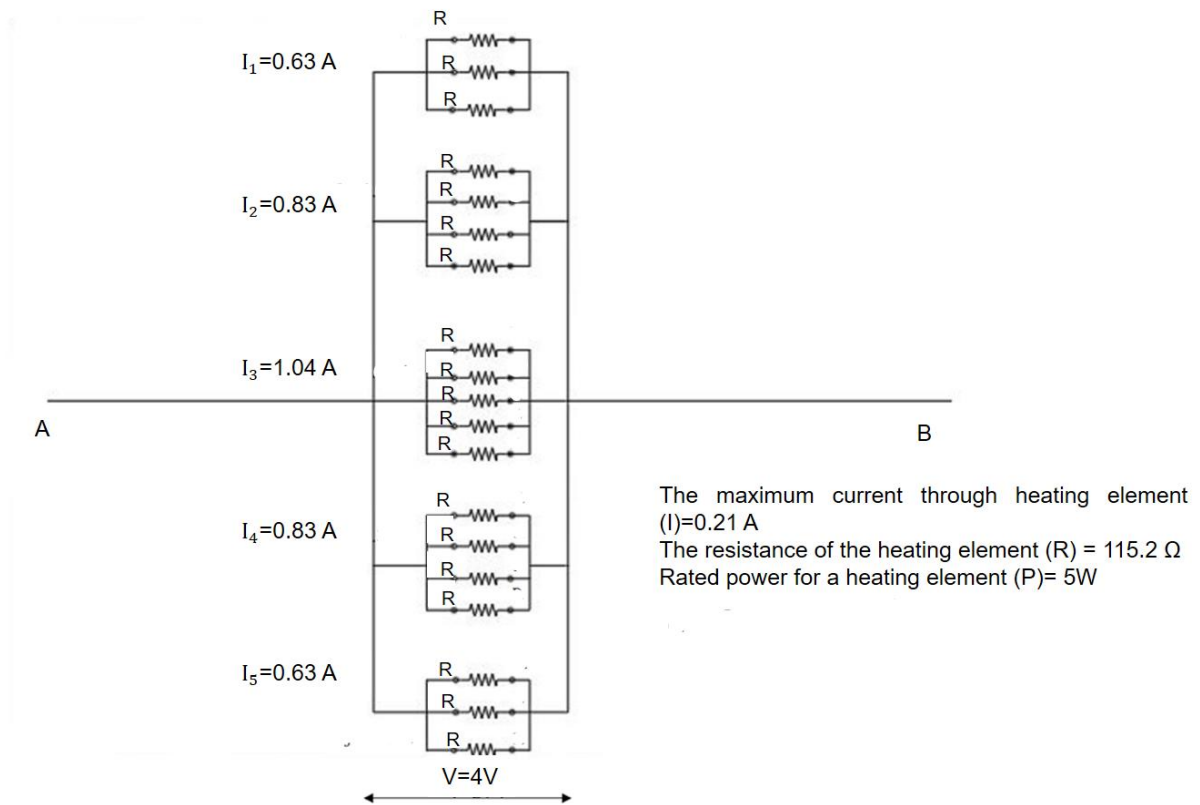
Figure 4.3. Electrical circuit diagram for experimental rig

The power calculations for a heating element, 19 heating elements and the relevant electrical circuit can be figured out as follows.

Table 4.1. Electrical calculation for single heating element

Voltage (V)	Current (A)	Power output from the heating element
4.0	0.03	0.14
8.0	0.07	0.56
12.0	0.10	1.26
15.2	0.13	2.00
20.1	0.17	3.50

Table 4.2. Electrical calculation for 19 heating elements

Voltage (V)	Current (A)	Power output from the heating element
4.0	0.65	0.14

8.0	1.33	0.56
12.0	1.98	1.26
15.2	2.51	2.00
20.1	3.31	3.50

4.2 Temperature measurements without airflow-no enclosure

Initially, the experiments were done on the custom jig without any enclosure and the airflow supply for the purpose of validating the simulation results. The experiments were done for three configurations by considering the effect of inter -cell distance, including the no-gap situation, the situation with the standard-gap, and the scenario of twice the gap as standard.

4.2.1 Effect of inter-cell distance

- Measurements for no-gap scenario

As shown in 4.4, thermocouples are used to take the measurements, and they are positioned on the top surface of the heating element using adhesive tapes. PICO data loggers (see Figure 4.5) and a laptop are used to record the temperature. Measurements were taken for total time of 5400 s including both of the heat up at 1500s and natural cooling after 1500s.
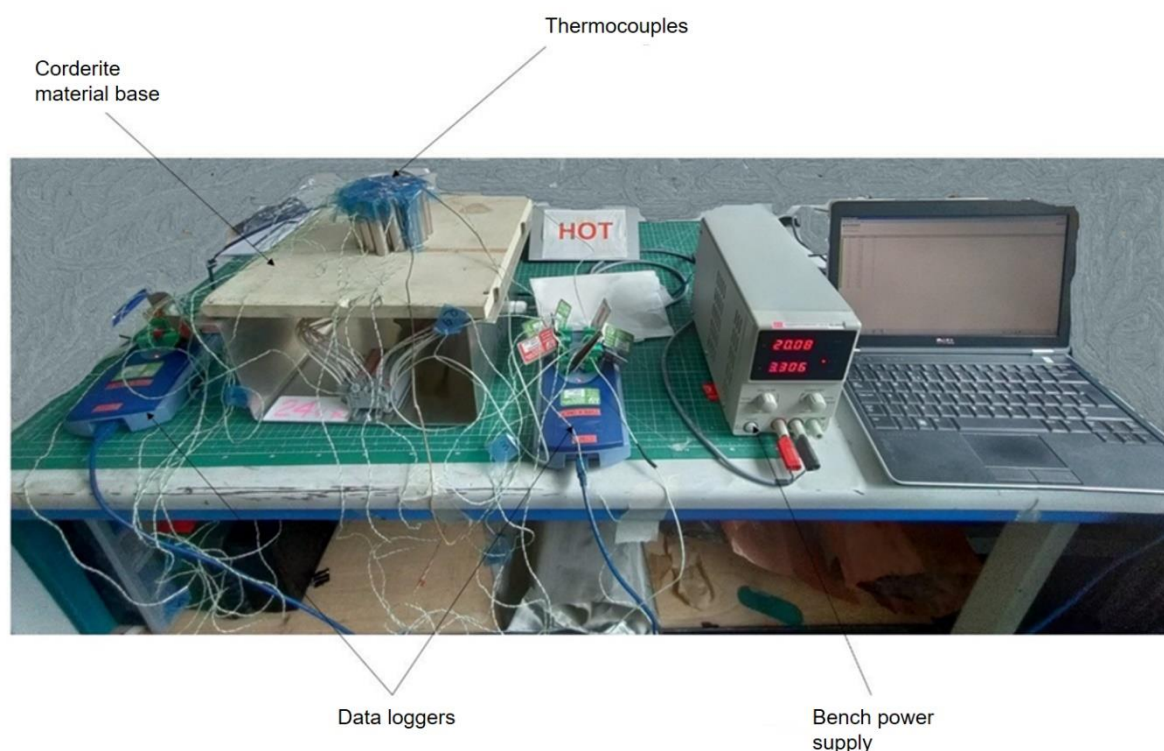
Figure 4.4. Experimental configuration for no gap scenario

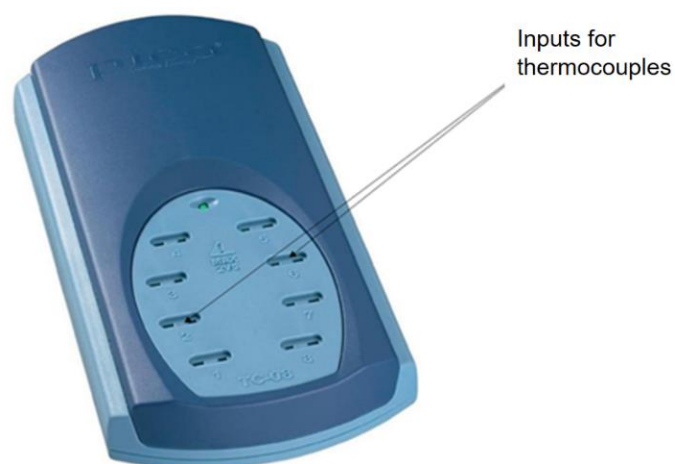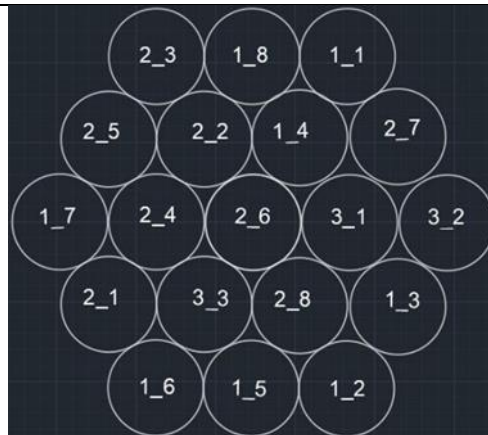Experimental validation of heat transfer model for Li-ion battery module using a metallic enclosure

Before supplying the power to the circuit, it was waited for 60 s at the room temperature (25 °C) to stabilise with the room temperature and then started to supply the power for heating element   for 1500 s. Then waited for the circuit to stabilise at the maximum temperature. It was because, in the simulation, there is a discharge at 1500 s for the battery module. However, the stabilised maximum temperature was found at around 1600-1700 s. Once the circuit reaches its stabilised maximum temperature (i.e. The maximum temperature is always depend on the amount of heating of heating elements, and the maximum temperature of the heating element and a battery cell has an average value which is closer to 83%) , the power supply is stopped, and the behaviour of temperature decrement is also recorded. In order to achieve the repeatability of the experiments, three tests were conducted.

In order to record the temperature, data loggers are used. Generally, a PICO data logger has 8 inputs for 8 thermocouples and for the experiment, three data loggers and 19 thermocouples are used. Therefore, the thermocouples are numbered with the combination of relevant data logger and the relevant thermocouple input. For an example, 1_1 thermocouple means the thermocouple which was fixed to the 1st input of the 1st data logger. As similarly 19 thermocouples were numbered as 1_1,1_2,1_3,1_4,1_5,1_6,1_7,1_8,2_1,2_2,2_6, 2_7, 2_8,3_1,3_2 and 3_3.

Inputs for thermocouples

Figure 4.5. The data logger

Experimental validation of heat transfer model for Li-ion battery module using a metallic enclosure

Figure 4.6. The configuration of thermocouples at the experiment

The configuration of the thermocouples used in the experiment is shown in Figure 4.6 .Initially, the experiments were run without the airflow supply.

The plots that are on the left side of the Annex 1 indicate the temperature distribution up to 1600-1700 s. (i.e., The time at which the maximum temperature is achieved), and the plots that are on the right side demonstrate the complete cycle of heating and cooling of elements. Measurements were taken using K-type thermocouples, and they have an accuracy of ±2.20 °C or ±0.75%. K-type thermocouples are used because they provide the most accurate temperature measurements, measuring up to 1300 °C.

Table 4.3 shows the maximum temperatures recorded from each heating element across three experiments. Average maximum temperature was presented with the standard error and the standard error was calculated using the Equation 27 .

$$Standard\ error = \frac{Standard\ deviation\ of\ the\ temperature}{\sqrt{total\ number\ of\ experiments}} \quad (27)$$

Table 4.3. The maximum temperature of each heating element at the end of heating cycle

Thermocouple	Experiments			
	Experiment 01	Experiment 02	Experiment 03	

Experimental validation of heat transfer model for Li-ion battery module using a metallic enclosure

	Temperature (°C)	Temperature (°C)	Temperature (°C)	Average Temperature (°C)
1_1	70.2	77.7	88.1	78.7
1_2	79.6	84.3	85.7	83.2
1_3	87.5	92.5	89.4	89.8
1_4	92.1	97.4	98.1	95.9
1_5	75.2	79.6	79.0	77.9
1_6	68.2	71.4	72.8	70.8
1_7	66.7	84.6	81.3	77.6
1_8	73.2	77.4	76.7	75.8
2_1	84.1	97.9	89.6	90.5
2_2	93.1	96.2	99.3	96.2
2_3	77.2	80.7	82.9	80.2
2_4	93.8	99.5	100.4	97.9
2_5	68.0	72.3	73.8	71.4
2_6	98.0	106.0	105.4	103.2
2_7	80.1	81.9	85.3	82.4
2_8	88.4	90.7	92.4	90.5
3_1	94.4	99.8	101.8	98.6
3_2	83.5	96.0	92.7	90.8
3_3	88.4	96.2	94.2	93.0

The maximum temperature which is achieved by a heating element was recorded in the centre one (i.e. Thermocouple 2_6) for all three experiment and has the average temperature of 103.28 ℃.

- Measurements for standard-gap

In order to measure the temperature of the heating elements, their orientation is changed by using the fabricated holes in the Corderite material base (see Figure 4.7). However, apart from the orientation, all other parameters and the experimental procedure are the same as in the experiments for the no-gap situation. Three experiments were conducted to determine the repeatability of the experiments, and the data were recorded using the data loggers and the computer using the K-type thermocouples which have a measurement accuracy of 2.20 °C ±0.75%.

Experimental validation of heat transfer model for Li-ion battery module using a metallic enclosure

Figure 4.7. Heating elements with the standard gap

The configuration of the thermocouples in the experiment is shown in Figure 4.8. The temperature distribution along with the time for three experiments are shown in Annex 2 .
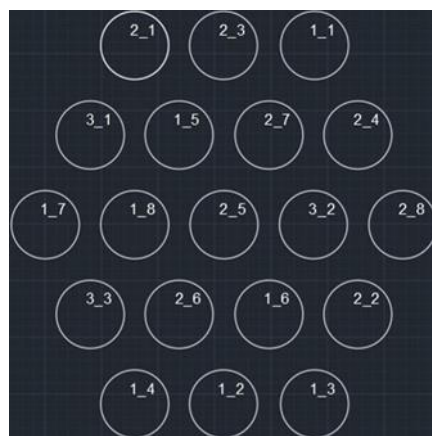
Figure 4.8.Configurations of thermocouples at the experiment

The plots that are on the left side of Annex 2 , indicate the temperature distribution up to the time at which the maximum temperature is achieved, and the plots that are on the right side demonstrate the complete cycle of heating and cooling of elements. Measurements were taken using K-type thermocouples, and they have an accuracy of 2.20 °C ±0.75%. Table 4.4 shows the maximum temperature recorded from each heating element across three experiments.

Table 4.4. The maximum temperature of each heating elements at the end of heating cycle

Thermocouple	Experiments	

Experimental validation of heat transfer model for Li-ion battery module using a metallic enclosure

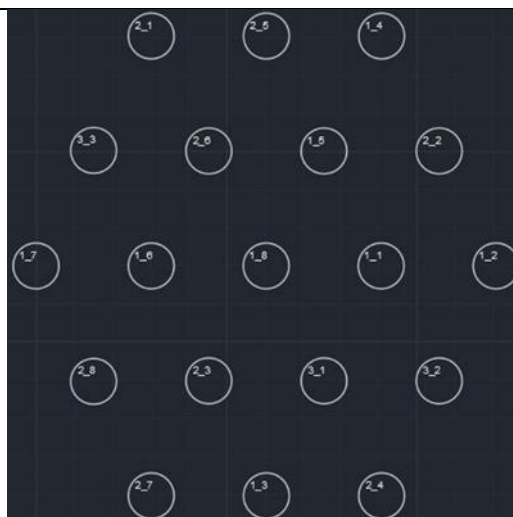|	Experiment 01 Temperature (°C)	Experiment 02 Temperature (°C)	Experiment 03 Temperature (°C)	Average Temperature (°C)
1_1	59.3	59.2	59.1	59.2
1_2	53.8	50.5	53.2	52.5
1_3	54.4	51.7	45.0	50.4
1_4	52.2	49.8	50.8	50.9
1_5	59.3	67.0	67.4	64.6
1_6	62.6	60.6	61.5	61.6
1_7	54.6	53.6	54.1	54.1
1_8	71.2	69.3	68.9	69.8
2_1	56.5	54.5	55.3	55.4
2_2	58.9	55.9	57.3	57.4
2_3	51.8	45.9	51.3	50.0
2_4	55.6	54.0	55.4	55.0
2_5	73.7	71.9	72.6	72.7
2_6	67.0	65.4	65.5	66.0
2_7	64.4	63.2	63.9	63.8
2_8	55.6	53.9	55.3	54.9
3_1	67.1	65.1	65.6	66.0
3_2	71.2	69.2	70.6	70.3
3_3	63.6	61.3	61.7	62.2

The maximum temperature that is achieved by a heating element was recorded in the centre one (i.e., Thermocouple 2_5) for all three experiments and has an average temperature of 72.7 °C.

- Measurements for twice the gap between heating elements

Apart from the orientation, all other parameters and the experimental procedure are the same as in the experiments for the no-gap situation and the standard-gap situation. Three experiments were conducted for the repeatability, and the data were recorded using the data loggers and the computer using the K-type thermocouples, which have a measurement accuracy of 2.20 °C ±0.75%.

The configuration of the thermocouples in the experiment is shown in Figure 4.9

Experimental validation of heat transfer model for Li-ion battery module using a metallic enclosure

Figure 4.9. The configuration of thermocouples at the experiment

The plots which are at the left side of the Annex 3, indicates the temperature distribution up to 1600-1700 s. (i.e. The time which the maximum temperature is achieved) and the plots which are at the right side demonstrate the complete cycle of heating and cooling of elements. Measurements were taken using K-type thermocouples and they have the accuracy of 2.20℃ ±0.75%. Table 4.5 shows the maximum temperature recorded from each heating element across three experiments.

Table 4.5. The maximum temperature of each heating element at the end of heating cycle

Thermocouple	Experiments			Average
	Experiment 01	Experiment 02	Experiment 03	Temperature
	Temperature	Temperature	Temperature	(℃)
	(℃)	(℃)	(℃)	
1_1	61.0	67.1	64.0	64.0
1_2	51.8	56.9	57.3	55.3
1_3	55.7	61.6	58.0	58.4
1_4	53.6	59.1	57.6	56.8
1_5	59.1	61.2	61.0	60.4
1_6	61.7	64.8	65.6	64.0
1_7	57.2	60.2	60.0	59.2
1_8	61.9	66.9	65.9	64.9
2_1	60.0	64.5	61.3	61.9
2_2	58.5	61.6	62.0	60.7
2_3	59.9	63.9	62.0	61.9

|				
2_4	52.1	56.1	55.9	54.7
2_5	53.7	56.9	56.9	55.9
2_6	59.5	62.3	62.3	61.4
2_7	57.2	60.2	60.4	59.2
2_8	62.8	66.6	64.6	64.7
3_1	59.9	63.1	63.6	62.2
3_2	59.9	62.6	62.9	61.8
3_3	59.5	62.5	63.4	61.8

The maximum temperature that is achieved by a heating element was recorded in the centre one (i.e., Thermocouple 1_8) for all three experiments and has the average temperature of 64.9 °C.

Results for all three scenarios have shown that the maximum temperature occurs at the centre heating element, the temperature distribution is extremely high for the no-gap scenario, and the results indicate that the temperature varies between 50-103 °C. Both the standard-gap and double-gap scenarios have a lower temperature distribution than the no-gap situation since there is an air gap between each heating element. However, the standard-gap scenario has a broader maximum temperature distribution than the double-gap scenario. (i.e., the temperature distribution for standard-gap scenario is 49-72 °C, and the temperature distribution for double -gap scenario is 54-64 °C). This indicates that the having more air gap between heating elements allows a more uniform temperature distribution among heating elements.

4.2.2 Comparison between experimental results and simulation results

The simulations for no-gap scenario were conducted by considering the same scenario without forced airflow conditions. However, since there is an unavoidable natural convection associated with the real environmental conditions, in the simulation the natural convection, which has 5 W/m^{2}K heat transfer coefficient, is added and the value is the nominal value which is associated with the air. As the initial temperature 25 °C was considered, the simulation results for the no-gap scenario, standard-gap scenario, and the double-gap scenario at 1500s and 2100 s are shown in Figure 4.10.
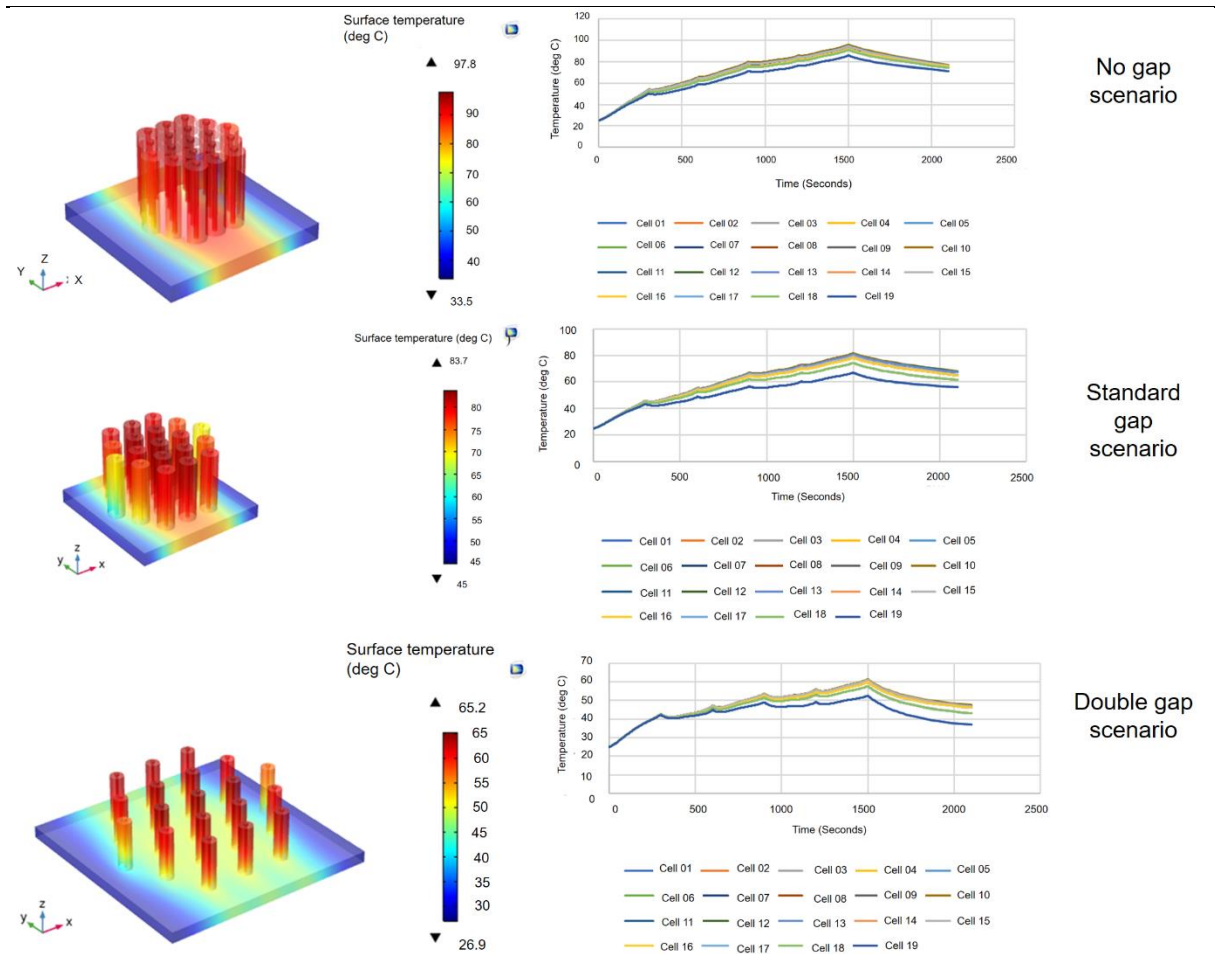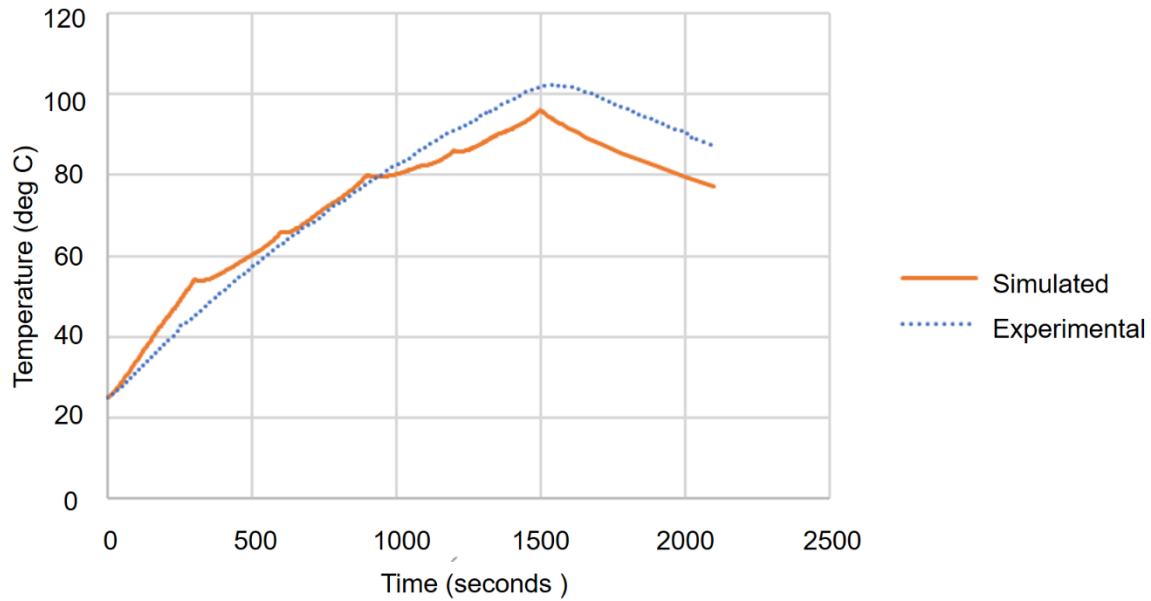
Figure 4.10. Simulation results for three scenarios

The maximum temperature for the no-gap scenario is achieved by both battery cell and the heating element, as recorded in the centre one for both experiments and simulations. The value became 95.9 °C and 103.2 °C for simulation and the experiment, respectively. By considering this fact, the common plot of temperature distribution for both battery cell and the heating element in the no-gap scenario was drawn to the centre element and shown in Figure 4.11.

Experimental validation of heat transfer model for Li-ion battery module using a metallic enclosure

Figure 4.11. Temperature distribution results for both experiment and simulation

One-way analysis of variance (ANOVA) statistical tests are run for the data of both simulation and experimental scenarios by considering each of the three specified heating elements using SPSS software up to the discharge point, and the results can be indicated as follows: One-way ANOVA test is used to determine whether there is any statistically significant difference between the two or more independent groups[54].

Table 4.6. ANOVA test results

Descriptives								
Temperature ºC								
					95% Confidence Interval for Mean (CI)			
	Number of data	Mean	Std. Deviation	Std. Error	Lower Bound	Upper Bound	Minimum	Maximum
Experimental	1583	69.9	23.0	.58	68.8	71.0	25.0	102.3
Simulation	736	67.7	20.7	.76	66.2	69.2	25.0	96.0
Total	2319	69.2	22.3	.46	68.3	70.1	25.0	102.3

Experimental validation of heat transfer model for Li-ion battery module using a metallic enclosure

ANOVA

Temperature ℃

	Sum of Squares	Degree of freedom	Mean Square	F	Sig.(p)
Between Groups	2367.2	1	2367.2	3.761	.329
Within Groups	1152108.9	2317	497.2		
Total	1154476.0	2318			

There was no significant difference between groups as determined by the one-way ANOVA (F (1,2317) =3.761, p=0.329). Descriptives show that the mean value of temperature (69.2±0.46) was no significantly difference between experimental and simulation (p= [0.329], 95% CI = [70.1,68.3]). Therefore, there was no significant difference between experimental and simulation data of the heating element, which is at the center, up to the discharging moment for the no-gap scenario.

The maximum temperature for the standard-gap scenario is achieved by both the battery cell and the heating element, as recorded in the centre for both experiments and simulations. The values became 83.7 ℃ and 78.8 ℃ for simulation and the experiment, respectively. By considering this fact, the common plot of temperature distribution for both battery cell and the heating element at standard-gap scenario was drawn to the centre element, as shown in Figure 4.12.
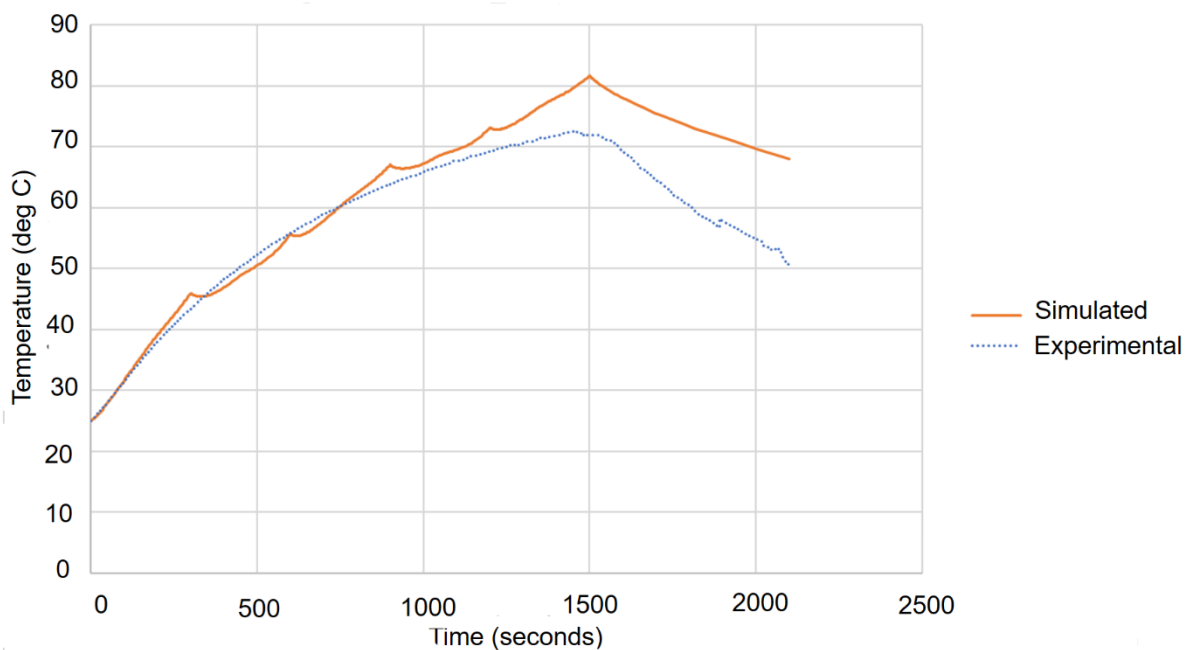
Figure 4.12. Temperature distribution results for both experiment and simulation

Experimental validation of heat transfer model for Li-ion battery module using a metallic enclosure

In order to find out whether there is any significant difference between the experimental and simulation results, the one-way ANOVA statistical test was run up to the discharge moment, and the results of ANOVA test can be figured out as follows.

Table 4.7. ANOVA test results

Descriptives

Temperature °C

	Number of data	Mean	Std. Deviation	Std. Error	95% Confidence Interval for Mean (CI)		Minimum	Maximum
					Lower Bound	Upper Bound		
Experimental	1534	56.8	13.5	.35	56.1	57.5	25.0	72.4
Simulation	689	57.5	16.4	.63	56.3	58.7	25.0	81.6
Total	2223	57.0	14.5	.31	56.4	57.6	25.0	81.6

ANOVA

Temperature °C

|	Sum of Squares	Degree of freedom	Mean Square	F	Sig.(p)
Between Groups	220.0	1	220.0	1.050	.306
Within Groups	465098.3	2221	209.4		
Total	465318.2	2222			

There was no significant difference between groups as determined by one-way ANOVA (F (1,2221) =1.050, p=0.306). Descriptives show that the mean value of temperature (57.0±0.31) was no significantly difference between experimental and simulation (p= [0.306], 95% CI = [57.6,56.4]). Therefore, there was no significant difference between experimental and simulation data of the heating element, which is at the center, up to the discharging moment for the standard-gap scenario.

The maximum temperature for the double-gap scenario is achieved by both the battery cell and the heating element, which were recorded in the center for both experiments and simulations. The values became 65.2 °C and 61.8 °C for the simulation and the experiment, respectively. By considering this fact, the common plots of temperature distribution for both

battery cell and the heating element in the double- gap scenario were drawn to the centre element, as shown in Figure 4.13.
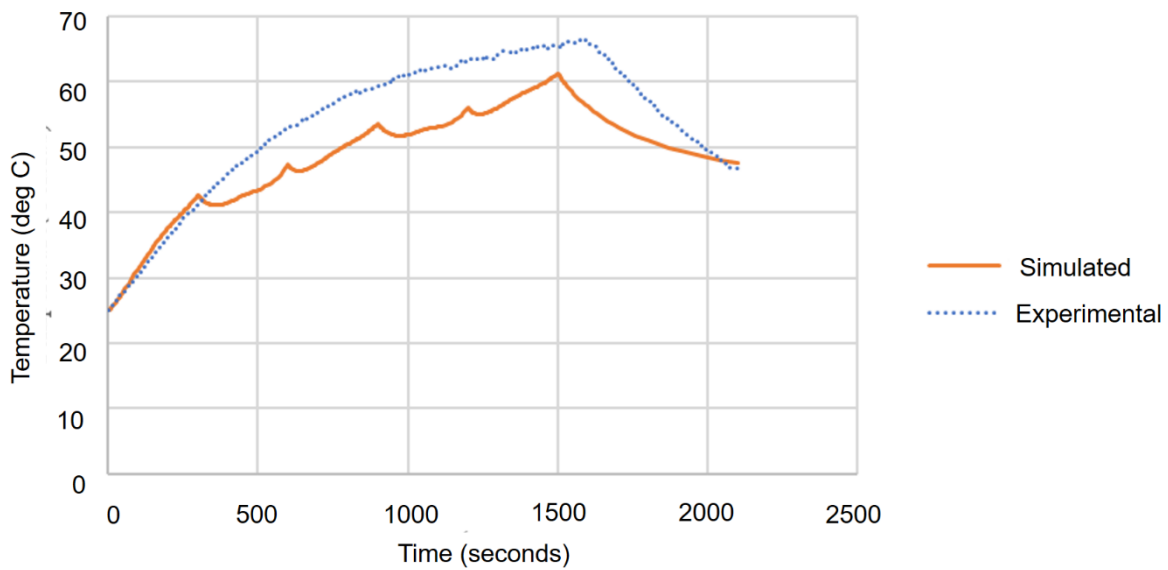
Figure 4.13.Temperature distribution results for both experiment and simulation

As mentioned in previous sections, the one-way ANOVA test was performed for both experimental and simulation results to find out whether there was any significant difference between both results, and the results are shown in Table 4.8.

Table 4.8. ANOVA test results

Descriptives

Temperature ^{o}C

	Number of data	Mean	Std. Deviation	Std. Error	95% Confidence Interval for Mean (CI) Lower Bound	Upper Bound	Minimum	Maximum
Experimental	1632	53.7	11.7	.29	53.2	54.3	25.0	66.5
Simulation	679	47.3	9.9	.38	46.5	48.0	25.0	61.3
Total	2311	51.8	11.6	.24	51.4	52.3	25.0	66.5

Experimental validation of heat transfer model for Li-ion battery module using a metallic enclosure

	Sum of Squares	Degree of freedom	Mean Square	F	Sig.(p)
ANOVA					
Temperature °C					
Between Groups	20101.9	1	20101.9	159.883	<.001
Within Groups	290307.6	2309	125.7		
Total	310409.4	2310			

There was a significant difference between groups as determined by one-way ANOVA (F (1,2309) =159.883, p<0.001). Descriptives show that the mean value of temperature (51.8±0.24) was significantly difference between experimental and simulation (p= [<0.001], 95% CI = [52.3,51.4]). Therefore, there was a significant difference between experimental and simulation data of the heating element, which is at the center, up to the discharging moment.

Considering all the results of the no-airflow scenario, it can be concluded that the simulation results can be almost validated by the proposed test rig and that the test rig can be used for all future analysis. However, there are some differences that exists in between both experiments and simulations. It is because, in the experiment, the environmental conditions are not always constant as in the simulations (i.e. air flow fluctuations, and environmental temperature fluctuations), and because there are some unavoidable issues in fixing heating elements (i.e., they are not vertical as in the simulation and are always associated with a small angle), which will cause for minor deviations in exposed surfaces.

4.3   Temperature measurement without airflow- metallic enclosure

Temperature measurements were conducted for three main scenarios by considering the inter-cell distance effect (including the no-gap scenario, standard-gap scenario, and the double-gap scenario). Three experiments were conducted for the repeatability for each scenario, and the data were recorded using the data loggers and the computer using the K-type thermocouples, which have a measurement accuracy of 2.20 °C ±0.75%. The rig was fully covered using the metallic enclosure and the experiments were run without an airflow. The experimental arrangement can be figured as follows.

Experimental validation of heat transfer model for Li-ion battery module using a metallic enclosure
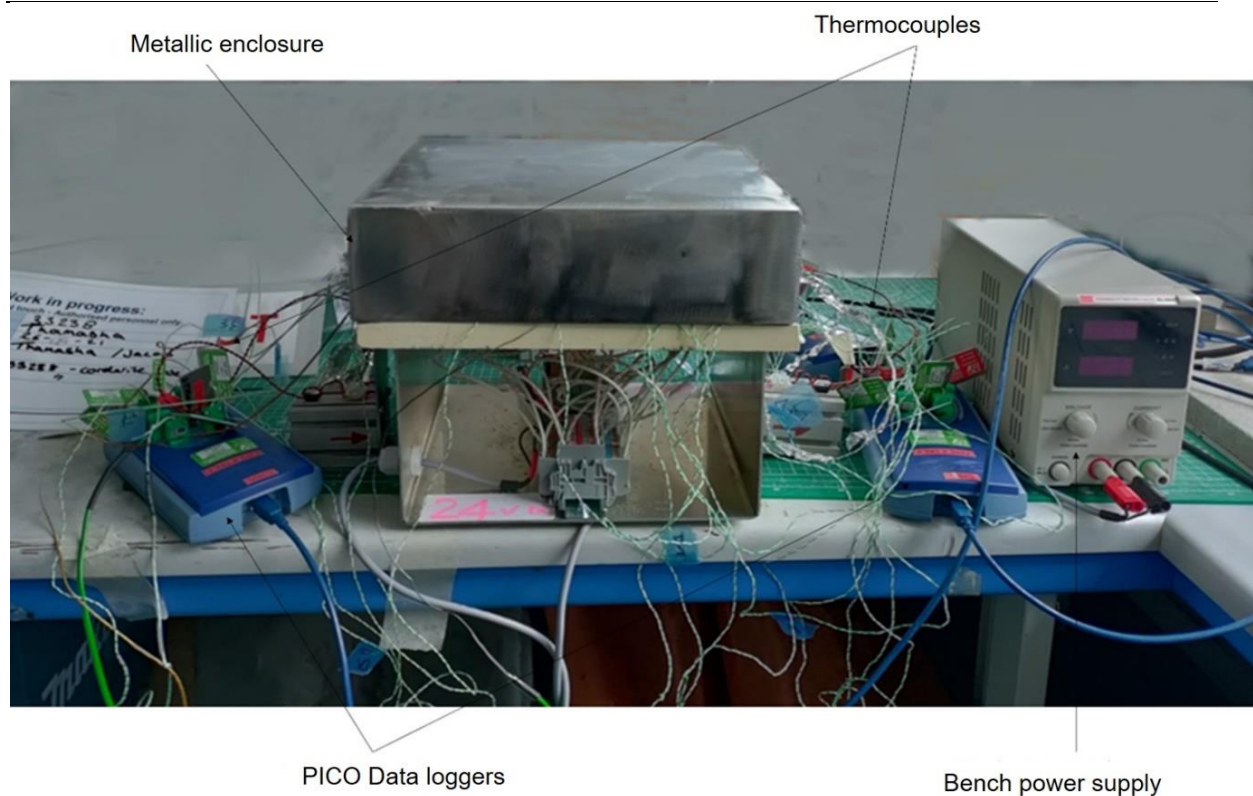

Figure 4.14. Experimental arrangement with the metallic enclosure

The datalogging commenced 60s before supplying the power to the circuit to stabilise with the room temperature and then power was applied to the heating element for 1500 s, then waited for the circuit to stabilise at the maximum temperature. It was because, in the simulation, there is a discharge at 1500 s for the battery module. However, the stabilised maximum temperature was found at around 1600-1700 s. Once the circuit reaches its stabilised maximum temperature, the power supply is stopped, and the behaviour of temperature decrement is also recorded. Annex 4 indicate the average experimental results for all three scenarios.

As shown in Figure 1 in Annex 4 the maximum average temperature that was achieved by a heating element in the no-gap scenario is recorded at 100.9 °C, and it was recorded at the centre element. For standard-gap scenario, the maximum average temperature is 70.2 °C and for double-gap scenario, the value became 66.3 °C. The maximum temperature is achieved at the centre heating element, as in the no-gap scenario. It can be seen that the average maximum temperature is gradually reducing along with the inter-cell distance between the heating elements due to the air gap.

4.3.1 Comparison between experimental results and simulation results

The simulations for no-gap scenario, standard-gap scenario and for the double-gap scenario were conducted with the steel enclosure without having any airflow. 5 W/m²K of convection heat transfer coefficient is added for both the outside and the inside of the enclosure by considering the natural convection heat transfer and the initial temperature of 25 °C. Steel enclosure properties are adopted using the material library from COMSOL. The simulation results for all three scenarios at 1500s and 2100 s are shown in Figure 4.15.
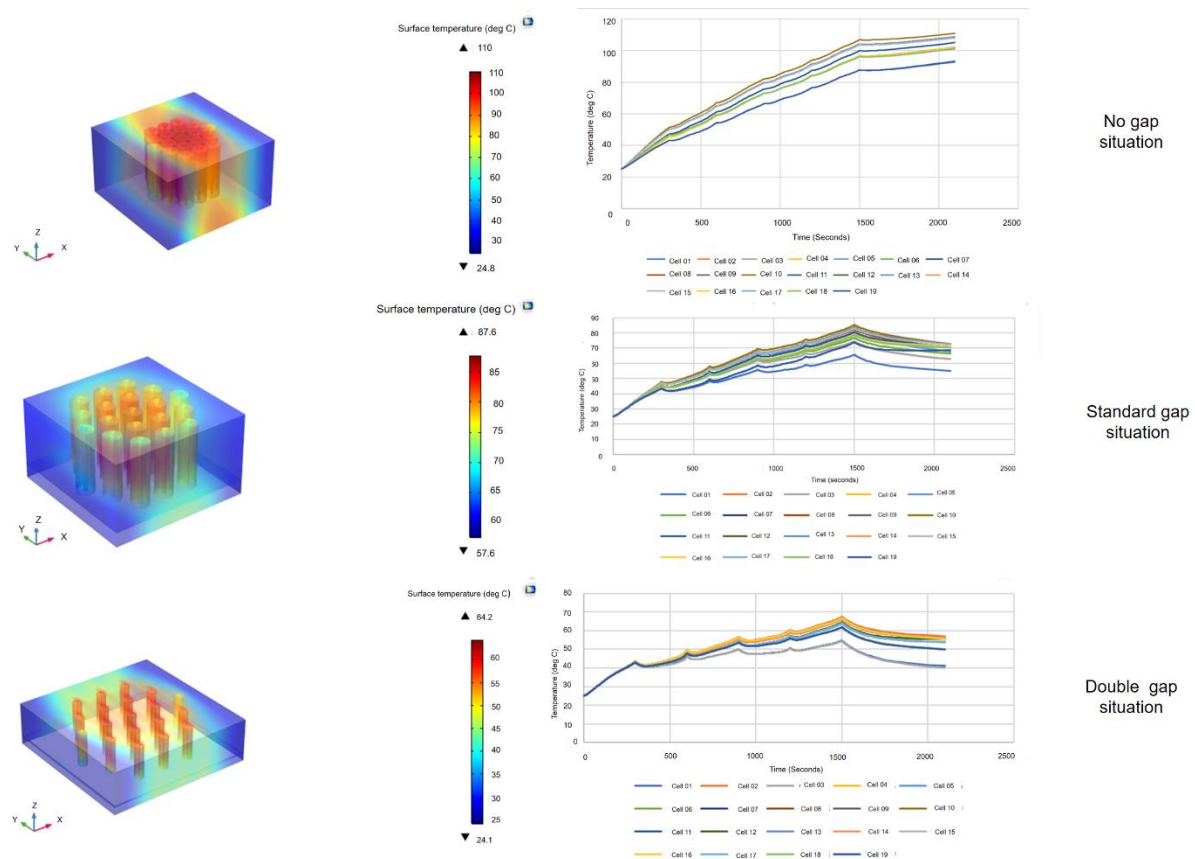
Figure 4.15. Simulation results at 1500 s and 2100 s

The maximum temperature for the no-gap scenario is achieved by both the battery cell and the heating element, as recorded in the centre for both experiments and simulations. The values became 110 °C and 100.9 °C for the simulation and the experiment, respectively. By considering this fact, the common plot of temperature distribution for both the battery cell and the heating element in a no-gap scenario was drawn to the centre element and shown in Figure 4.16.

Experimental validation of heat transfer model for Li-ion battery module using a metallic enclosure
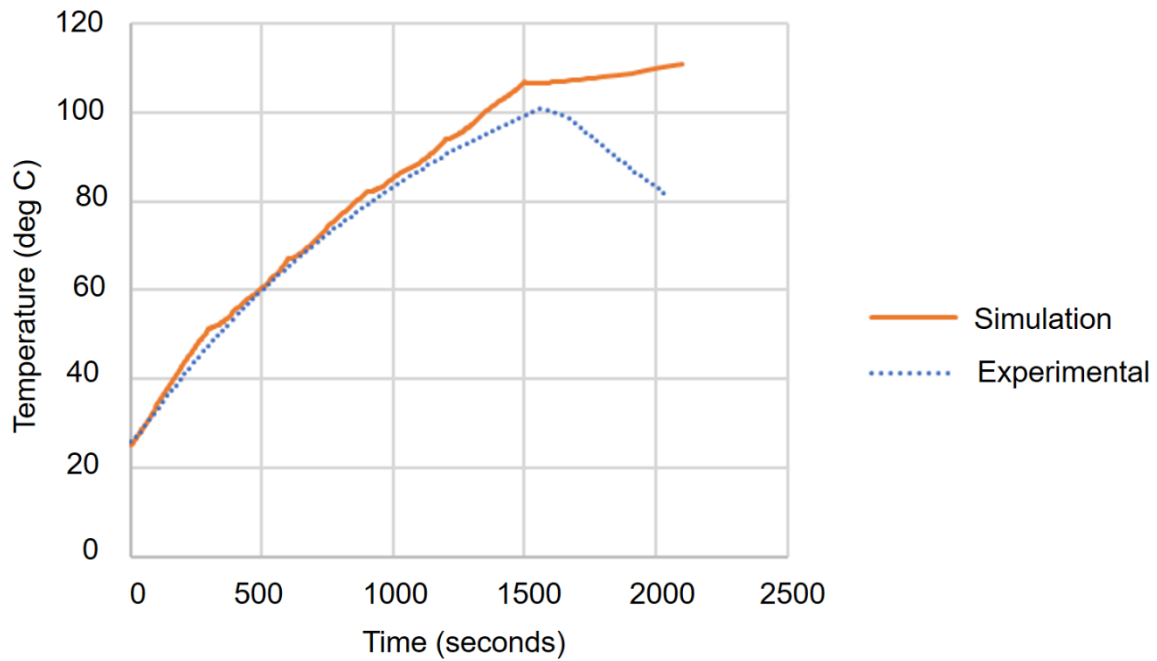
Figure 4.16. Temperature distribution results for both experiment and simulation

To find out whether there is any significant difference between the experimental and simulation results, the one-way ANOVA statistical test was run up to the discharge moment, and the results of ANOVA test can be figured out as follows:

Table 4.9. ANOVA test results

Descriptives								
Temperature °C								
	Number of data	Mean	Std. Deviation	Std. Error	95% Confidence Interval for Mean (CI)		Minimum	Maximum
					Lower Bound	Upper Bound		
Experimental	1611	70.6	21.7	.55	69.6	71.7	25.0	100.9
Simulation	750	70.5	24.5	.99	68.6	72.5	25.0	110.0
Total	2361	70.6	22.5	.48	69.7	71.5	25.0	110.0

Experimental validation of heat transfer model for Li-ion battery module using a metallic enclosure

ANOVA

Temperature °C

	Sum of Squares	Degree of freedom	Mean Square	F	Sig.(p)
Between Groups	6.4	1	6.4	0.013	0.91
Within Groups	1096263.6	2172	504.7		
Total	1096270.0	2173			

There was no significant difference between groups as determined by the one-way ANOVA (F (1,2172) =0.013, p=0.91). Descriptives show that the mean value of temperature (69.7±0.48) was not significantly different between experimental and simulation (p= [0.91], 95% CI = [70.6,70.5]). Therefore, there was no significant difference between experimental and simulation data of the heating element, which is at the center, up to the discharging moment for the no gap scenario.

The maximum temperature for the standard-gap scenario is achieved by both the battery cell and the heating element, as recorded in the centre one for both experiments and simulations. The values became 87.6 °C and 70.2 °C for simulation and the experiment, respectively. By considering this fact, the common plot of temperature distribution for both battery cell and the heating element, at a standard gap scenario was drawn to the centre element, and it is shown in Figure 4.17.
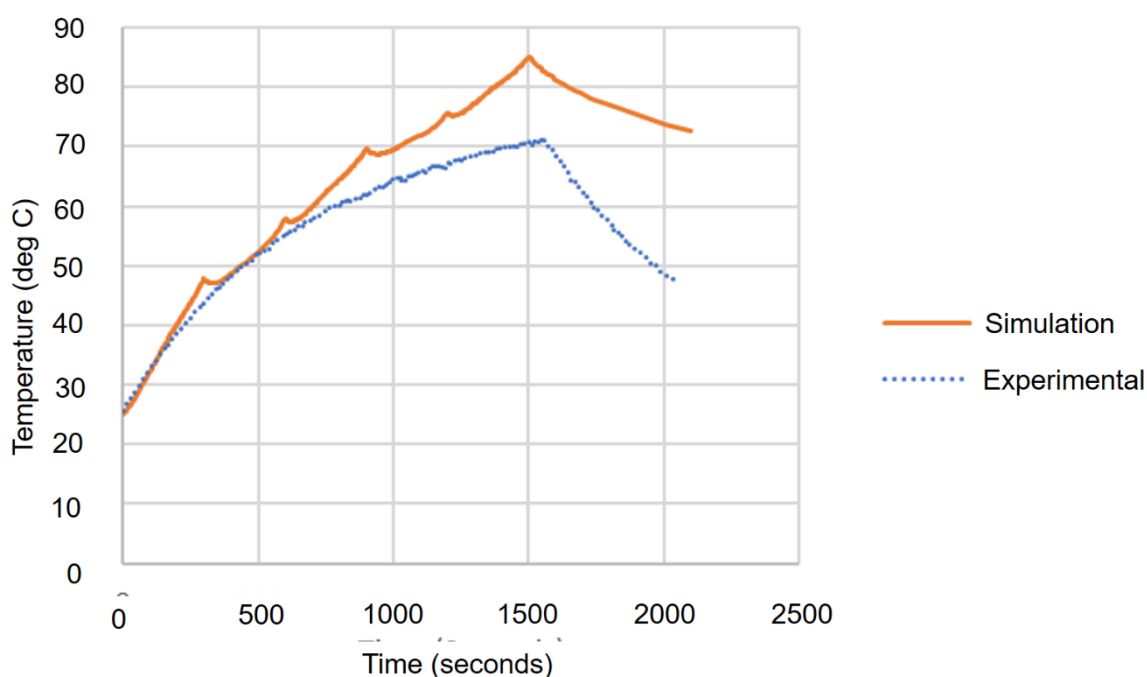
Figure 4.17. Temperature distribution results for both experiment and simulation

Experimental validation of heat transfer model for Li-ion battery module using a metallic enclosure

To find out whether there is any significant difference between experimental and simulation results, the one-way ANOVA statistical test was run up to the discharge moment, and the results of ANOVA test can be figured out as follows:

Table 4.10. ANOVA test results

Descriptives

Temperature°C

	Number of data	Mean	Std. Deviation	Std. Error	95% Confidence Interval for Mean (CI)		Minimum	Maximum
					Lower Bound	Upper Bound		
Experimental	1611	55.7	12.4	.32	55.0	56.3	25.0	70.2
Simulation	750	59.5	17.3	.65	58.2	60.7	25.0	87.6
Total	2361	56.9	14.3	.30	56.3	57.5	25.0	87.6

ANOVA

Temperature °C

	Sum of Squares	Degree of freedom	Mean Square	F	Sig.(p)
Between Groups	7021.0	1	7021.0	35.0	<0.001
Within Groups	444622.3	2217	200.6		
Total	451643.4	2218			

There was a significant difference between groups as determined by one-way ANOVA (F (1,2217) =35.0, p<0.001). Descriptives show that the mean value of temperature (56.9±0.30) was significantly different between experimental and simulation (p= [<0.001], 95% CI = [55.7,59.5]). Therefore, there was a significant difference between experimental and simulation data of the heating element, which is at the centre, up to the discharging moment.

The maximum temperature for the double-gap scenario is achieved by both the battery cell and the heating element, which were recorded in the centre for both experiments and simulations. The values became 64.2 °C and 66.3 °C for simulation and the experiment, respectively. By considering this fact, the common plots of temperature distribution for both the battery cell and the heating element in the double-gap scenario were drawn to the centre element, as shown in Figure 4.18.

Experimental validation of heat transfer model for Li-ion battery module using a metallic enclosure
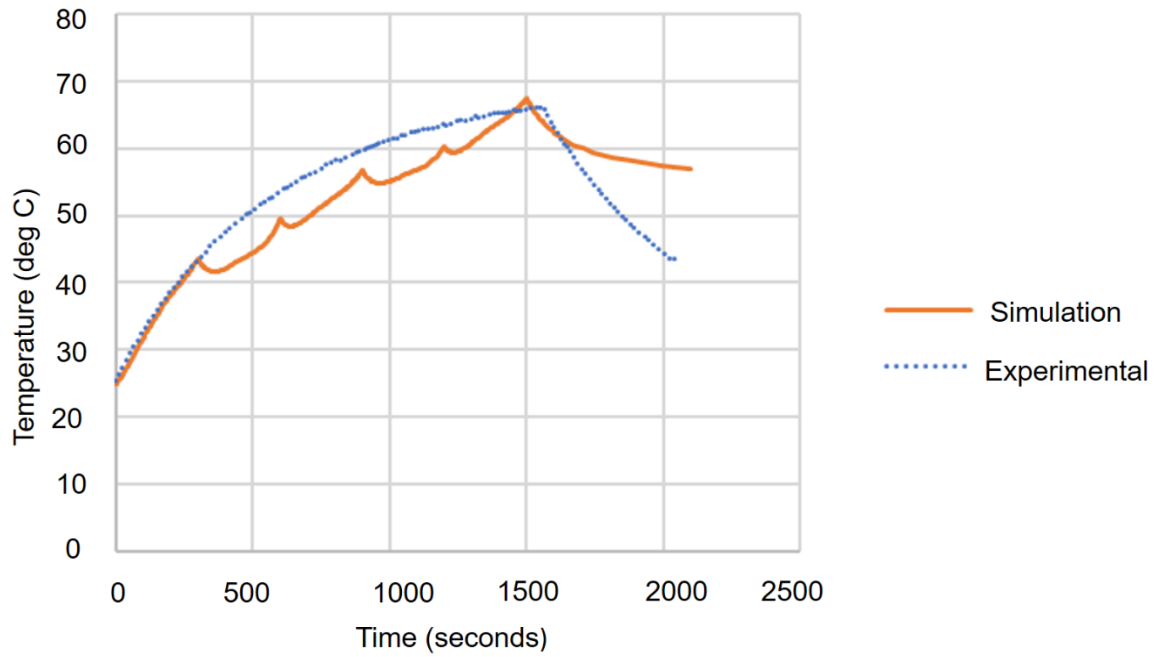
Figure 4.18.Temperature distribution results for both experiment and simulation

To find out whether there is any significant difference between both the experimental and simulation results, the one-way ANOVA statistical test was run up to the discharge moment, and the results of ANOVA test can be figured out as follows.

Table 4.11. ANOVA test results

Descriptives

Temperature°C

| | Number of data | Mean | Std. Deviation | Std. Error | 95% Confidence Interval for Mean (CI) | | Minimum | Maximum |
					Lower Bound	Upper Bound		
Experimental	1611	50.3	11.0	.27	54.9	54.9	25.0	66.3
Simulation	750	54.4	11.8	.43	49.3	51.1	25.0	64.2
Total	2361	53.1	11.4	.23	53.6	53.6	25.0	64.2

Experimental validation of heat transfer model for Li-ion battery module using a metallic enclosure

ANOVA

Temperature ℃

	Sum of Squares	Degree of freedom	Mean Square	F	Sig.(p)
Between Groups	8784.8	1	8784.8	69.9	<0.001
Within Groups	296641.1	2359	125.7		
Total	305425.9	2360			

There was a significant difference between groups as determined by one-way ANOVA (F (1,2359) =69.9, p<0.001). Descriptives show that the mean value of temperature (53.1±0.23) was significantly different between experimental and simulation (p= [<0.001], 95% CI = [50.3,54.4]). Therefore, there was a significant difference between experimental and simulation data of the heating element, which is at the centre, up to the discharging moment.

Considering all the results of the metallic enclosure and without airflow scenario, it can be found that there are some minor differences that exist between both experiments and simulations for the standard-gap scenario and the double-gap scenario. It is because, in the experiment, the environmental conditions are not always constant as in the simulations, and also because there are some unavoidable issues in fixing heating elements (i.e., they are not vertical as in the simulation and are always associated with a small angle), which will cause minor deviations in exposed surfaces. Furthermore, in the simulation, the batteries are associated with the charge-discharge circle, and in experiments, the heating elements show the continuous heating with the continuous power supply. Therefore, to make the heating elements more compatible with the battery cells, the future experiments will be run with a discontinuous power supply.

4.4   Temperature measurement with airflow-metallic enclosure

The experiments were run with a discontinuous power supply to replicate the real battery charge-discharge behaviour, and 300 s of cycle time was considered. The powering cycle was changed mainly due to the slight graphical deviation found between the continuous power supply experimental data and the simulation data .The airflow supply was provided by using 2 PC fans, and the fans provided the 2 m/s of rated airflow velocity to the arrangement. The airflow velocity was chosen by considering the range which is used in the industry [68] for air cooling battery modules and then by considering the available PC fan air velocities. One fan is to supply the air and the other fan is to suction the airflow, and therefore 2 PC fans were used to supply a linear, continuous airflow through the enclosure. The flow velocity is constant

since the fans were programmed to have a 2 m/s velocity. In addition to that, to control the environmental parameters a steel enclosure is also used with the experiments. The steel enclosure consists of a circular inlet and a circular outlet. The diameter of both the inlet and outlet is 20 mm. This diameter was selected based on the values that were considered in previous literature [68]. The experimental arrangement is shown in Figure 4.19.
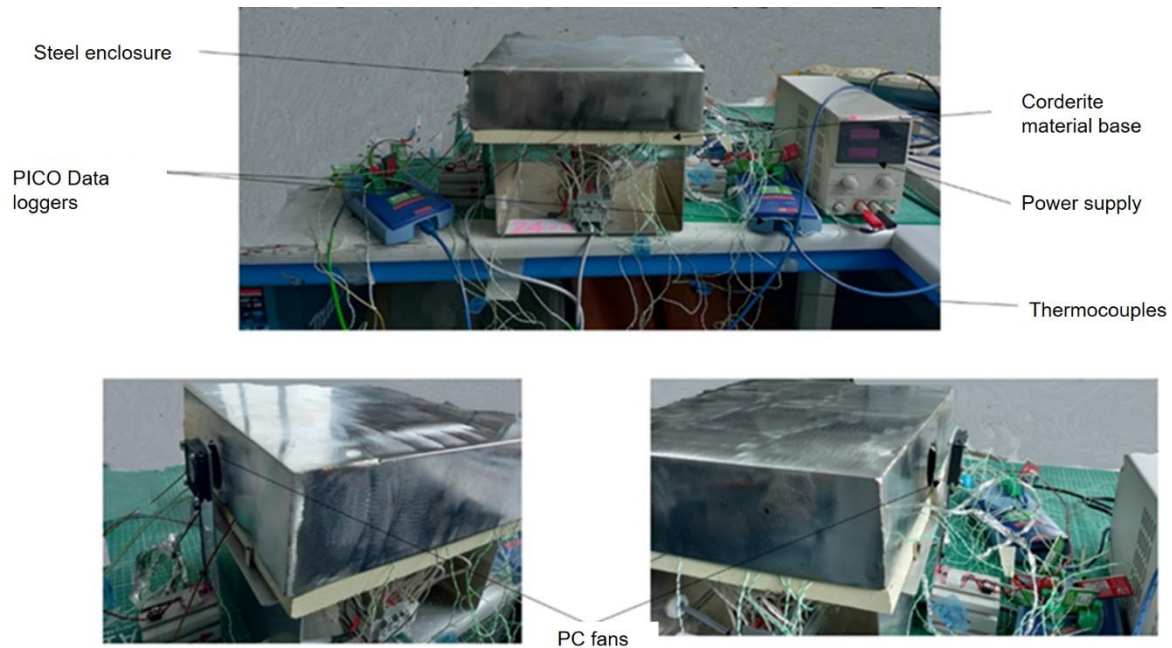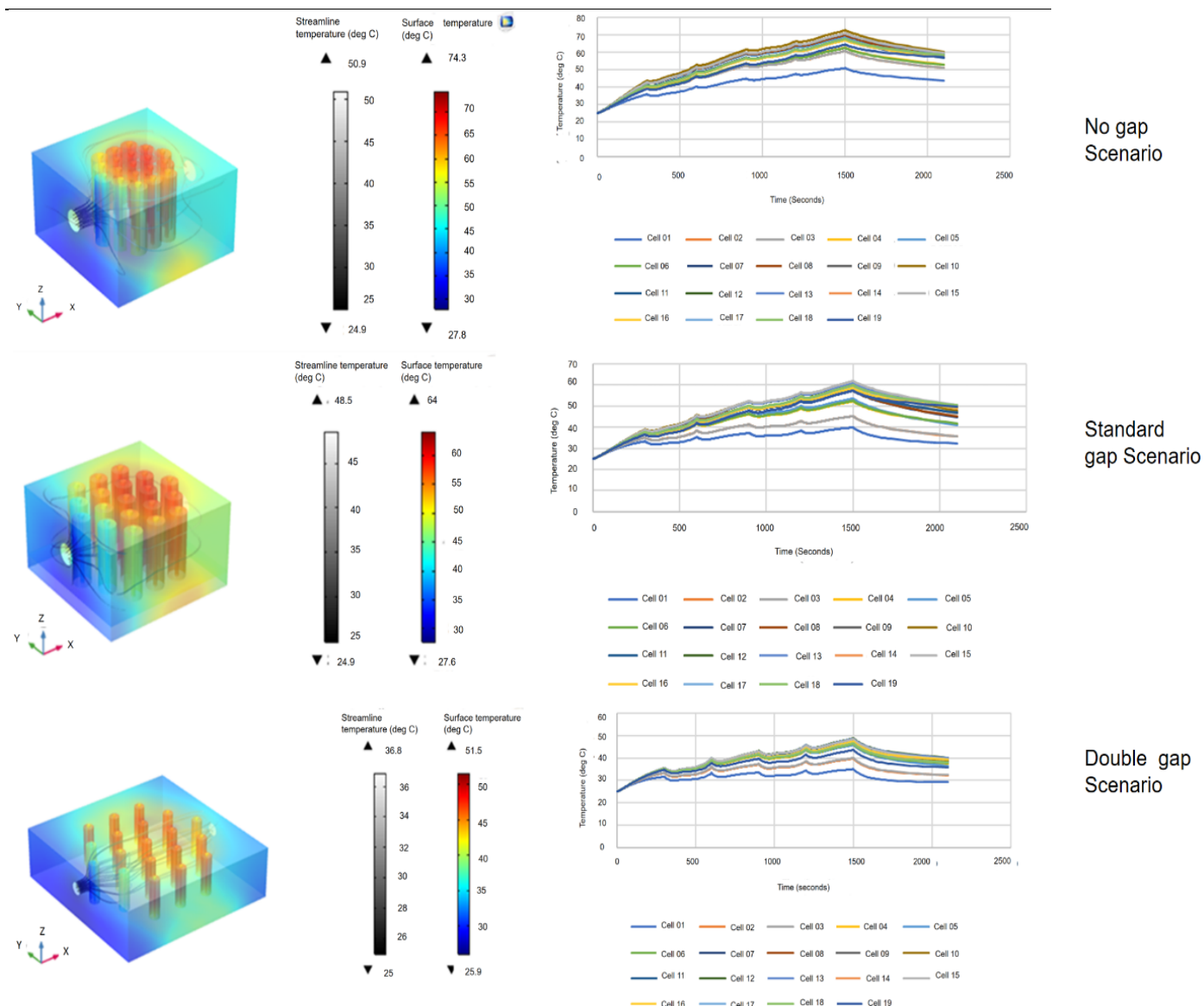

Figure 4.19.Experimental arrangement with the steel enclosure and PC fans

4.5 Effect of inter-cell distance and the comparison between simulation and experimental results

The simulations for the no-gap scenario, standard-gap scenario, and the double- gap scenario was conducted with the airflow conditions. The airflow rate was taken as 2 m/s as indicated in the experiments. However, since there is forced air convection associated with the airflow velocity, 10 W/m^{2}K of heat transfer coefficient is added, and the initial temperature of 25 $^\circ$C is considered. Steel enclosure properties are adopted using the material library from COMSOL. The simulation results for all three scenarios at 1500s and 2100s are shown in Figure 4.20.

Experimental validation of heat transfer model for Li-ion battery module using a metallic enclosure

Figure 4.20.Simulation results for three scenarios with airflow and the steel enclosure

Three experiments were also conducted (with the same repeatability) for each heating element arrangement with the steel enclosure and the airflow, which has 2 m/s velocity as mentioned above. The experimental results for each heating element arrangements' (including no-gap scenario, standard-gap scenario and double-gap scenario) temperatures are shown Annex 5 ,Annex 6 and Annex 7.

The temperature distribution pattern for heating elements in the no-gap scenario is similar to the simulation results as shown in Figure 4.20, and the lowest temperature is at the element that is situated near the inlet. In the simulation, the maximum temperature, that is achieved by the heating element at the inlet is 50.8 °C, but in the experiment it was 37.5 °C. The maximum temperature was achieved at the centre element for both the experiment and simulation. The

maximum temperature that was achieved in the simulation is 72.5 °C, while the value for the experiment is 64.2 °C.

Also, it was considered the heating element, which was situated near the outlet as well. Although it was not the maximum, a considerable amount of temperature difference can be seen in the element in both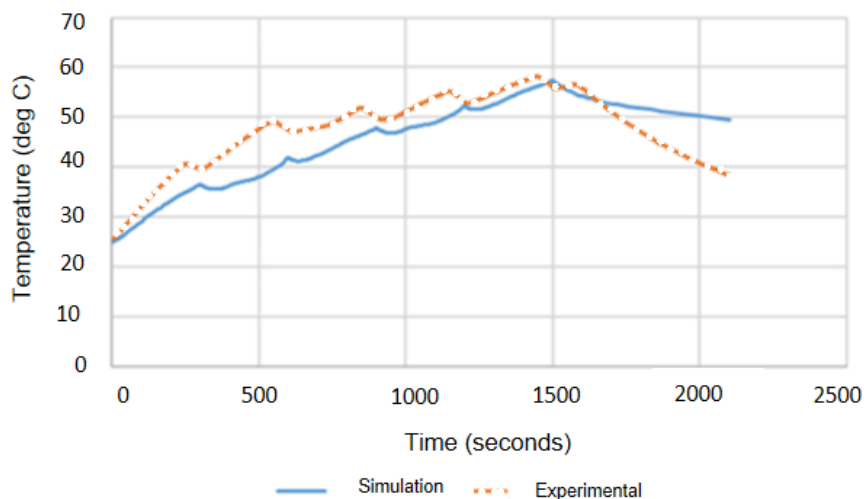 simulation and experiment. The common plots for the specified heating elements for no-gap scenario are shown in Figure 4.21.

Common plots for the heating elements which is near to the inlet

Common plots for the centre heating element

Common plots for the furthest heating element
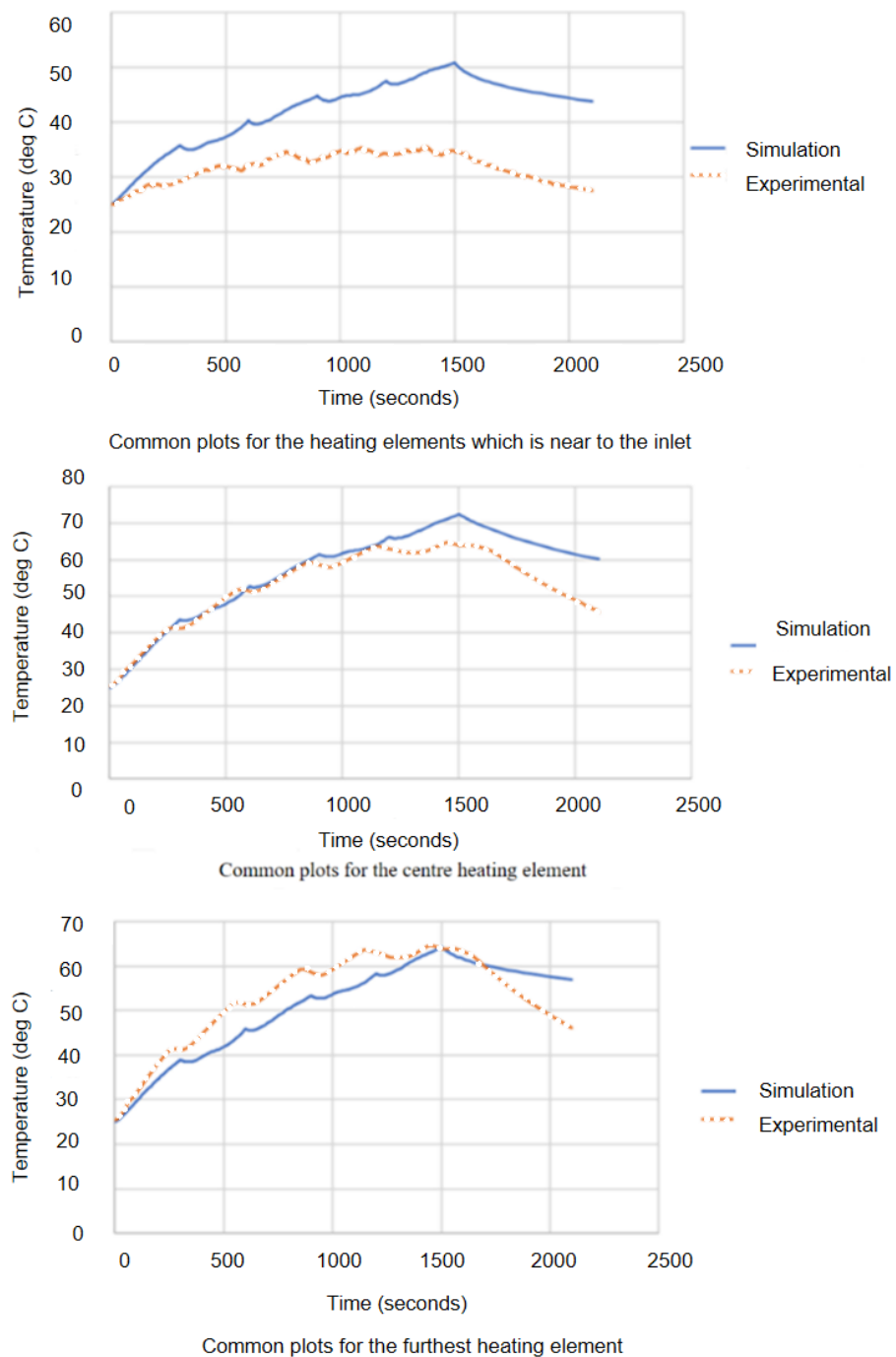
Figure 4.21. Common plots for the heating elements in the no-gap scenario

One-way analysis of variance (ANOVA) statistical tests are run for the data of both simulation and experimental scenarios up to the discharge moment by considering each of the three specified heating elements using SPSS. The results are summarised in Table 4.12.

Table 4.12.ANOVA test results summary

Heating element location	ANOVA conclusion
Near the inlet	Significant difference between experimental and simulation data
Centre	No significant difference between experimental and simulation data of the heating element
Furthest from inlet	Significant difference between experimental and simulation data

The statistical analysis confirms that the simulation is more accurate at the centre of the battery than the inlet and outlet points. This may be caused by existing natural air flow at these points, which is not captured by the simulation. Furthermore, the simulation assumes that air is entering and exiting the battery elements only from the two fan positions. This is not easy to achieve in the experimental setup though the gaps were sealed using tapes.

In the simulation for standard-gap scenario, the maximum temperature that is achieved by the heating element at the inlet is 39.9 $^{\circ}$C, but in the experiment it was 39.7 $^{\circ}$C. As indicated in Figure 4.21, the temperature distribution pattern for heating elements is almost the same as the simulation results, and the lowest temperature is at the element that is situated near the inlet.

Although, the maximum was achieved at the centre element in no-gap situation, here for the standard-gap scenario, the maximum temperature was achieved at the element which was situated next to the centre element for both experiment and simulation. The maximum temperature which was achieved at the experiment is 58.8 $^{\circ}$C and the value for the simulation is 61.9 $^{\circ}$C.

In addition to that, the heating element, which was situated near the outlet, was also considered for the standard-gap scenario. Although it was not the maximum, a considerable amount of temperature distribution can be seen in the element in both simulation and experiment for the standard-gap scenario.

The common plots for the specified heating elements are shown in Figure 4.22.
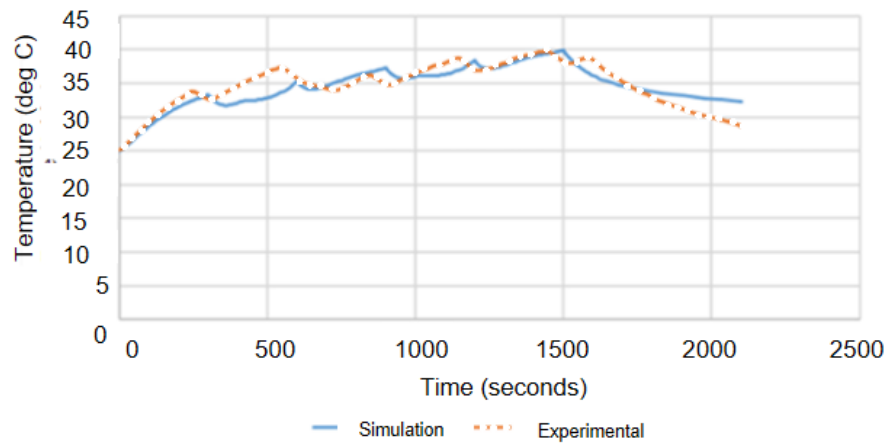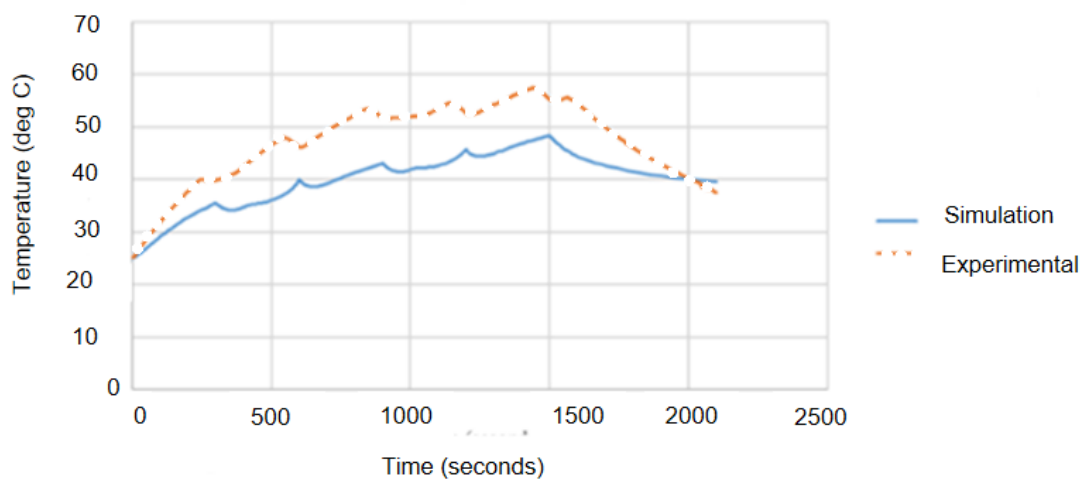

Common plots for the heating element which is near to the inlet
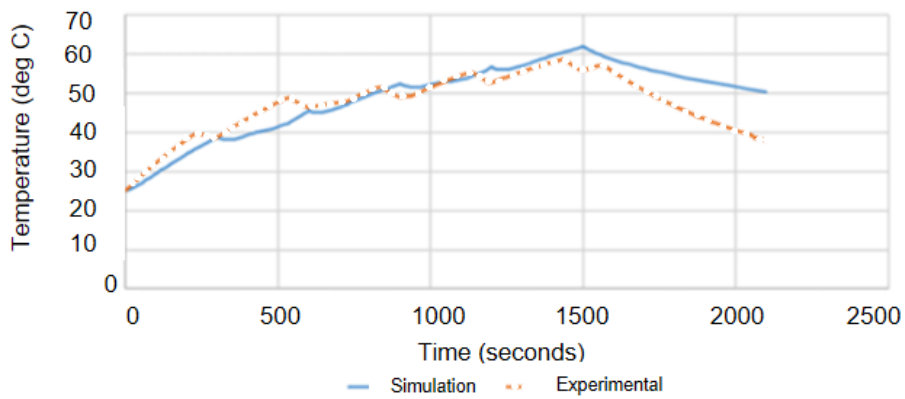
Common plots for the heating element, situated next to the centre element

Common plots for the furthest heating element

Figure 4.22.Common plots for heating elements

Experimental validation of heat transfer model for Li-ion battery module using a metallic enclosure

As in the previous section, statistical analysis was performed for these three cases. The results are summarised in Table 4.13.

Table 4.13. ANOVA test results summary

Heating element location	ANOVA conclusion
Near the inlet	No significant difference between experimental and simulation data
Centre	No significant difference between experimental and simulation data of the heating element
Furthest heating element from the inlet	Significant difference between experimental and simulation data

Although the same issues as before apply to this case (conditions close to the outlet locations of the battery element vary more compared to the inlet and centre of the experimental rig) it can be concluded that there is a good agreement between simulation and experimental results for the standard-gap scenario.

As shown in Figure 4.23, the temperature distribution pattern for heating elements for double-gap scenario is almost the same as the simulation results. The lowest temperature is occurred at the element which is situated near to the inlet. In the simulation, the maximum temperature which is achieved by the heating element at the inlet is 35.0 °C and in the experiment it became 36.5 ℃ for double-gap scenario.

Although the maximum was achieved at the centre element in no-gap situation, for double-gap scenario the maximum temperature was achieved at the elements which was situated next to the centre elements and two elements next to that element for both experiment and simulation. The maximum temperature which was achieved at the experiment is 51.9 °C and the value for the simulation is 48.4 °C.

In addition, the heating element which was situated near to the outlet was considered. Although it was not the maximum, still there was a considerable amount of temperature difference can be seen in the element in both simulation and experiment.

The common plots for each specified heating element are shown in Figure 4.23 and the statistical analysis is summarised in Table 4.14
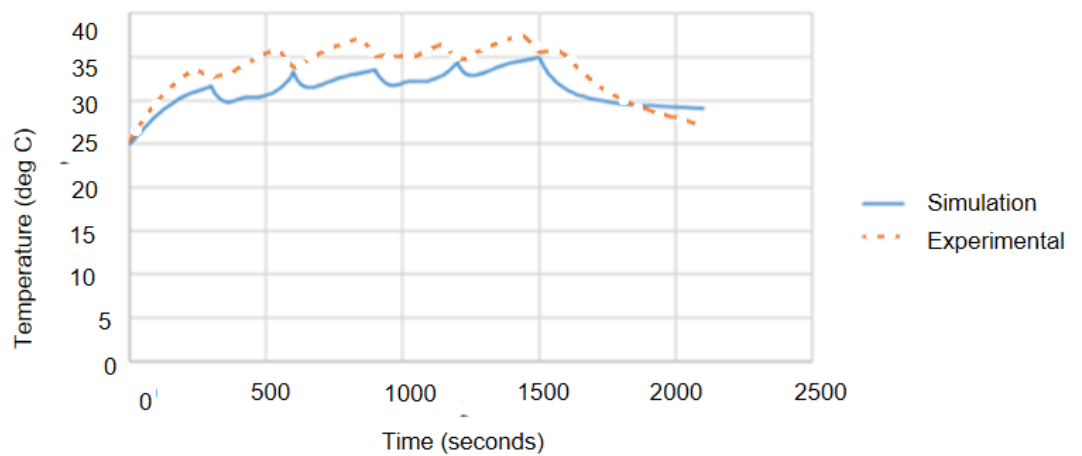
.

Common plots for the heating element which is near to the inlet
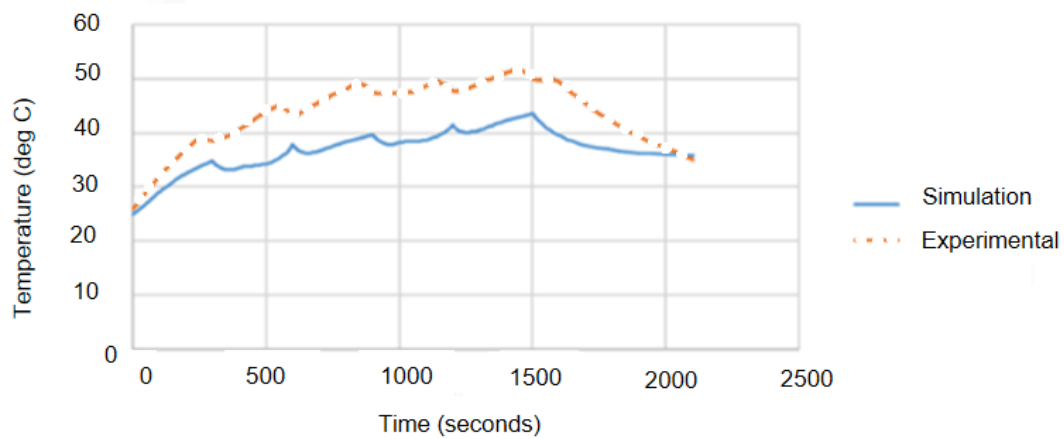
Common plots for the heating element, situated next to the centre element

Common plots for the furthest heating element

Figure 4.23.Common plots for each heating elements

Experimental validation of heat transfer model for Li-ion battery module using a metallic enclosure

Table 4.14. ANOVA test results summary

Heating element location	ANOVA conclusion
Near the inlet	Significant difference between experimental and simulation data
Centre	No significant difference between experimental and simulation data of the heating element
Furthest from heating element	Significant difference between experimental and simulation data

The same trends as in the previous cases are observed (data in the centre of the battery element are closer to simulation results than the inlet and outlet). Also, since the gap is high, a more turbulent air behaviour can be expected inside the module under the natural environment. This may add to the deviations observed in double-gap scenario.

4.6 Discussion and conclusion

By considering the overall results for all scenarios (including without enclosure, with the metallic enclosure, and with the metallic enclosure and airflow supply), there is a good agreement between simulations and experiment results. Minor deviations are attributed to fixing issues of heating elements during the experiments. (Some elements tilt slightly, creating deviations from the ideal geometry of the battery module.). Therefore, it is decided to continue the further investigations and experiments with the existing thermal modelling and the custom jig which is made with the heating elements.

In addition, although there exists a turbulence effect, still there is a considerable reduction of the temperature inside the enclosure can be found with the airflow. However, since the research is more focused on the passive cooling methods than active cooling, the experiments will be continued without the airflow effect.

Also, it was found that, with the discontinuous power supply, the custom jig of heating elements demonstrates much the same behaviour as the battery module. Furthermore, since, the experimental results indicate that the temperature distribution at standard-gap scenario is more uniform and validated with the simulation results, it is decided to continue future experiments on standard-gap scenario with the discontinuous power supply.

5 Composite enclosure for Li-ion battery module

5.1 Composite enclosure design and fabrication

5.1.1 Composite enclosure with no pins

As mentioned in Chapter 2, the Liquid Composite Molding (LCM) method was chosen for the composite enclosure fabrication. Under the LCM method, the composite battery casing was fabricated based on three different methods, including the hand lay-up method, the resin infusion method, and the resin infusion method with a caul plate. Although they are not recommended for large scale manufacturing, three methods were considered to identify the best method for fabricating the final composite enclosure prototype, which is supposed to have variable thermal conductivity.

Though the hand lay-up method is a relatively simple and low-cost technique requiring minimal equipment, it is reducing the final product's quality. Also, parts manufactured using the hand lay-up method may exhibit relatively lower mechanical properties compared to other methods due to potential voids, resin-rich areas, and lower fiber volume fraction. This could lead to reduced stiffness, strength, and fatigue resistance, especially in larger and more critical applications.

Although the resin infusion method generally has longer cycle times compared to hand lay-up and is comparatively expensive, it allows for more controlled resin distribution, minimising voids, and improving mechanical properties. Therefore, parts manufactured using resin infusion can exhibit improved mechanical properties compared to hand lay-up, with better stiffness, strength, and fatigue resistance due to reduced void content and improved fiber consolidation.

In order to enhance compaction during resin infusion, reducing voids, and improving fiber consolidation, the resin infusion with a caul plate was used. However, the use of caul plates adds complexity to the process and requires careful setup and alignment.

As the fibre, Tenax™ woven Carbon fibre from Teijin Carbon Europe is used and as the resin IN2 epoxy infusion resin (EP-IN2-S1) from Easy Composite Ltd is used. As mentioned in the manufacturer's data sheet, the uncured properties of the epoxy resin system are as follows: The resin appears as a clear liquid with a viscosity ranging from 500 to 800 mPa.s. at 20°C, while the hardener, an amber liquid, exhibits a viscosity of 10 to 20 mPa.s. at the same temperature. When combined, the resulting mixture maintains a clear liquid appearance with

a viscosity falling within the range of 200 to 450 mPa.s. The densities of the resin and hardener at 20°C range from 1.08 to 1.18 g/cm³ and 1.07 to 1.13 g/cm³, respectively. The combined formulation yields a density between 1.12 and 1.18 g/cm³.

Regarding pot-life and cure times, the epoxy resin system demonstrates varying characteristics based on temperature and the type of hardener used. At 25°C, the pot-life ranges from 120 to 150 minutes for the slow hardener and 10 to 14 minutes for the fast hardener. Gelation occurs within 8 to 10 hours with the slow hardener and within 2 to 4 hours with the fast hardener, both at 25°C. Demould times, also at 25°C, fall between 18 to 24 hours for the slow hardener and 6 to 8 hours for the fast hardener. Additionally, these times can be adjusted by blending fast and slow hardeners to achieve desired pot-life and demould times within the specified ranges. For accelerated curing, the cure times at higher temperatures are as follows: 24 hours at 25°C, 6 hours at 60°C, and 3 hours at 100°C. Full cure of the epoxy resin system at 25°C typically requires 7 days.

By using a specifically designed mould tool, the enclosures were fabricated. It was designed as a male tool for a 300 mm × 300 mm ×80 mm rectangular composite enclosure and can be seen in Figure 5.1.
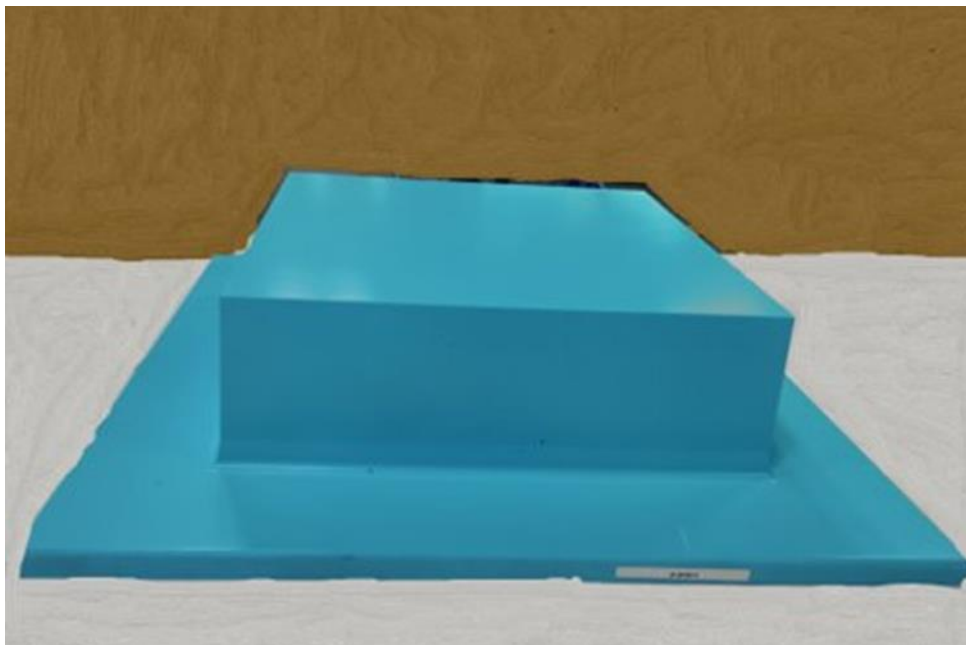
Figure 5.1.Mold tool

Mould tooling was fabricated using a high-density epoxy tooling board, which contains glass microspheres, epoxy resins, and other chemical hardeners. Also, it can withstand 120 °C , and

Marbocote HP7 release agent was used as the release agent for the tooling board since the sealant used for the board was Marbocote HP 2002. For the first manufacturing run, 7 coats were applied for the tooling board, and after that, 4 coats were applied.

Templates for the reinforcement were designed to avoid having ply joints at the corners of the casing. Avoiding ply joints at the corners of the composite enclosure is important because corners tend to experience more stress, and adding joints there can make it weaker. By avoiding joints, the enclosure becomes stronger and less likely to break. It also looks better because there are no visible seams, and it's easier to make during manufacturing. So, by keeping the corners free of joints, it is ensured that the enclosure is strong, looks good, and is easier to make.

The template wrapped around the tooling board can be seen as in Figure 5.2.

Template for fibre
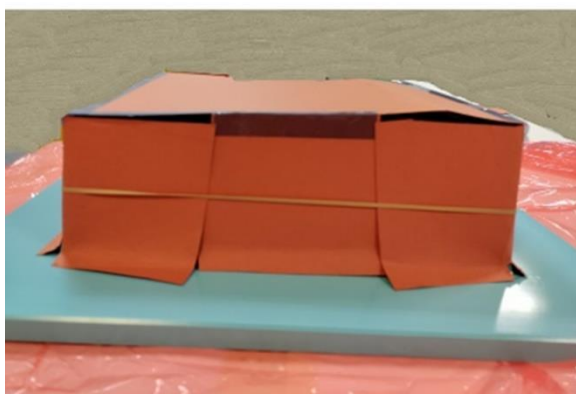
Template assembly with the mould tool

Template assembly with the mould tool

Figure 5.2. Template for fibre and template wrapped with the mould tool

With the 50% of fibre volume fraction, the required quantity for resin is calculated as follows.

$$t = \frac{nA_v}{\rho_f v_f}$$ (28)

where,

t	Thickness of plies		
n	Number of plies	:	8
A_v	Ariel weight (dry fibre)	:	204 g/m^2
ρ_f	Fibre density	:	1.8×10^6 g/m^3
v_f	Volume fraction	:	50%

By substituting the data to Equation (28), the thickness of plies is found as 1.84 mm.

Volume of 5 sides (including top surface and 4 side surfaces)

=30×30×1.84×0.1   =165.6 cm^3

= 30×8×1.84×0.1   =176.6 cm^3

=165.6+ 176.6 cm^3 =342.2 cm^3

Since the fibre volume fraction is 0.5, the resin volume is from total volume is 50% and it is equal to 171.1 cm^3.

It is proposed to have 90% extra resin for the purpose of compensation losses and therefore, the required volume of resin is 171.1cm^3×1.9 = 325.1 cm^3

From the material data sheet of IN2 infusion epoxy resin [55], it was found that the average resin density is 1.10 g/cm^3.

Therefore, the required resin weight is = 325.1 cm^3×1.1 g/cm^3 = 357.6 g

Furthermore, it has mentioned [77] that the mixing ratio of AT30 slow hardener and the resin is 30 :100 and therefore, the relevant weight for hardener is equal to 357.6 g ×0.3= 107.3 g

Both resin and hardener were weighted by using a DYMO digital scale which has the resolution 2g. The mixing process of resin and hardener occurred inside a fume cupboard to ensure safety from fumes. After mixing, the mixture was transferred to a degassing chamber where it underwent degassing to remove any trapped air bubbles. This step is crucial as it helps improve the quality of the composite by reducing voids and enhancing the mechanical properties of the final product.

As mentioned, initially, three methods were followed to fabricate the composite enclosures and first enclosure was fabricated using the hand lay-up method. In hand lay-up method, fibres were placed by manually, and the resin was applied using a brush by hand. However, at the end, it was kept under vacuum for removing tapped air and the better bonding between resin and fibre. The relevant experimental arrangement is shown in Figure 5.3.
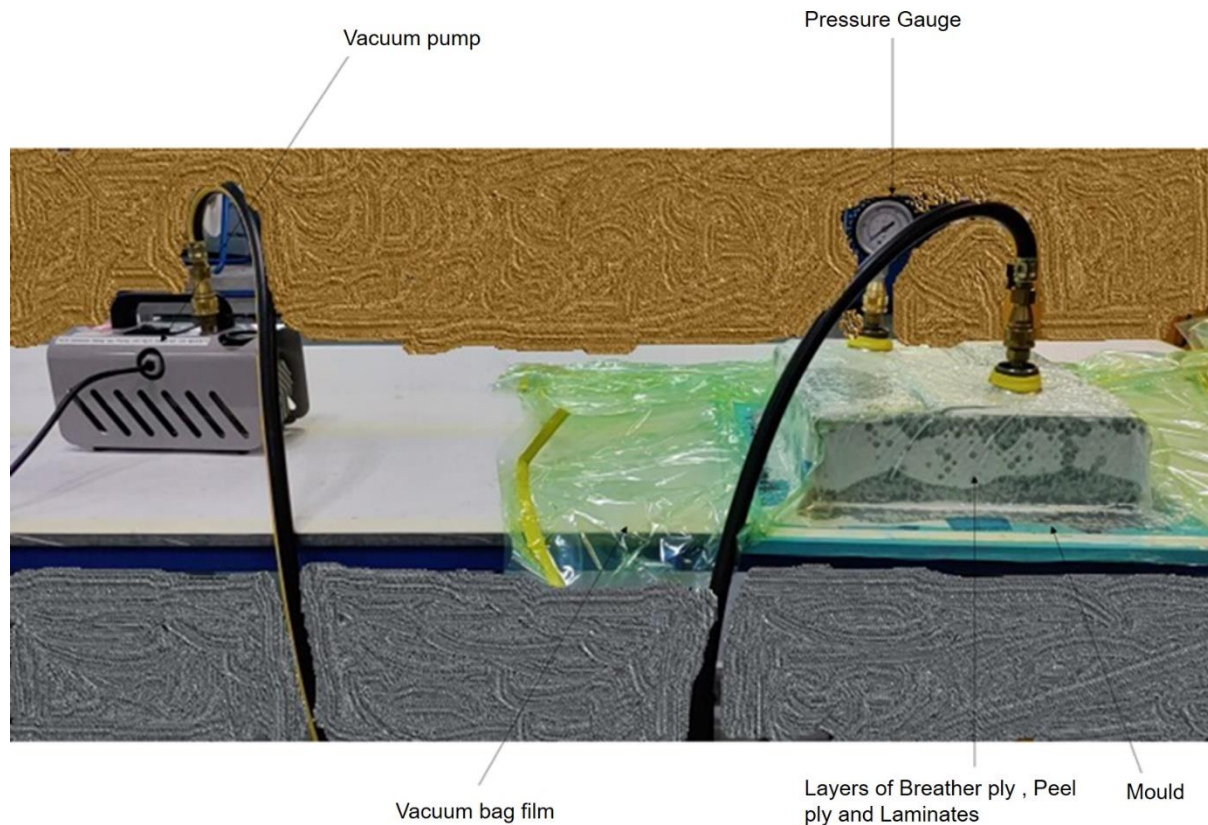
Figure 5.3.Hand lay-up method assembly

The resin infusion method was conducted with the assistance of peel ply, release film, breather ply, mesh, and a vacuum. It is because, in the resin infusion process, the vacuum bag assembly layout is crucial. First, a peel ply goes directly on the mold to create a smooth surface. Then, a release film prevents resin from sticking. Next, a breather material allows air and excess resin to escape. On top of that, a resin distribution mesh ensures even resin flow. Finally, the vacuum bag seals everything tightly, allowing the vacuum pump to remove air and excess resin, leading to high-quality composite parts.

The vacuum was provided by using a vacuum bag and a vacuum pump. The experimental arrangement for resin infusion can be shown in Figure 5.4.
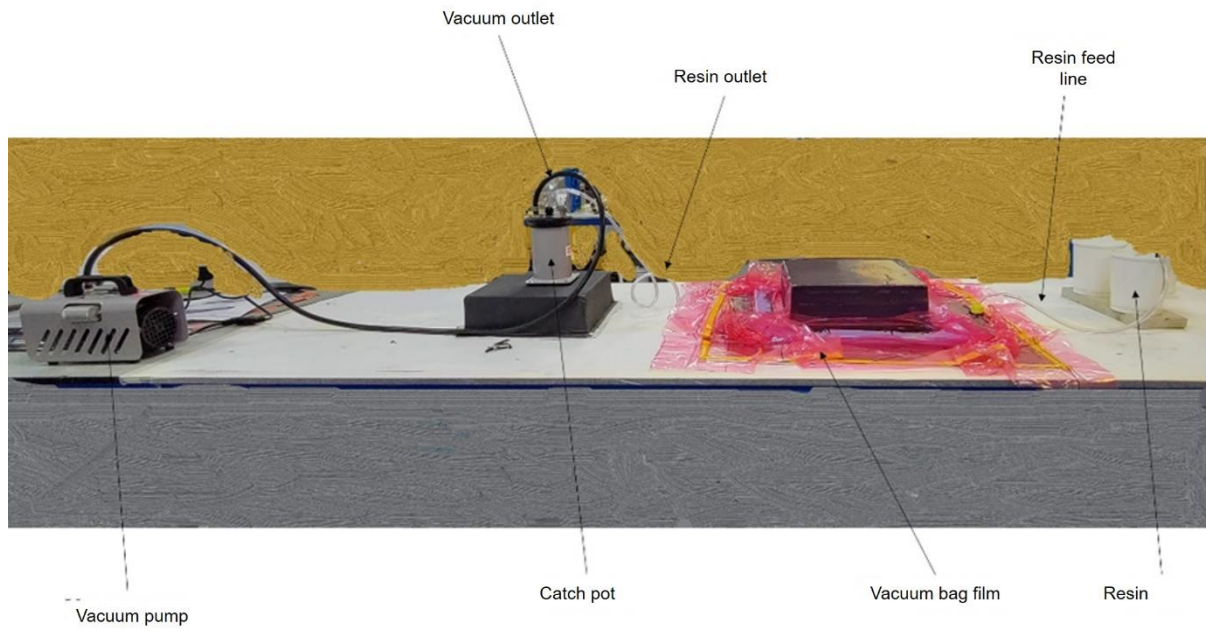
Figure 5.4.Experimental arrangement for resin infusion

The third trial enclosure was fabricated through resin infusion and the caul plate. The caul plate was made of stainless steel and was proposed for a better surface finish. The experimental arrangement is shown in Figure 5.5.
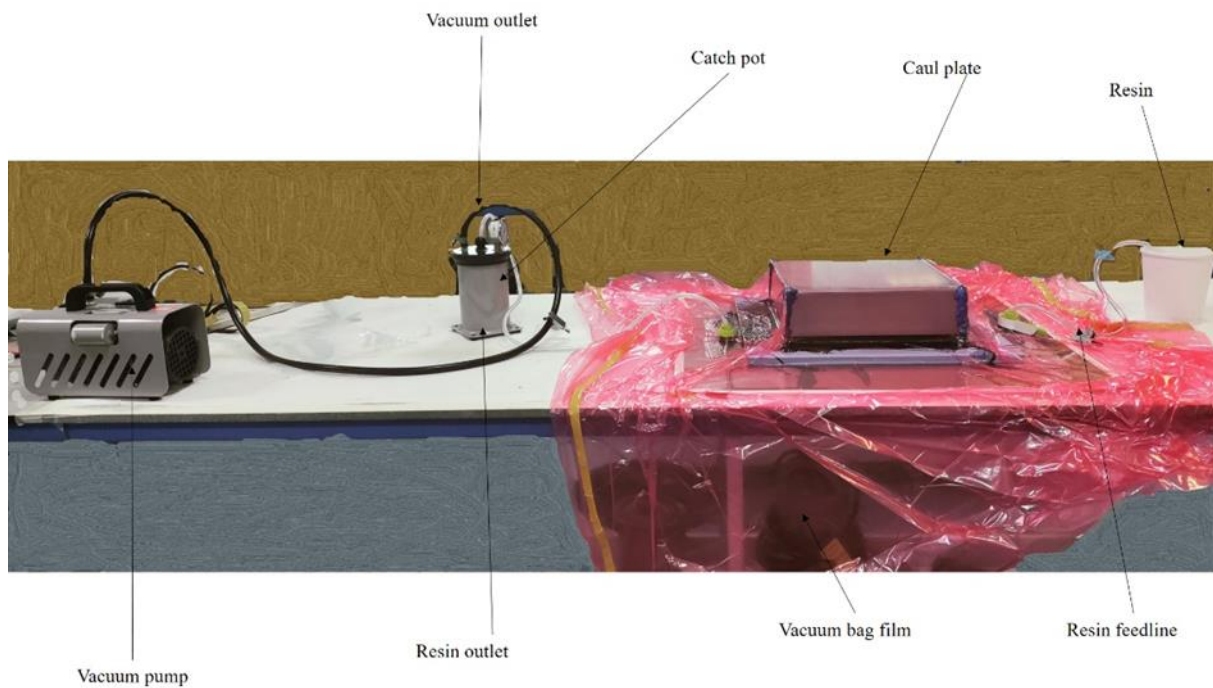
Figure 5.5.Experimental arrangement for resin infusion with caul plate

Enclosure 01- Hand lay-up method

Enclosure 02- Resin infusion method

Enclosure 03- Resin infusion method with caul plate
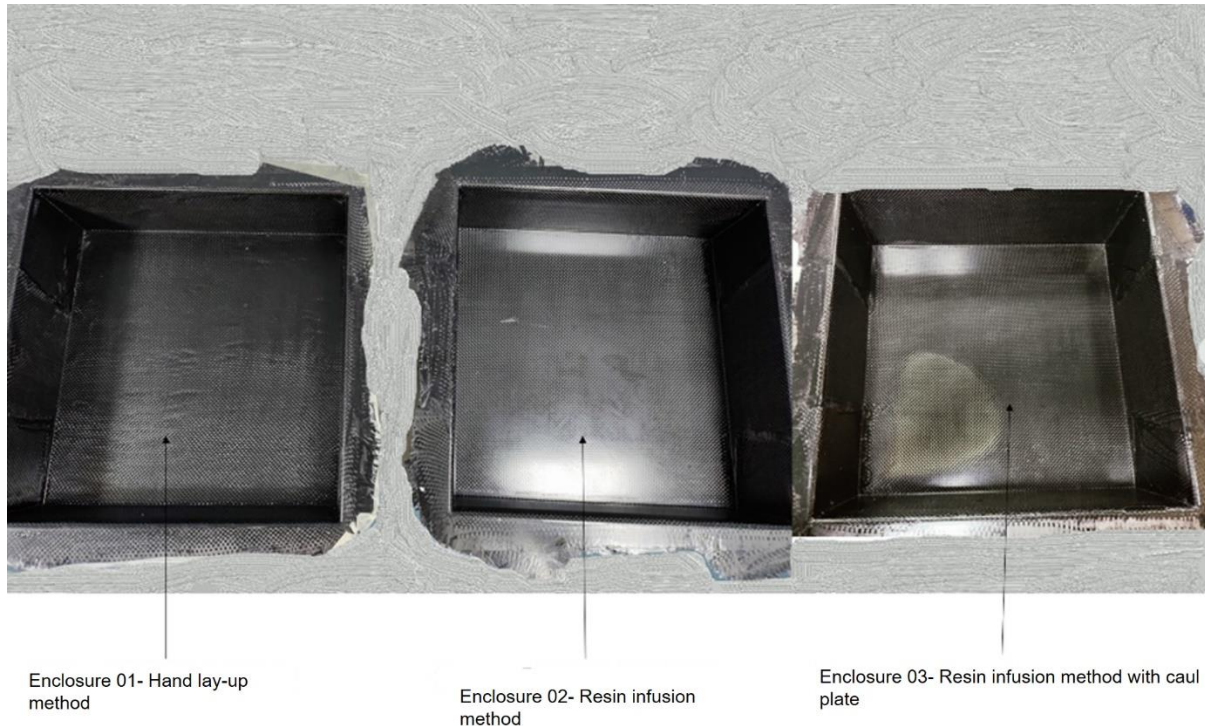
Figure 5.6.First three trail composite enclosures

As indicated in Figure 5.6, the enclosure, which was fabricated using the resin infusion method with caul plate, got a dry spot at the end of process due to air trapping under the caul plate. Therefore, it was decided not to continue the resin infusion with caul plate for enclosure fabrication. However, it was found that the resin infusion method gave a better surface finish than the hand lay-up method. Therefore, resin infusion method is used to fabricate the remaining composite enclosures. To have repeatability in the experiments and the experimental data, three enclosures were fabricated using the resin infusion method. Initially, the enclosures were made without any pins.

5.1.2 Composite enclosure with pins

At the end of fabricating three composite enclosures, it is proposed to produce three additional enclosures which has the thickness of 3.6 mm. These additional enclosures will incorporate metallic pins at significant locations affected by higher temperatures, aiming to improve thermal conductivity. Copper pins were used because copper is identified as the common metal with the highest thermal conductivity [78], and the copper thermal conductivity is 398 W/mK [78]. The metallic pins act as a thermal bridge between the air inside the enclosure and the air outside the enclosure.

5.1.2.1 Identifying significant areas

The experiments were conducted to identify the significant areas where the higher temperatures are marked using both steel enclosure and composite enclosures. Initially, the experiments were conducted to identify the temperature variation of the steel enclosure which has the thickness of 3.5 mm. To identify the temperature of the surface and the temperature variation of the enclosure surface, five orientations were considered in terms of both inside and outside surface, and the experimental configuration can be figured out as follows:
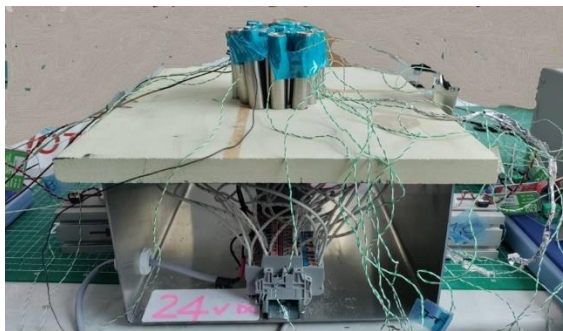
Temperature measurements
of the cells

Temperature measurements
of the enclosure

Figure 5.7.Experimental orientation

Inside the enclosure, the 19 heating elements hexagonal structure, which has the standard gap was operated with the power discontinuity at every 5 min in order to replicate the batteries charge discharge behaviour. The enclosures were heated up for 60 min duration with each orientation for three times. The orientations can be figured out as follows. Here, thermocouple orientation refers to the positions at which the thermocouples are fixed on the enclosure surface.
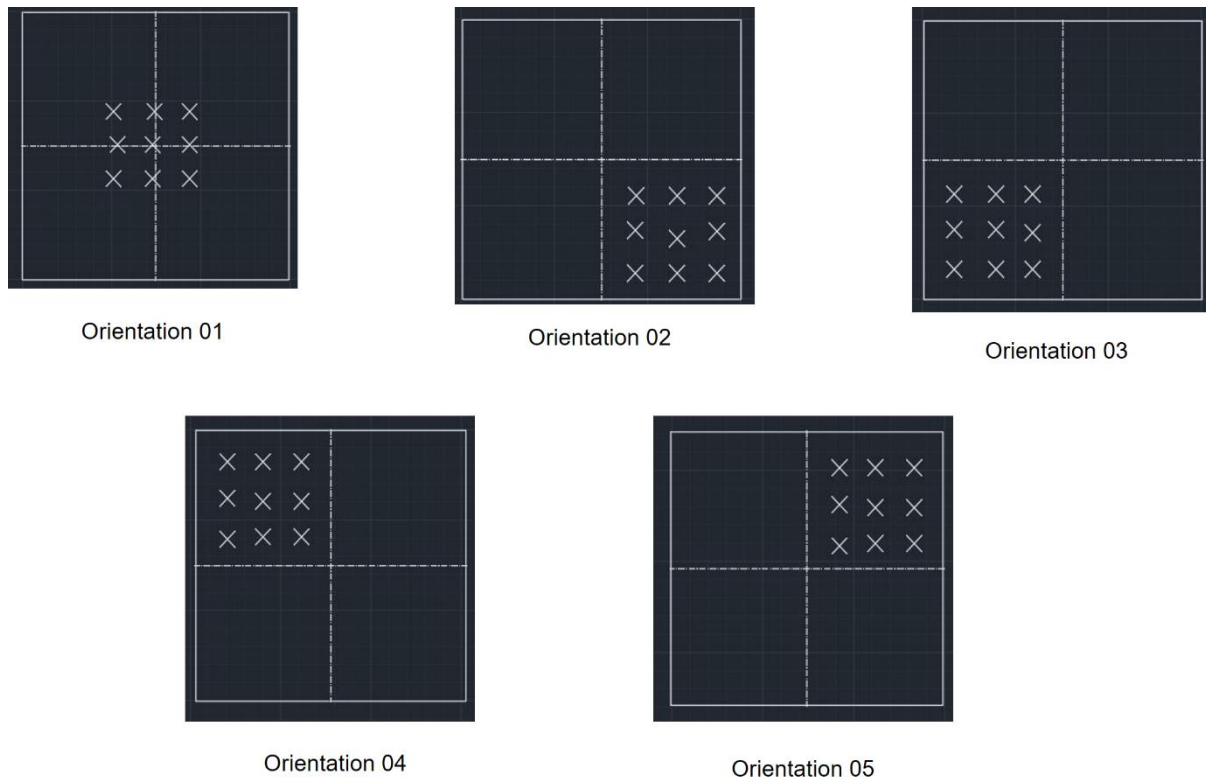
Figure 5.8 Thermocouple orientations

The results for five configurations can be described as follows. (For the temperature plots please refer Annex 8.

For the orientation 1 (inside surface) The average maximum temperature was marked at the centre point, and it was approximately 45 °C. However, according to the results, all nine points have the average maximum temperature above 40 °C.

For the orientation 01 -outside surface the average maximum temperature was marked at the centre point, and it was approximately 40 °C. However, according to results, all nine points have the average maximum temperature above 35 °C and results are mainly varying between 35 °C -40 °C.

For the orientation 2-inside surface the average maximum temperature was marked at the corner point, near to the edge and it was approximately 45 °C. However, according to the results, the temperature on the right side is much higher than on the left side of the orientation. The temperatures are varying between 35-45 °C.

For the orientation 2 -outside surface the results indicate that all nine points have an average maximum temperature approximately 35 °C, and mainly the outside temperature is varying between 35 °C -40 °C.

For the orientation 3 -inside surface the average maximum temperature was marked at the corner point at the right side of the orientation near to the center, and it was approximately 48 °C. However, the overall results indicate that the temperature on the right side is much higher than on the left side of the orientation. Mainly the temperatures are varying between 35-50 °C.

For the orientation 3 -outside surface the average maximum temperature was marked at the same point as in the inside, and it was approximately 38 °C. However, the results indicate that the temperature on the right side is much higher than on the left side of the orientation. The temperatures are varying between 30-40 °C.

For the orientation 4-inside surface the average maximum temperature was marked at the points which are near to the centre and it was approximately 43 °C. However, the results indicate that the temperature on the right side is much higher than on the left side of the orientation. The temperatures are varying between 35-45 °C.

For the orientation 4- outside surface, the average maximum temperature was marked at the points which are near to the centre as in inside, and it was approximately 38 °C. However, the results indicate that the temperature on the right side is much higher than on the left side of the orientation. The temperatures are varying between 30-40 °C.

For the orientation 5- both inside and outside surfaces, the average maximum temperature was marked at the points which are near to the centre, and it was approximately 38 °C. However, the results indicate that the temperature on the right side is much higher than on the left side of the orientation. The temperatures are varying between 35-40 °C.

Therefore, considering the experimental results, it was identified that the heat is mostly associated with the centre part of the enclosure, and therefore, it is suggested to use copper pins at the centre area of the enclosure.

5.1.2.2 Modelling the length of metallic pins and the quantity

Initially, a model for a material plate with a copper pin was built by assuming isotropic material properties. Isotropic materials can be considered as the materials which has no change of the thermal conductivity with the direction. The internal temperature was taken as 65 °C, and the external temperature was set for 0 °C. A considerable level of temperature gap was maintained to observe the temperature variation clearly though the actual temperature values were already available from previous experiments. The convection heat transfer coefficient for both the internal and external sides of the material plate was taken as 10 W/m²K. The thermal conductivity of the material was set at 0.1 W/mK, and the thermal conductivity for copper pin was considered as 398 W/mK. As shown in Figure 5.9, the pin was located at the centre of the material plate through the thickness of 3.5 mm.
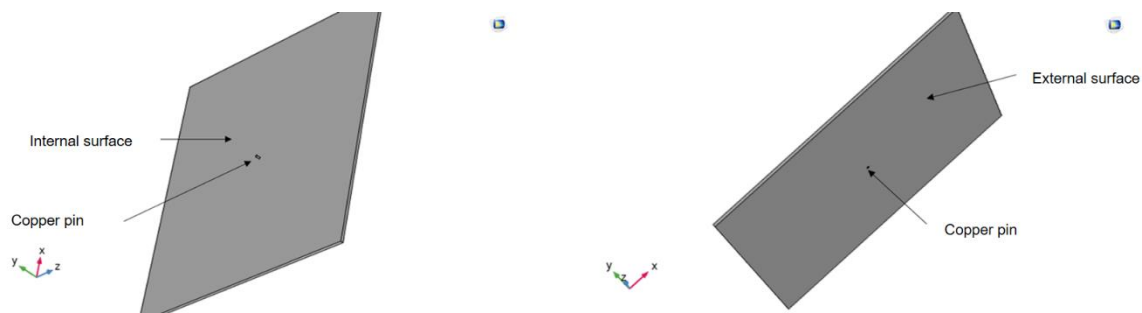
Figure 5.9. Geometry for the simulation

The relevant simulation results at 1500 s can be seen in Figure 5.10 and the results confirmed that the heat is more accumulated at the pin when compared to the other areas of the material plate.
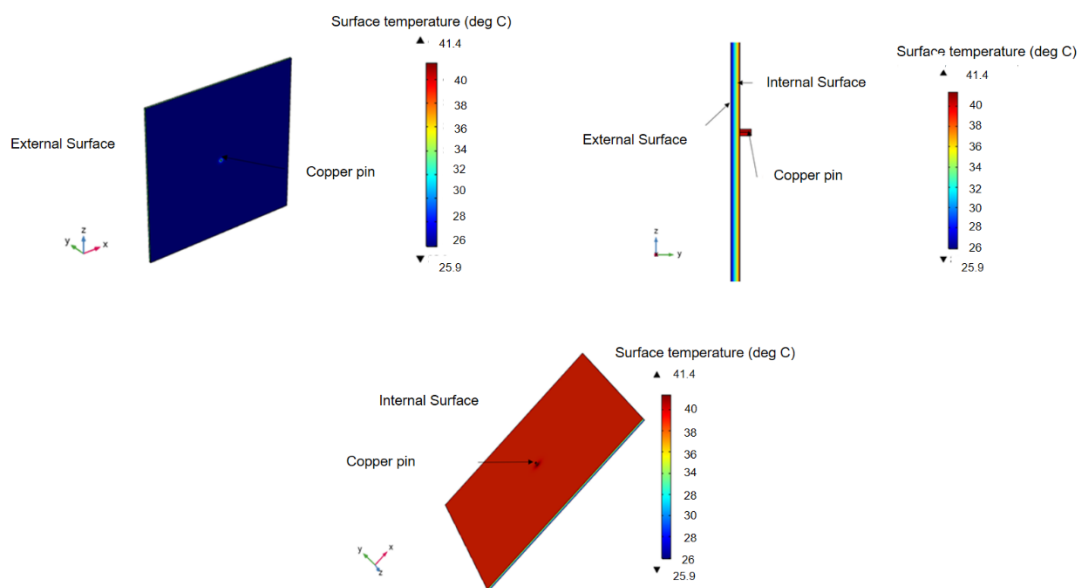
Figure 5.10.Simulation results at 1500 s

In addition to that, it was compared the material plate without a pin and with a pin and the simulation results indicate that the material plate which has the pin shows the higher temperature at the centre (i.e. 41.4 ℃). It is because that the heat is accumulating more prominently towards the pin.

Without pin   With pin
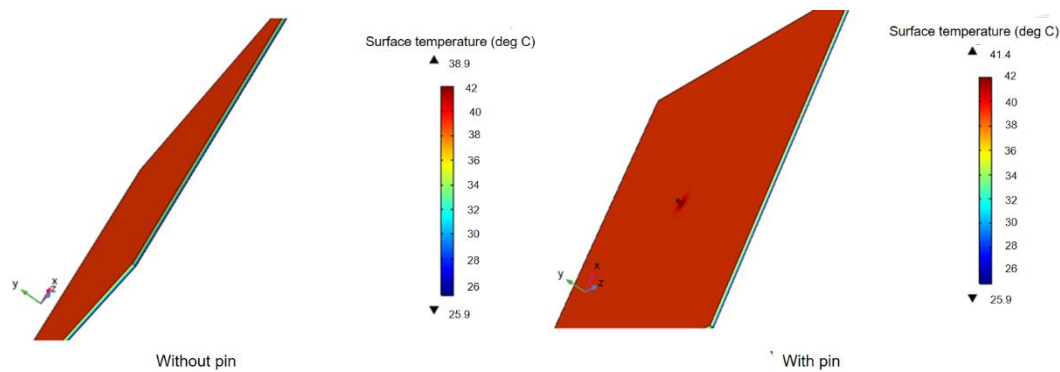
Figure 5.11.Comparison of simulation results for isotropic material without a pin and with a pin

However, since a composite material is an anisotropic material, the anisotropic material properties for thermal conductivity of CFRP were adopted to the existing model (i.e. k_{11} =0.68 W/mK; k_{22}= 0.68 W/mK; k_{33}=4.18 W/mK) [28] and all boundary conditions were kept as the previous (i.e. heat transfer coefficient 5 W/m^{2}K, initial temperature 25℃) The simulation was conducted by considering the time dependent transient approach.

The thermal conductivity of a material can vary depending on the direction of heat flow relative to the structure of the material. In the case of CFRP (carbon fiber reinforced plastic), which is a composite material consisting of carbon fibres embedded in a plastic matrix, the arrangement of fibres greatly influences its thermal conductivity.

The "k11," "k22," and "k33," are referring to the thermal conductivities along different axes. In this context, "k11" and "k22" represent the thermal conductivities in the directions parallel to the layers of carbon fibres, while "k33" represents the conductivity across the layers.

Now, in CFRP, the carbon fibres provide high thermal conductivity along their length (in the directions parallel to the fibres), while the plastic matrix typically has lower thermal conductivity. This means that heat can flow more easily along the fibres (parallel to the layers) than across them.

The significantly higher value of "k33" compared to "k11" and "k22" can be attributed to the fact that heat transfer across the layers of fibres (in the direction perpendicular to the layers)

is less hindered compared to heat transfer parallel to the layers. Even though there are fewer fibres in the third direction, the pathways for heat transfer across the layers are less obstructed by the resin matrix, resulting in a higher effective thermal conductivity in that direction.

The comparison of results without a pin scenario and with a pin scenario for anisotropic material (Figure 5.12) also shows the same behaviour as in the isotropic material, confirming that the pin has the ability to accumulate the most of heat from the material plate. The highest temperature is recorded as 34.2 ℃.
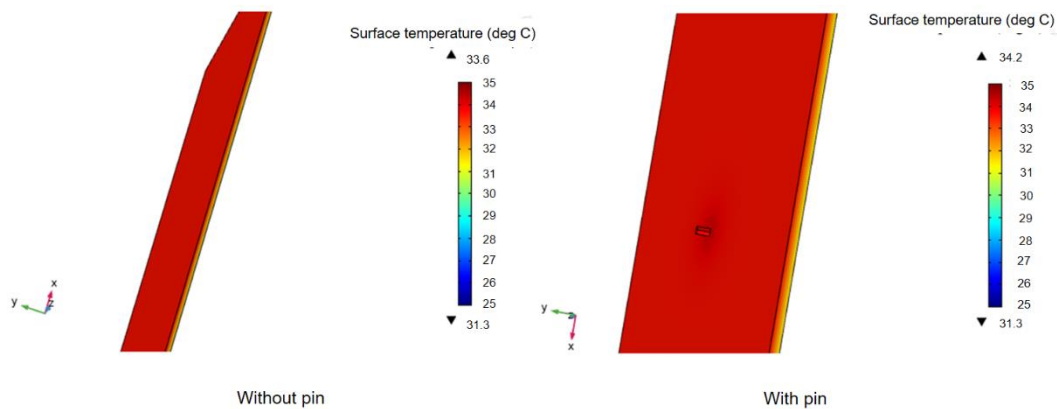
Figure 5.12. Comparison of simulation results for anisotropic material (composite material) without a pin and with a pin

Furthermore, the temperature changing behaviour was analysed for no pin, a pin, and 81 pins in the CFRP material plate and the results are indicated as follows.
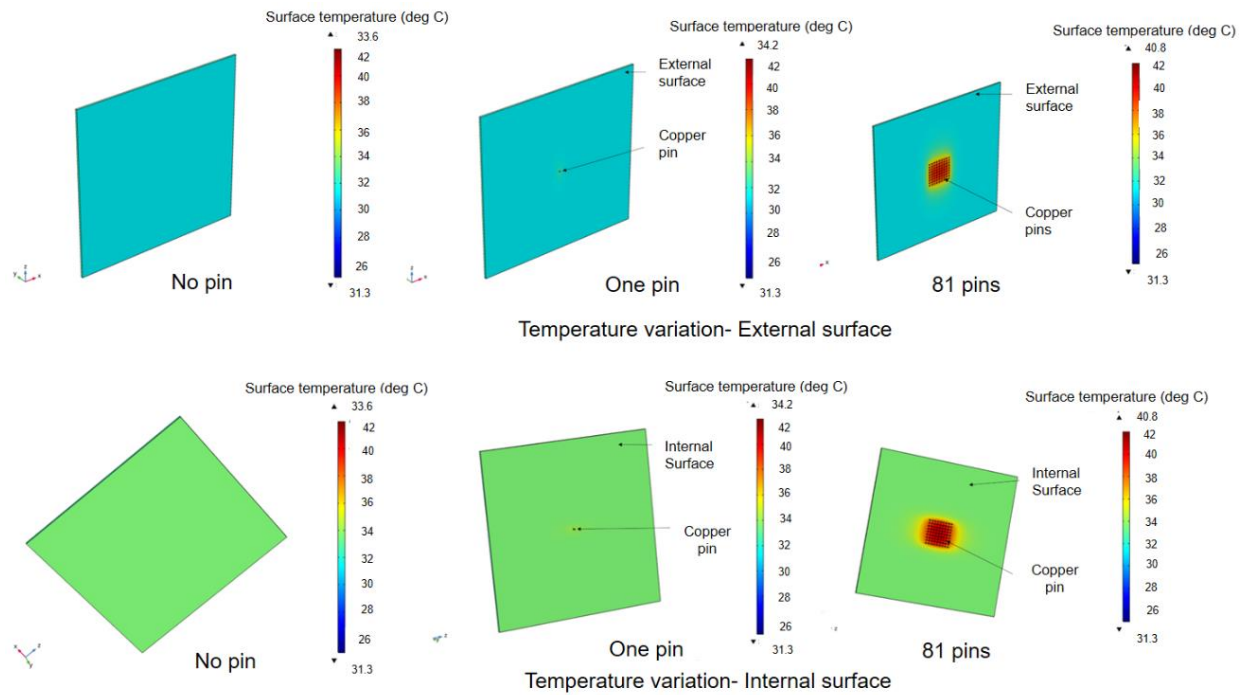
Figure 5.13. Temperature variation of internal and external surfaces with the number of pins
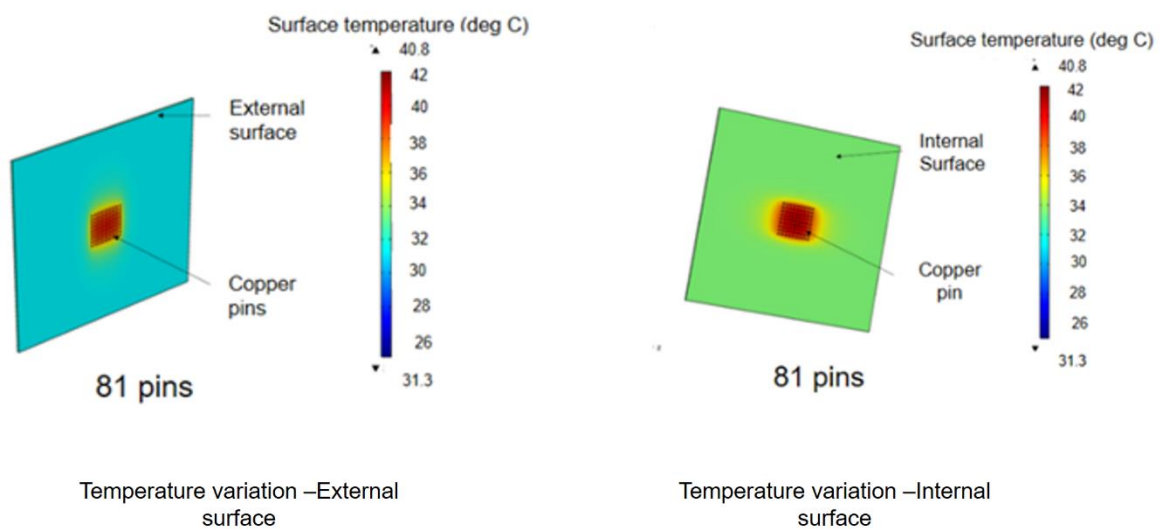
Figure 5.14 Temperature variation of internal and external surfaces for 81 pins

As shown in Figure 5.13 and Figure 5.14, the maximum temperature is increasing along with the number of pins, and it can be seen that, when there are 81 pins, the heat accumulation is comparatively higher than the one pin or no pin. By considering all these simulation results, it can be concluded that the use of copper pins in a composite material can act as a thermal bridge for heat transferring purpose.

As the next step, the pin model was adopted to the battery enclosure to find out the number of pins that is required and the length of pins which are required to maximise the heat transfer through thermal conductivity to have increased surface area.

In the simulation, the same thermal conductivity properties and convection heat transfer coefficients are applied as in previous simulations. However, the external temperature was changed to 25 °C, and internal temperature is allowed to fluctuate along with the heat generation of batteries because the inside temperature is changing the heat generation of the batteries. Furthermore, the number of pins that were added to the enclosure is gradually increased from 1 pin to 81 pins, and pins were located at the centre of the enclosure since the central area was identified as a significant area. The diameter of pins was taken as 2.65 mm to match with the commercially available copper pins. The length of pins was changed from 4 mm to 15 mm to see the temperature variation along with the length of pins and the excess length protrude from the outside of the laminate. The simulation results for each configuration can be presented as follows.
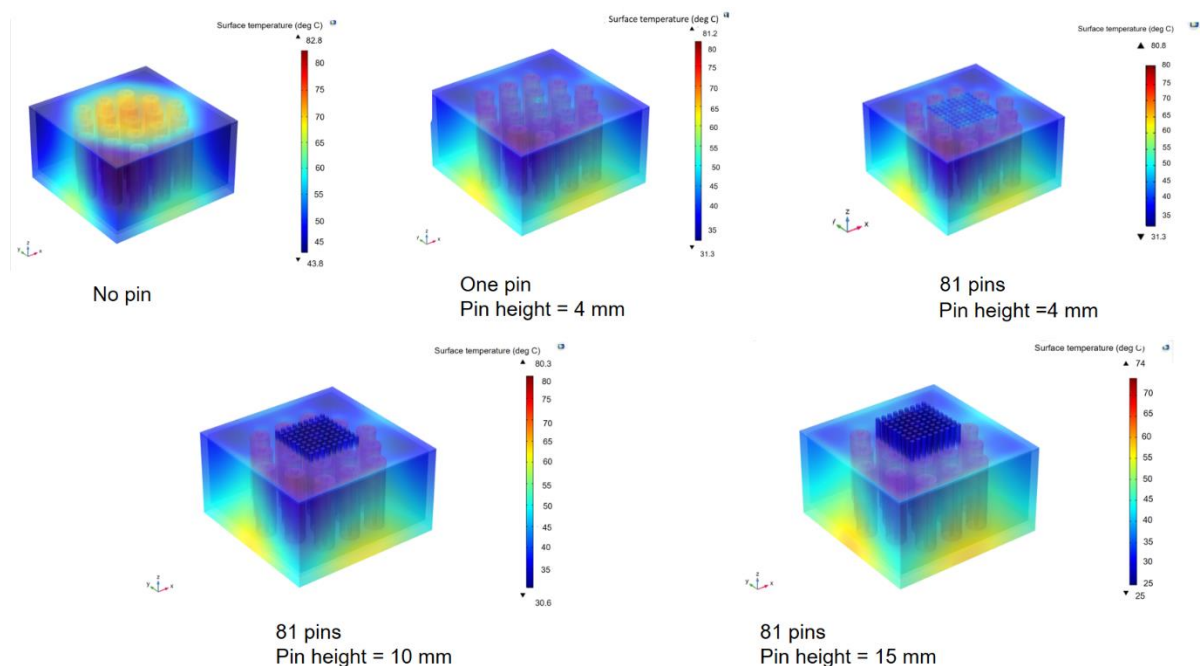
Figure 5.15. Simulation results at 1500 s for each configuration

As expected, longer pins lead to faster temperature reduction. Exposure of the pins on the inside of the composite enclosure will further enhance the cooling effect. Therefore, the pin length will be constraint by practical considerations such as area available around the enclosure and distance between the enclosure and the battery cell. For this study pins of 10mm height were used

5.1.2.3 Fabrication of the composite enclosure with pins

Before fabricating the composite enclosure with pins, it was first tried with the composite material plate. Initially, copper wires with a diameter of 2.65 mm were employed as the copper pins. To place the copper wires at desired locations, it was first tried with the polystyrene foam to locate them and the resin infusion conducted. The initial experimental arrangement with copper wires and the polystyrene foam can be figured out as follows:
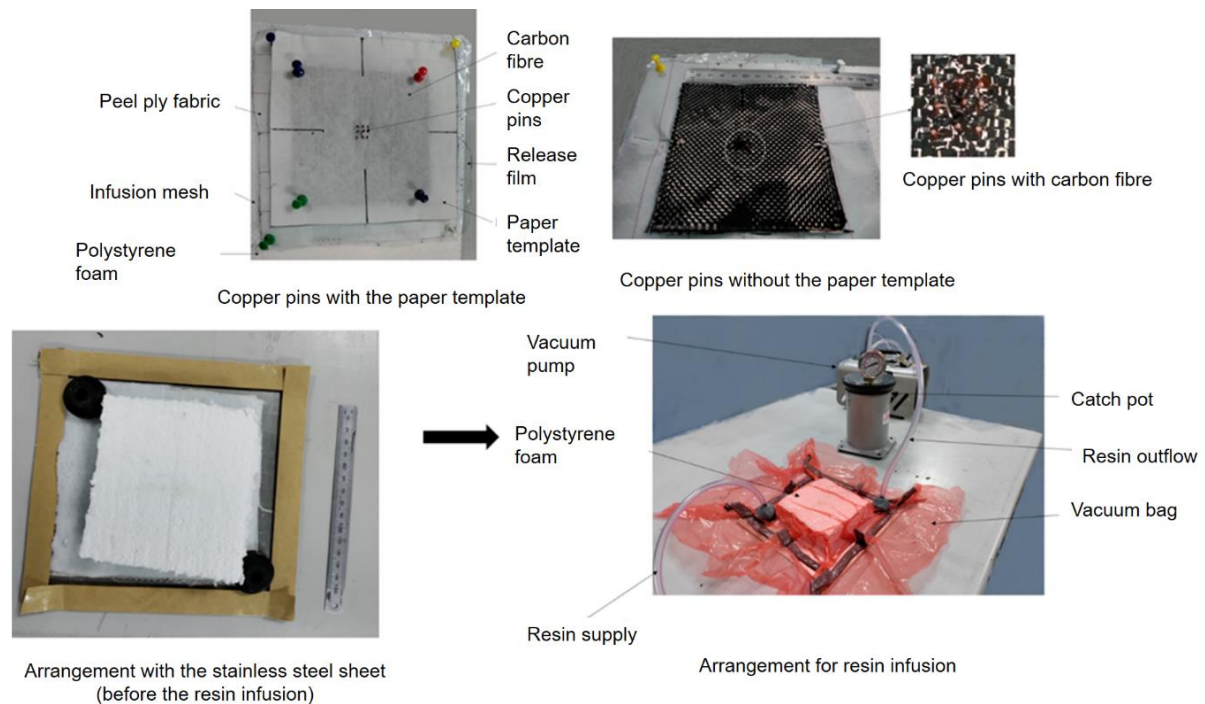
Figure 5.16. Initial experimental arrangement

However, as shown in Figure 5.17, the part was unsuccessful due to the air trapped by the polystyrene foam. Also, it was found that the copper wires are not the best solution for copper pins due to the improper bonding between copper wire and the fibre.
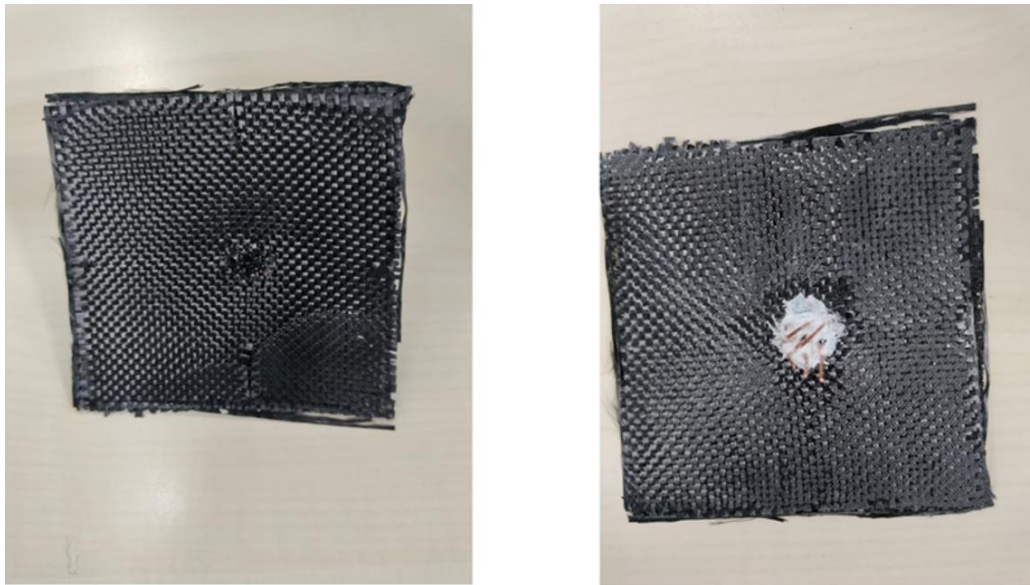
Part after the resin infusion

Figure 5.17. Final part after the resin infusion

After a few attempts with various types of holding boards (including breadboards and etc.), it was decided to use a Polytetrafluorethylene (PTFE) sheet as a holding board with copper nails. PTFE sheet is a high-performance engineering plastic and chemically inert material. Also, the PTFE sheet is easy to use in resin infusion since it is a self-releasing material. The arrangement was prepared as shown in the diagram.
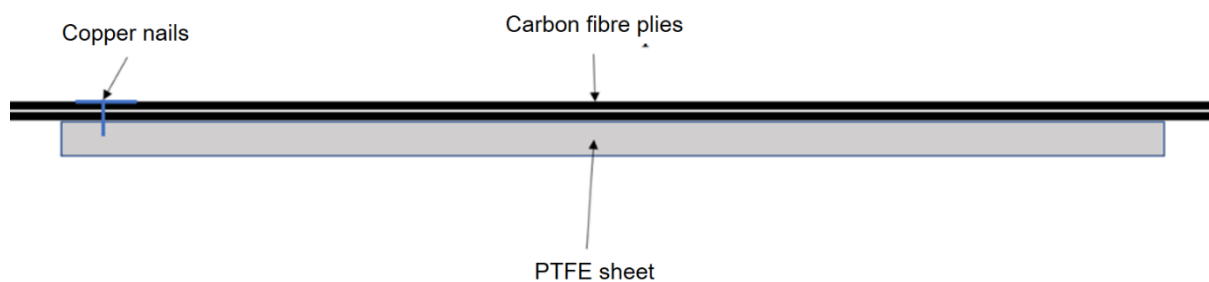
Figure 5.18. The experimental arrangement for PTFE sheet, copper nails and carbon fibre plies

The selected PTFE sheet has a thickness of 10 mm, and the selected copper nails has the length of 15 mm. However, the extra 5 mm length from the copper nails was removed to avoid damaging the vacuum bag. The experimental arrangement for resin infusion and the final part after the resin infusion are presented in Figure 5.19.
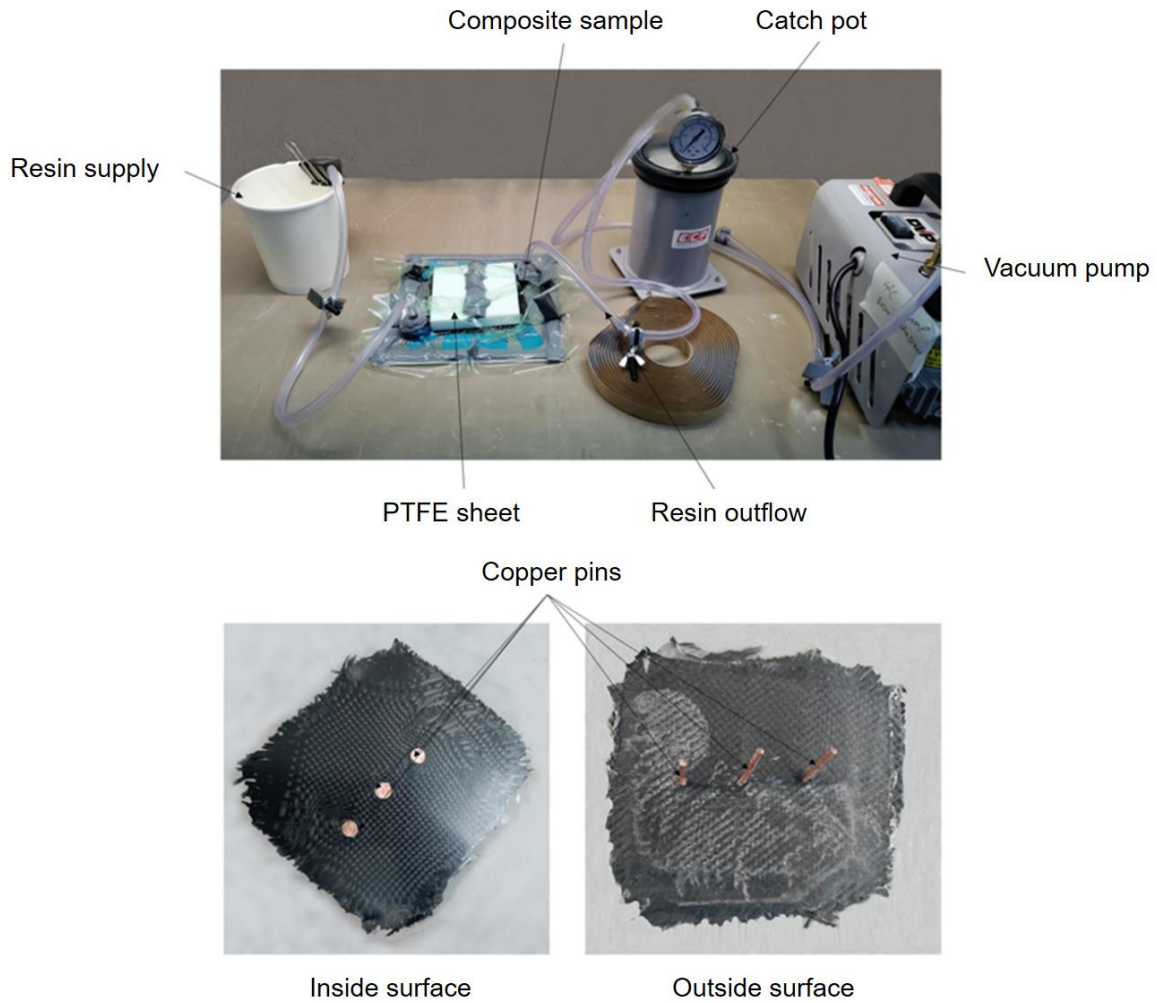
Figure 5.19. Experimental arrangement for resin infusion and the final part after the resin infusion

It was found that, there were some dry locations in the final part, and to avoid that, it was decided to use more resin in enclosure fabrication. Other than that, since all the properties of the final composite part were as desired, it was decided to continue the PTFE sheet with copper nails in enclosure fabrication.
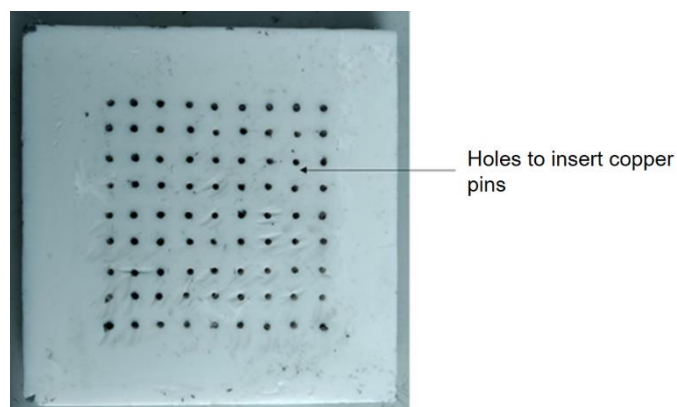
Figure 5.20. PTFE sheet for pins assembly

For the enclosure fabrication, as shown in Figure 5.18, copper nails were inserted into the PTFE sheet and the plies arrangement (including carbon fibre plies, peel ply and infusion mesh). Then the arrangement was placed on top of the mould. Carbon fibre plies were stuck to the mould tool using FusionFix™ composite adhesive. To avoid the risk of damaging vacuum bag, the pins' ends were covered using tacky tape and a piece of breather ply. As the final step, the whole arrangement was put under vacuum using the vacuum bag and vacuum pump for the resin infusion. The arrangements, process, and the final part were demonstrated as in Figure 5.21. The pink colour sheet was used to cover the whole assembly while cutting the sharp edges of the copper nails and the vacuum bag is showing in the green colour.

81 copper pins arrangement with the PTFE sheet

Arrangement before the resin infusion

Arrangement during the resin infusion

Final part after the resin infusion
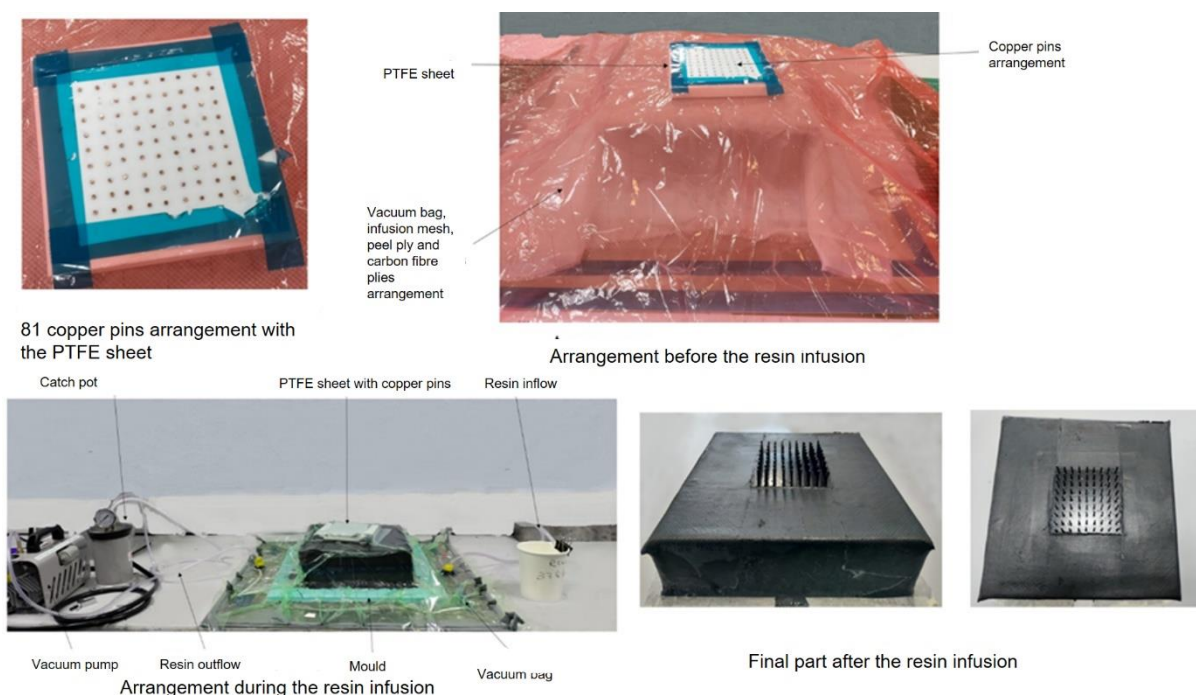
Figure 5.21. The arrangement, process and the final part

5.2 Thermal conductivity measurements

The thermal conductivity of the CFRP was measured according to the standards of ASTM C518-15 by means of the heat flow meter apparatus. As indicated in the standards, this test method covers the measurement of steady state thermal transmission through flat slab specimens. The measuring apparatus establishes steady state one dimensional heat flux through a test specimen between two parallel plates at constant but different temperatures. Fourier's law of heat conduction is used to calculate thermal conductivity and thermal resistance. It has been mentioned that the test method can be used for the measurements of thermal transmission through a wide range of specimen properties and environmental

conditions, applicable for ambient conditions of 10 to 40 °C with thicknesses up to 250 mm and with plate temperatures for -195 to 540 °C at 25 mm thickness.
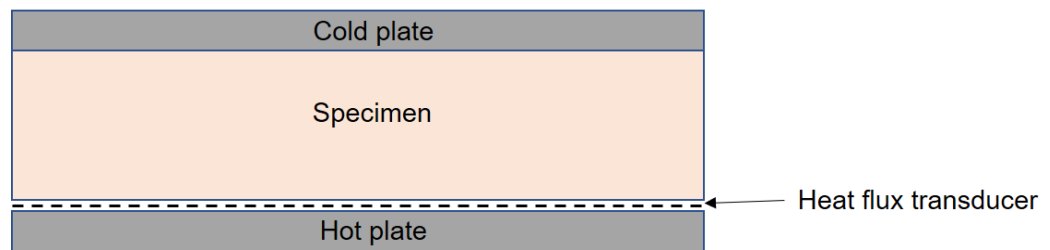
Figure 5.22. Apparatus with one heat flux transducer and one specimen

Three CFRP specimen which have the exact thickness of 3.6 mm were prepared according to the standards and they were fabricated using the same procedure and layup arrangement as in the resin infusion process for producing the composite enclosures.
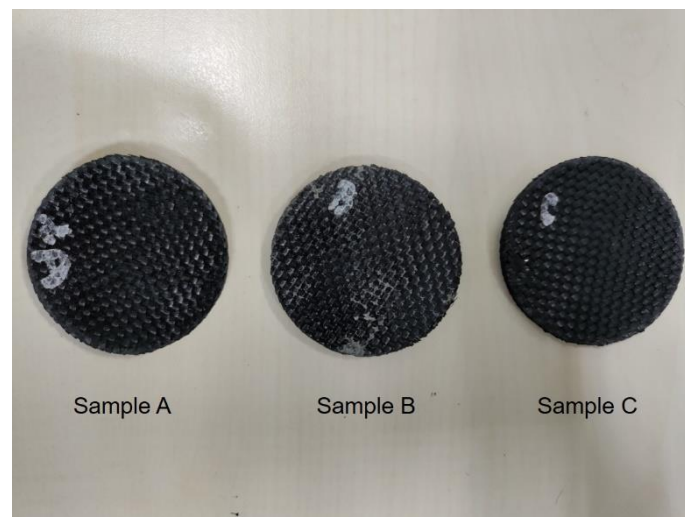
Figure 5.23. Three CFRP specimen

The measurements were conducted by considering five different temperatures up to 70 °C.(i.e. including 30, 40,50 ,60 and 70 °C) . Measurements were taken for three samples to consider the repeatability. The measured values for thermal conductivity with the temperature for three samples can be plotted as follows.
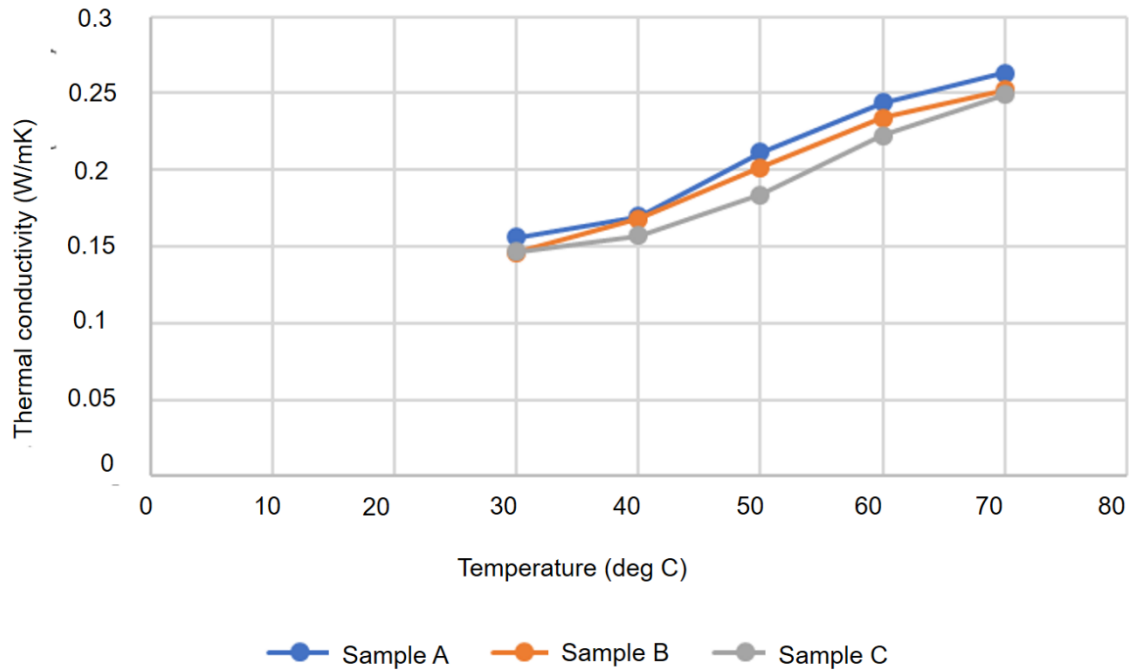
Figure 5.24. Thermal conductivity measurements along with the temperature for CFRP samples

Thermal conductivity generally increases with temperature due to the increased vibrational energy of atoms or molecules within a material as temperature rises. In simpler terms, as temperature increases, the particles in a material vibrate more vigorously, leading to more efficient transfer of thermal energy through the material. This increased vibrational energy enhances the ability of the material to conduct heat, resulting in higher thermal conductivity. Additionally, at higher temperatures, phonon scattering, which is a process that impedes the movement of heat-carrying vibrations (phonons), becomes less significant, further contributing to the overall increase in thermal conductivity.

In order to find out whether there is any significant difference between the thermal conductivity values of three samples, a one-way ANOVA test was conducted for the measurements. The results of ANOVA test can be figured out as follows.

Table 5.1. ANOVA test results

Descriptives

Thermal Conductivity (W/mK)

	Number of data	Mean	Std. Deviation	Std. Error	95% Confidence Interval for Mean (CI)		Minimum	Maximum
					Lower Bound	Upper Bound		
Sample A	5	0.21	0.05	.02	0.15	0.27	0.16	0.26
Sample B	5	0.20	0.44	.02	0.15	0.26	0.15	0.25
Sample C	5	0.19	0.04	.02	0.14	0.25	0.15	0.25
Total	15	0.20	0.04	.01	0.18	0.22	0.15	0.26

ANOVA					
Thermal Conductivity (W/mK)					
	Sum of Squares	Degree of freedom	Mean Square	*F*	Sig.(p)
Between Groups	0.001	2	0.000	0.181	0.837
Within Groups	0.024	12	0.002		
Total	0.025	14			

There was no significant difference between groups as determined by the one-way ANOVA (F (2,12) =0.181, p=0.837). Descriptives show that the mean value of thermal conductivity (0.2±0.01) was no significantly difference between sample A, sample B and sample C (p= [0.837], 95% CI = [0.21,0.20,0.19]). Therefore, there was no significant difference between the thermal conductivity values of three CFRP samples and the average value for thermal conductivity of CFRP can be taken as 0.20 W/mK.

The thermal conductivity of materials typically varies with temperature, so it's indeed a temperature-dependent quantity. Choosing a specific value, such as the statistical mean of 0.2 W/mK, rather than a value representative of the operating temperature of the composite enclosure, is done for practical reasons.

Firstly, the statistical mean provides a general indication of the material's thermal conductivity across a range of temperatures. It offers a baseline or average value that can be useful for

initial design or analysis purposes, especially when detailed temperature-dependent data is unavailable or impractical to use.

Secondly, the operating temperature of the composite enclosure may fluctuate or vary depending on the specific application or environmental conditions. Using a single value representative of the operating temperature might not accurately capture the material's behavior over the entire temperature range it could experience.

Therefore, by using the statistical mean value, it provides a reasonable approximation of the material's thermal conductivity that can be applied across different temperature scenarios, offering a pragmatic approach for analysis and design considerations.

Since the ANOVA test confirms that the thermal conductivity value for CFRP sample is 0.20 W/mK, it was used for the 3D simulation thermal conductivity model for CFRP by considering the upper temperature limit as 70 °C and the lower temperature limit as 30 °C. The model thickness was also taken as similar to the sample thickness of 3.6 mm. The simulation is carried out by assuming the isotropic thermal conductivity properties for 1500 s and the results can be figured out as follows.
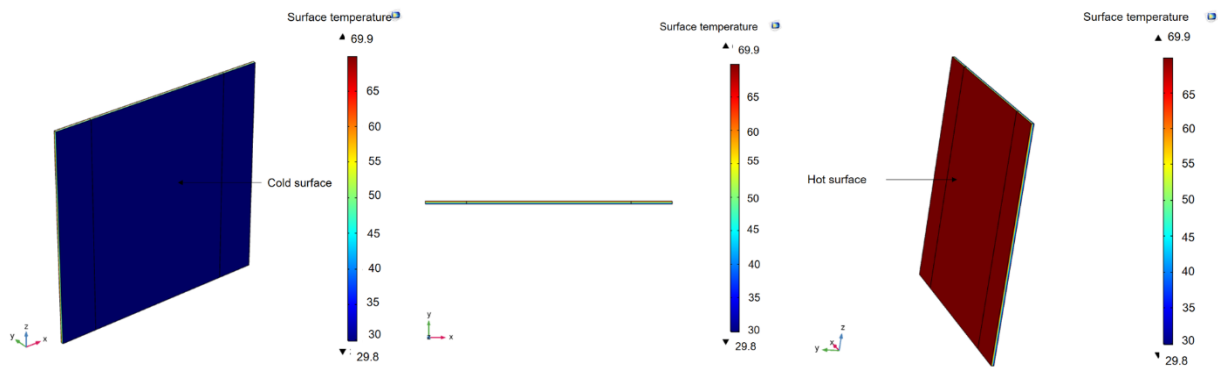
Figure 5.25. Temperature distribution results for CFRP sample
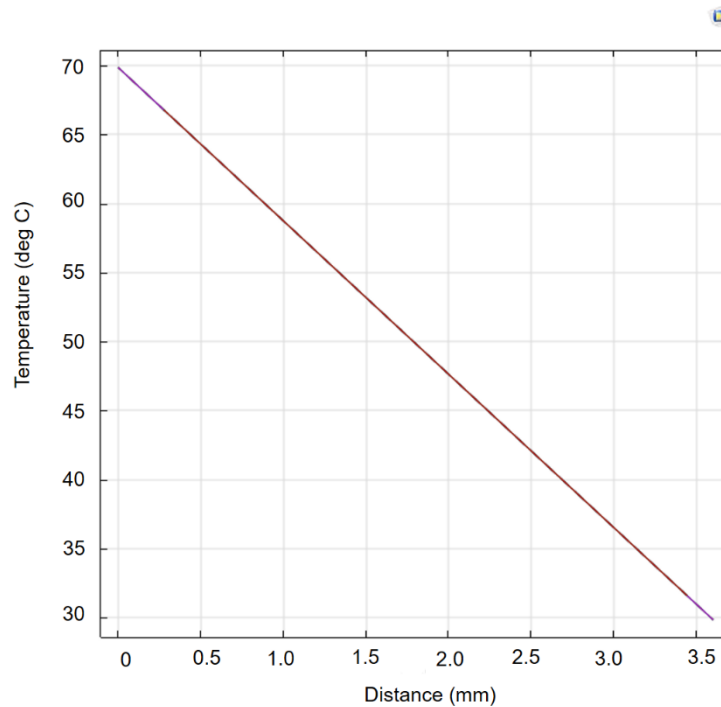
Figure 5.26. Temperature variation along with the distance

5.3 Temperature measurements without airflow- composite enclosure without and with pins

5.3.1 Experimental configurations

5.3.1.1 Experimental configurations -Without pins

K- type thermocouples are used to take the measurements during the experiment, and using adhesive tapes, they are positioned on the top surface of heating elements. The heating elements and the thermocouple arrangement were then covered using the composite enclosure without pins arrangement. PICO data loggers and a laptop are used to record the temperature. Measurements were taken for 2100s including 1500 s of heat up cycle and the remaining 600 s of cooling under natural convection.
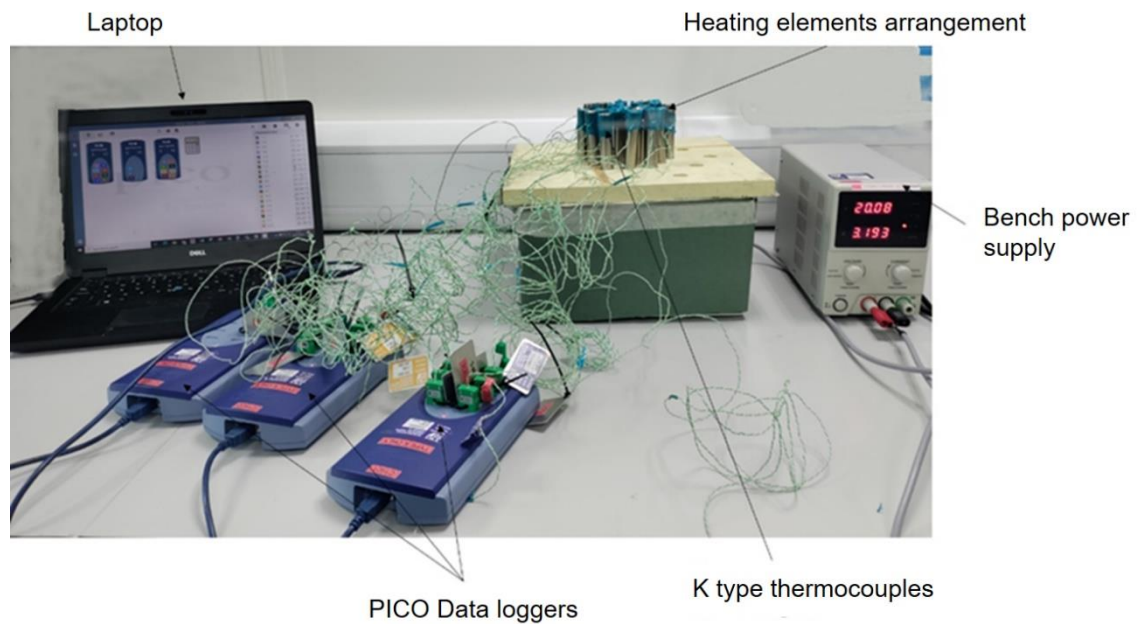
Figure 5.27. Experimental arrangement without the composite enclosure
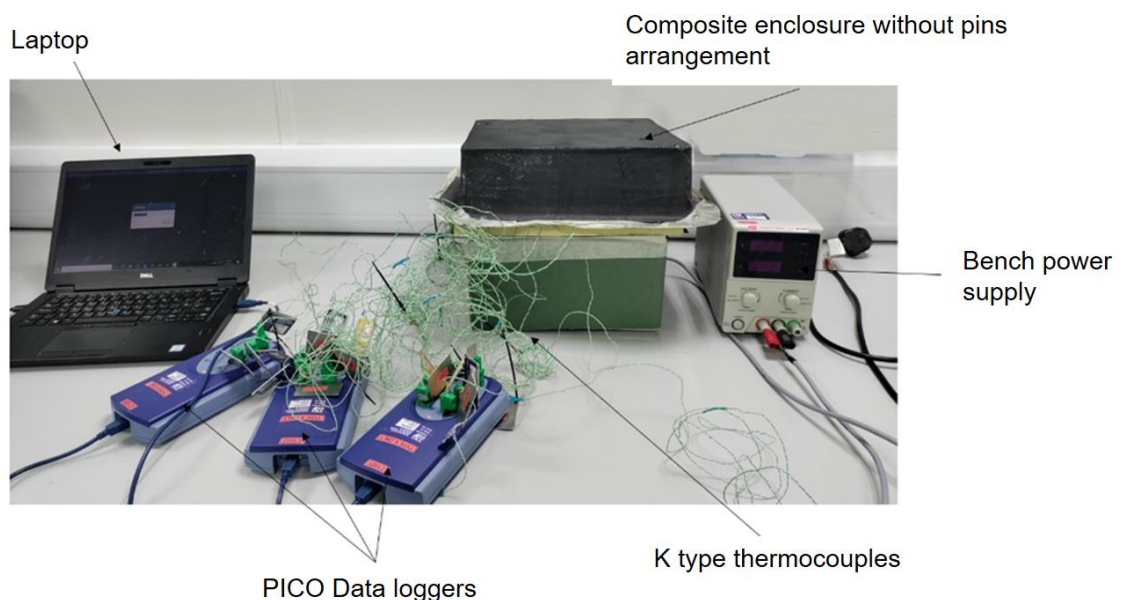
Figure 5.28.Experimental arrangement with the composite enclosure

The experiments were conducted with a power discontinuity for each 5 min to replicate the charge-discharge behaviour of an actual battery cell. In addition, thermocouples are numbered with the combination of relevant data logger and the relevant thermocouple input. The configuration of the thermocouples used in the experiment and the relevant heating element is shown in Figure 5.29.
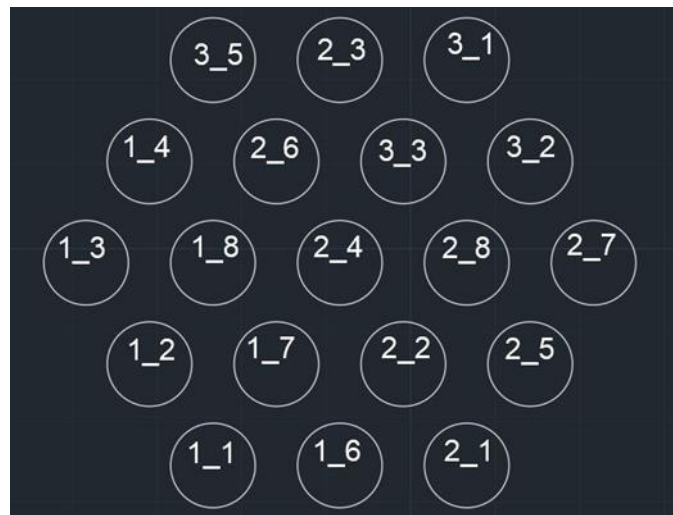
Figure 5.29.The configuration of thermocouples at the experiment

5.3.1.2 Experimental configuration -With pins

As in previous experiments, thermocouples are used to take the measurements, and they are positioned on the top surface of heating element using adhesive tapes. The heating elements and the thermocouple arrangement were then covered using the composite enclosure with pins arrangement. PICO data loggers and a laptop are used to record the temperature. Measurements were taken for 2100s.
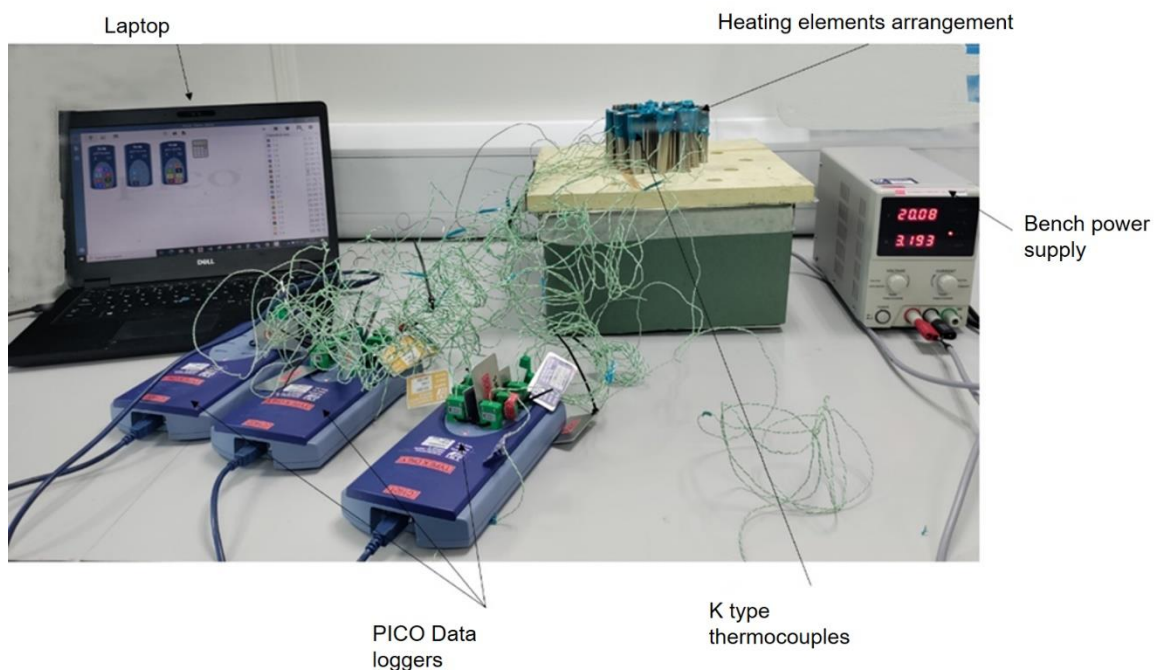
Figure 5.30. Experimental arrangement without the composite enclosure
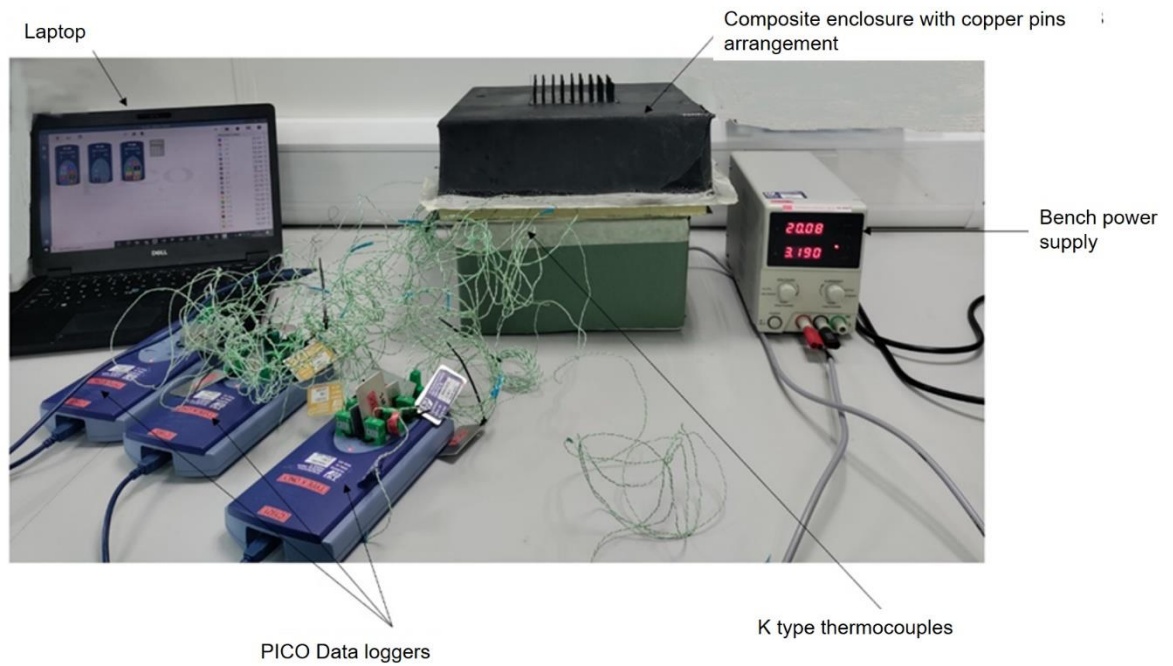
Figure 5.31. Experimental arrangement with the composite enclosure and copper pins

Furthermore, the experiments were conducted with a power discontinuity to replicate the charge-discharge behaviour of actual battery cell. In addition to that, thermocouples are numbered with the combination of relevant data logger and the relevant thermocouple input. The configuration with the thermocouples at the experiment and the relevant heating element are shown in Figure 5.32 .
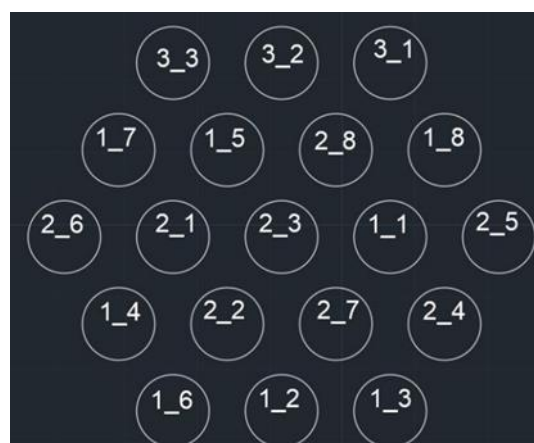
Figure 5.32. The configuration of thermocouples at the experiment

5.3.2 Comparison between experimental results and simulation results

5.3.2.1 Enclosure -Without pins

The simulations were conducted on the existing Li-ion battery module model with the CFRP composite enclosure, and the convection heat transfer coefficient for both the inside and outside of enclosure was taken as 5 W/m^{2}K. In addition to that, the environmental temperature was set as 25 ^{o}C, and the internal temperature was allowed to fluctuate along with the battery module temperature.

Furthermore, by considering the anisotropic material properties of thermal conductivity of CFRP, the composite enclosure thermal conductivity was set as k_{11}=0.68 W/mK; k_{22}=0.68 W/mK; k_{33}= 4.18 W/mK. [28]

In summary, the anisotropic nature of CFRP, where the arrangement of fibres affects thermal conductivity, leads to "k33" being significantly higher than "k11" and "k22" due to the relatively easier heat transfer across the layers of fibres, despite there being fewer fibres in that direction.
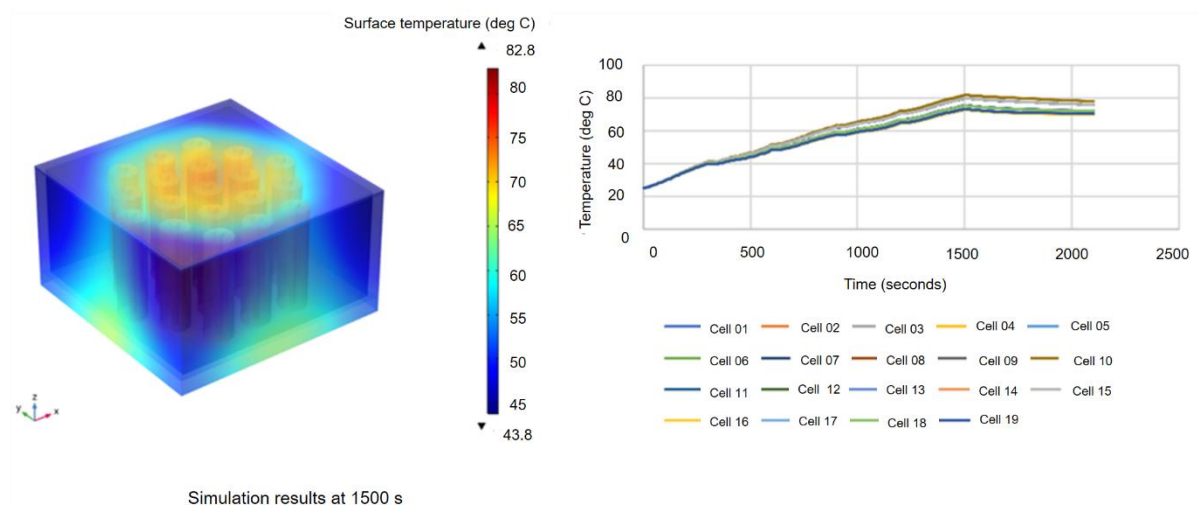
Figure 5.33. Simulation results with the composite enclosure

Three experiments were conducted for three CFRP enclosures to test the repeatability and under each enclosure, three experiments were conducted. The average results for three enclosures for 1500 s and 2100 s can be figured out in Annex 9:

Since the maximum temperature was found at the centre element for all three enclosures, for the comparison, the average experimental results and the simulation results for the centre element were considered. The common plots can be figured out as follows:
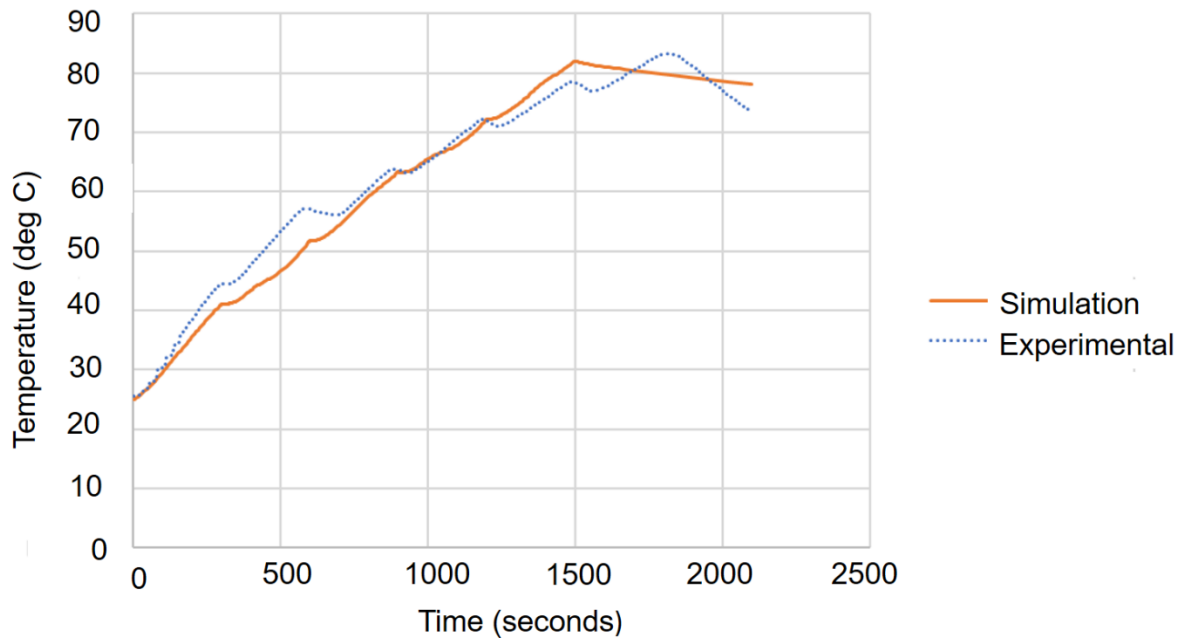
Figure 5.34. Comparison between experimental and simulation results for centre element

In order to find out whether there is any significant difference between both the experimental and simulation results, a one-way ANOVA test was conducted for both experimental and simulation results up to the discharge moment. (i.e.1500 s). The results of ANOVA test can be figured out as follows.

Table 5.2. ANOVA test results

Descriptives

Temperature °C

	Number of data	Mean	Std. Deviation	Std. Error	95% Confidence Interval for Mean (CI)		Minimum	Maximum
					Lower Bound	Upper Bound		
Experimental	1501	57.2	14.4	.37	59.4	57.9	25.5	78.5
Simulation	570	55.3	17.1	.72	53.9	56.7	25.0	82.0
Total	2071	56.7	15.2	.33	56.0	57.3	25.0	82.0

ANOVA

Temperature °C

	Sum of Squares	Degree of freedom	Mean Square	F	Sig.(p)

Between Groups	1394.3	1	1394.3	6.041	.014
Within Groups	477540.1	2069	230.8		
Total	478934.4	2070			

There was no significant difference between groups as determined by the one-way ANOVA (F (1,2069) =6.041, p=0.014). Descriptives show that the mean value of temperature (56.7±0.33) was no significantly difference between experimental and simulation (p= [0.014], 95% CI = [57.2,55.3]). Therefore, there was no significant difference between experimental and simulation data of the heating element, which is at the centre, up to the discharging moment for the composite enclosure.

5.3.2.2 Enclosure -With pins

The simulations were conducted with the pins' arrangement and the enclosure for the existing Li-ion battery model, and the dimensions of the pins were taken as similar to the experimental arrangement. (i.e. diameter of a copper pin: 2. 65 mm; height of a copper pin: 10 mm; distance between each copper pins: 6mm)

The convection heat transfer coefficient for both inside and outside of the enclosure was taken as 10 W/m^{2}K. The environmental temperature was set as 25 °C, and the internal temperature was allowed to fluctuate along with the battery module temperature. (based on the battery heat generation).

In addition to that, by considering the anisotropic material properties of thermal conductivity, the enclosure thermal conductivity was set as k_{ii} =0.68 W/mK; k_{22}= 0.68 W/mK; k_{33}=4.18 W/mK. The thermal conductivity for copper was taken as 398 W/mK.
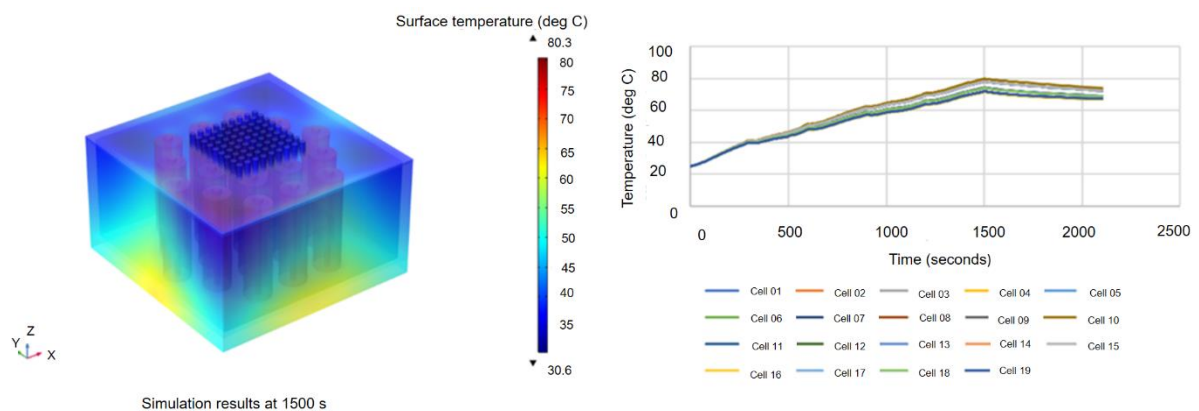
Figure 5.35. Simulation results with copper pins

As mentioned above, three experiments were conducted for three CFRP enclosures with the pin arrangement for the repeatability, and under each enclosure, three experiments were conducted. The average results for three enclosures for 1500 s and 2100 s can be figured out in Annex 10.

Since the maximum temperature was found at the centre element for all three enclosures, for the comparison, the average experimental results and the simulation results for the centre element were considered. The common plots can be figured out as follows:
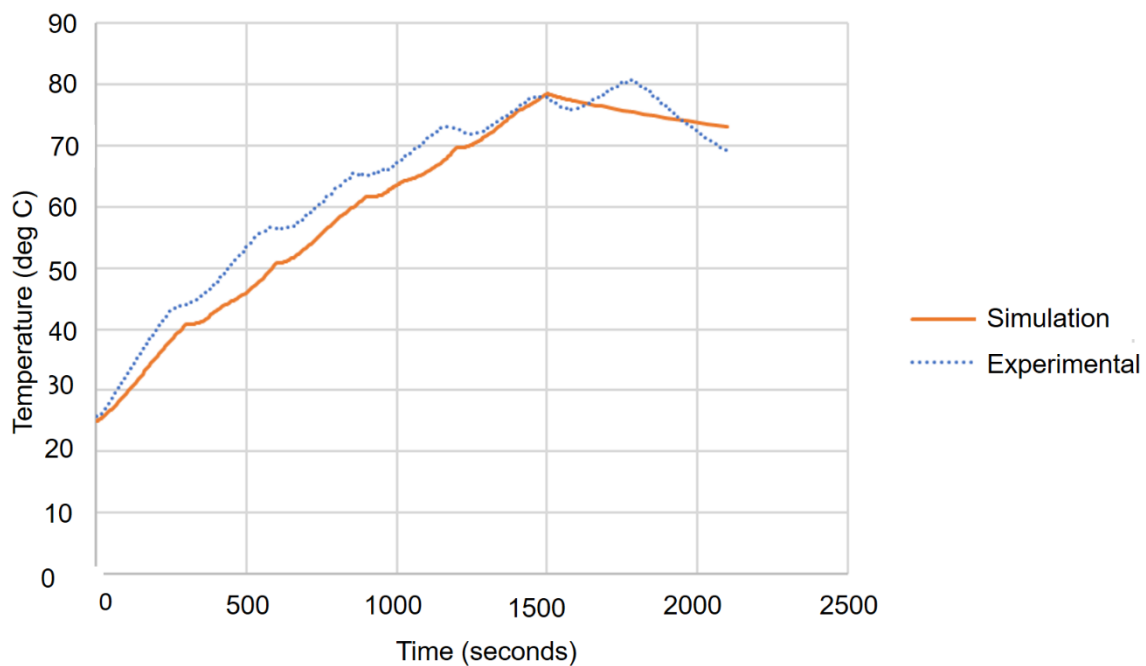
Figure 5.36. Comparison between experimental and simulation results for centre element

In order to find out whether there is any significant difference between both the experimental and simulation results, a one-way ANOVA test was conducted for both experimental and simulation results up to the discharge moment. (i.e.1500 s). The results of ANOVA test can be figured out as follows.

Table 5.3. ANOVA test results

Descriptives						
Temperature °C						
	Number of data	Mean	Std. Deviation	Std. Error	95% Confidence Interval for Mean (CI)	Minimum	Maximum

				Lower Bound	Upper Bound		
Experimental	1501	59.7	14.7	.38	59.0	60.4	26.0	80.8
Simulation	586	54.0	15.7	.65	52.7	55.3	25.0	78.5
Total	2087	58.1	15.2	.33	57.4	58.7	25.0	80.8

ANOVA					
Temperature °C					
	Sum of Squares	Degree of freedom	Mean Square	F	Sig.(p)
Between Groups	234.0	1	40.0	1.050	.306
Within Groups	471451.8	2085			
Total	471685.8	2086			

There was no significant difference between groups as determined by one-way ANOVA (F (1,2085) =1.050, p=0.306). Descriptives show that the mean value of temperature (58.1±0.33) was not significantly different between experimental and simulation (p= [0.306], 95% CI = [59.7,54.0]). Therefore, there was no significant difference between experimental and simulation data of the heating element, at the centre, up to the discharging moment for pin arrangement.

Furthermore, in order to observe the surface temperature variation in the enclosure with and without pins, the infrared thermography method was used, and the images were captured using a FLIR thermal camera. In infrared thermography, the total radiation received by the sensor (W_{tot}), can be considered as a combination of three types of radiation [79], i.e., The radiation from the object (W_{obj}), the radiation from the atmosphere (W_{atm}), and the reflected radiation from the surroundings of the object (W_{ref}). [79]

$$W_{tot} = W_{obj} + W_{ref} + W_{atm} \qquad (29)$$

The Equation (29) can be expanded as follows.

$$W_{tot} = \varepsilon\tau\sigma T_{obj}^4 + (1-\varepsilon)\tau\sigma T_{ref}^4 + (1-\tau)\sigma T_{atm}^4 \qquad (30)$$

where, σ is the Stefan- Boltzmann constant (5.67×10^{-8} W/m^{-2}K^{-4}) and ε denotes the emissivity of the object. τ is for the atmosphere transmittance parameter. T_{obj} and T_{ref} denote the temperature of the object and the surroundings of the object reflected towards the camera. T_{atm} is the atmospheric temperature.

Therefore, as indicated in Equation (30), the emissivity significantly reduces the radiation from the surroundings and the low emissivity can potentially affect the accuracy of readings [79]. To overcome this problem, the enclosure surface and pins are covered using a matt black paint since it will increase the surface emissivity. While getting the thermal images, the enclosure heats up using the battery module with standard-gap for 2100 s cycle and the results were captured at 1500s (i.e. the point where the maximum temperature is achieved). The centre location of the enclosure is considered for both with and without pin scenarios. In addition to that, all calibration parameters (Calibrated by FLIR systems) are reported in Table 5.4.

Table 5.4. Calibration parameter for IR thermography

Parameter	Value
Emissivity (ε)	0.98
Reflected apparent temperature (T_{ref})	20 °C
Relative humidity (RH%)	37%
Atmospheric temperature (T_{atm})	19 °C
Camera to enclosure distance	1.0 m

The infrared thermography results can be presented as follows.

Enclosure surface without pins   Enclosure surface with pins
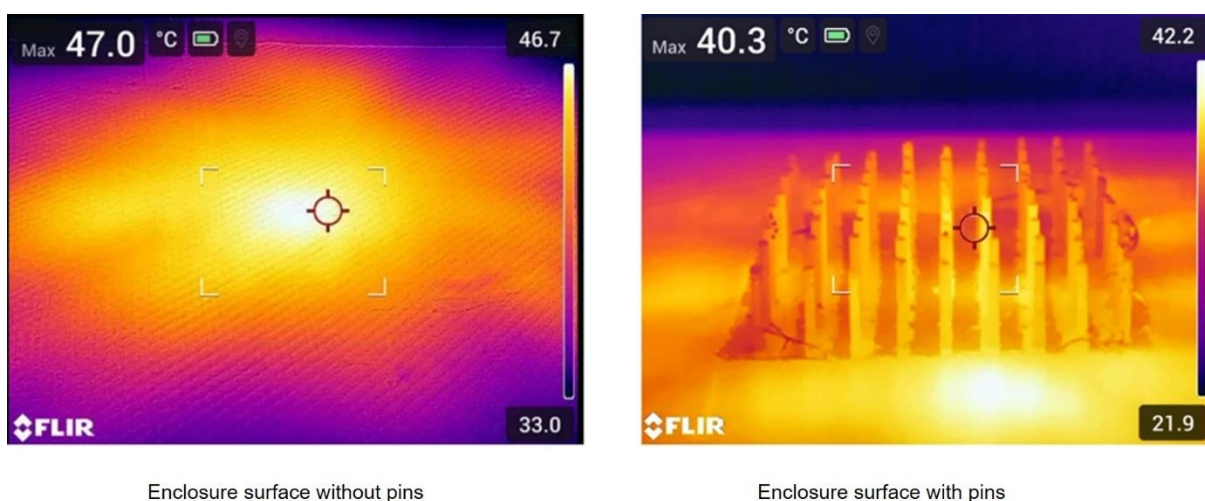
Figure 5.37. IR thermography results on the enclosure without pins and with pins

The IR thermography results indicate that when there are pins, the surface cooling effect is higher than when there are no pins. Without pins, the enclosure surface indicates the maximum temperature 47 °C, and with the pins the temperature was reducing for 40.3 °C.

However, to confirm that there is a heat conduction through the copper pin, the temperature variation along the pin and around the pin were also measured using K-type of thermocouples. The relevant results can be presented as follows.
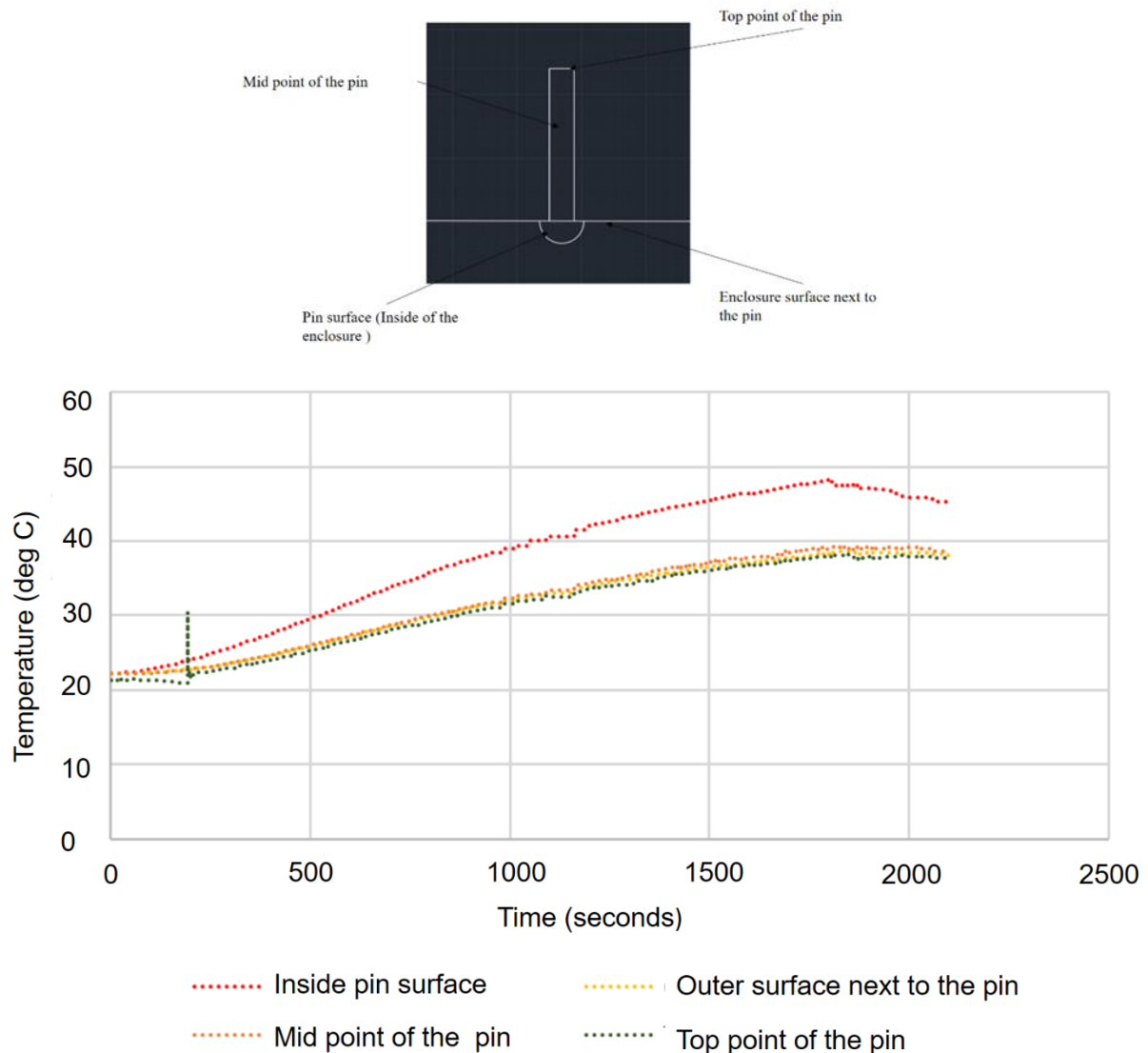
Figure 5.38. The temperature variation along with the pin and around the pin

As indicated in Figure 5.38 the maximum temperature can be found in the inside of the enclosure due to the heat generation of battery module. However, the temperature at the mid-point of the pin is higher than the temperature at outer surface next to the pin, and the temperature at top point of the pin is almost same to the temperature at the outer surface next

to the pin. Therefore, this confirms that the heat is conducting faster through the copper pin to the outside of the enclosure.

5.4 Discussion and Conclusion

Among three methods of composite manufacturing processes (including resin infusion, hand lay-up method, and resin infusion with a caul plate), resin infusion method was used to fabricate the composite enclosure.

By using the metallic enclosure, the experiments were conducted for the custom jig which contains 19 heating elements to find out the significant areas where the heat affects the most. The experimental results confirmed that the centre area of the enclosure is mostly affected due to the battery heat generation inside the enclosure.

To improve the thermal conductivity of the composite enclosure, it was decided to insert the metallic pins in significant areas, and since copper has the highest thermal conductivity among the common metals, copper was chosen. Here, the pins act as a thermal bridge between the air inside and outside of the enclosure.

Simulation and experimental results have a better agreement between each other for the scenarios of the enclosure and the enclosure with the copper pins arrangement. Furthermore, the simulation results, IR thermography results, and the experimental results confirmed that the copper pins arrangement is a better solution to conduct the heat that is accumulated inside the enclosure to the outside effectively without the use of any active cooling methods such as air-cooling or water cooling.

6 Overall discussion and conclusions

With the combination of modified Newman's equation, a three-dimensional CFD model was used in the heat transfer modelling of a Li-ion battery cell. Due to its high level of computational effectiveness and the limited involvement of both experimental and parametric data, the CFD model was used. The Newman's equation was associated with the CFD model to calculate the amount of heat generated inside the battery cell and the battery module.

Furthermore, the thermal performance of Li-ion battery module was discussed in the study by considering both analytical and simulation methods. Assumptions of the lumped model were applied in the analytical method of a single cell. Simulations were conducted by coupling both 1 D and 3 D model. In addition, thermal performance analyses were performed for different cell structures and the arrangement and structures include 1× 24, 3×8, 4×6 arrays rectangular arrangements and 19 cells hexagonal arrangement. Among all structures discussed in the study 4× 6 cubic structure was identified as the best choice in terms of the cooling capability. However, 19 cells hexagonal arrangement was identified as the best choice in terms of both cooling capability and space utilisation effect. Therefore, it was selected for further investigations throughout the project and the effect of inter-cell distance was also investigated. Results confirmed that the having a gap between battery cells reduces the mutual heating effect and increases the cooling effectiveness.

Experiments were conducted by considering the inter-cell distance between each cell. A custom jig that includes cylindrical heating elements with the same dimensions as the Li-ion battery cells was used to replicate the Li-ion battery module. Also, experiments were conducted by considering the scenarios of without enclosure, with the metallic enclosure and with the metallic enclosure and the airflow supply as well. The overall results for all scenarios indicate that the good agreement between simulation and experimental results. However, minor deviations are attributed to fixing issues of heating elements during the experiments. (Some elements tilt slightly, creating deviations from the ideal geometry of the battery module). Since the custom jig was validated experimentally with the simulation results, it was decided to continue the further investigations and experiments with the existing thermal modelling and the custom jig.

In addition, although there exists a turbulence effect, still there is a considerable reduction of the temperature inside the enclosure can be found with the airflow. However, since the research is more focused on the passive cooling methods than the active cooling, the experiments were continued without the airflow effect.

Also, it was found that with the discontinued power supply, the custom jig of heating elements demonstrates much the same behaviour as the battery module. Furthermore, since, the experimental results indicate that the temperature distribution in the standard gap scenario is more uniform and validated by the simulation results, the further experiments on the standard gap scenario with the discontinuous power supply were continued.

Due to its simplicity and the low cost, liquid composite moulding (LCM) technique was chosen. Among the methods of composite manufacturing processes (including resin infusion, and resin infusion with a caul plate), the resin infusion method was used to fabricate the composite enclosure. As the resin IN2 epoxy infusion resin was used with the carbon fibre for the fabrication.

A completely new idea for a composite casing is considered in this project. The composite casing will have a variable thermal conductivity, depending on the volume fraction and other conductive elements. The selective high conductivity in areas of the casing will create "Thermal avenues" close to the hot areas of the battery enclosure to provide passive heat dissipation in the areas needed the most. Therefore, experiments were conducted to identify the hot areas of the battery enclosure using the metallic enclosure and found that the significant areas are mainly located in the centre of the enclosure. This was confirmed by using the composite enclosure as well.

To improve the thermal conductivity of the composite enclosure with the use of conductive elements, it was decided to insert metallic pins in significant areas and since, copper has the highest thermal conductivity among the common metals, copper was chosen. Here, the pins act as a thermal bridge between the air inside and outside of the enclosure. Although, the insertion of copper pins to the composite enclosure with the resin infusion is challenging, with the assistance of a PTFE sheet it was achieved in the fabrication. However, for the commercialisation, the copper pins' insertion through the thickness is recommended using the z-pinning technique for composite battery casing.

Simulation and experimental results have a better agreement with each other for the scenarios of the composite enclosure and the composite enclosure with the copper pins arrangement. Furthermore, the simulation results, IR thermography results and experimental results confirmed that the copper pins arrangement is a better solution to conduct the heat that is accumulated inside the enclosure to the outside effectively without the use of any kind of active cooling methods such as air-cooling or water cooling. Also with the addition of 10 mm copper

pins, the overall thermal conductivity of the enclosure centre is become 167.41 W/mK and there is a 16,62% surface temperature reduction occurred with the addition of copper pins.

6.1 Benefits and trade-offs from the use of composite enclosure in battery modules

Since the automotive industry rapidly electrifies its fleets, interest is growing between original vehicle manufacturers and battery module producers in using composite materials for battery enclosures. It is because the composite enclosures can reduce the overall mass and the stack tolerances. It has mentioned that [80]; the empty metallic battery enclosure adds 110-160 kgs to the mass of a vehicle and currently it is identified as the heaviest component on the battery electric vehicle before the battery pack is loaded [80].

In addition, the battery enclosures can also be identified as multicomponent assemblies. As each component is attached to the previous one, the space taken up by the entire assembly is additive. However, it is more challenging and expensive to form the metal enclosures into complex shapes. If it is metal, then the enclosures must be produced in more pieces that take up additional space. However, the composite enclosures could be designed into more efficient shapes, which requires less space.

Also, when compared to metal, the composite enclosures have better impact performance and no effect due to the corrosion as with the metallic enclosures as well.

Therefore, by considering all these facts, the use of composite enclosures in battery modules can be identified as a better solution in terms of most aspects. However, since composites are thermally insulated materials, as mentioned in previous chapters, there is a risk of fires and thermal runaway events. To avoid these extreme situations and to make sure the vehicle and battery pack are safe, it is required to increase the thermal conductivity of the composite enclosures. Therefore, this project suggested inserting the metallic pins in the composite enclosure to increase the thermal conductivity, and through experiments, it was proven that the metallic pins arrangement effectively dissipated the inside heat to the outside without adding any additional considerable weight or complexity.

6.2   Suggestion for further work

In considering future developments, it is proposed to substitute metallic pins throughout the enclosure surface, leveraging the correlation between pin count and heat dissipation. However, it is important to address concerns regarding the potential impact of metal pins on the weight-saving advantages of composite materials. While metallic pins may offer effective heat dissipation, their inclusion could compromise the weight-saving benefits of using composites.

Though copper is highly thermally conductive, it is not used as a battery enclosure material due to its higher weight compared to composite enclosures. To mitigate this issue, the strategic placement of longer metallic pins at key locations is recommended, as this approach enhances heat dissipation while minimising the overall quantity of metal used. Additionally, incorporating tapered surfaces with fins can further optimise heat transfer without significantly increasing weight.

Furthermore, the project encountered a challenge in incorporating highly thermally conductive elements like graphene particles into the composite enclosures due to the resin infusion fabrication method employed. Nonetheless, it is feasible to integrate graphene pins using automated z-pinning techniques, thus offering a solution for future commercialisation or research endeavours. Consequently, preference is given to either graphene or copper pins. Graphene pins, composed of graphene or graphene-based materials, serve to optimise heat transfer within the enclosure, thus improving thermal management. By incorporating these pins into composite structures, researchers aim to enhance heat dissipation without compromising the weight-saving benefits of composites.

While graphene may incur higher costs, the use of lightweight composite materials for enclosure fabrication, coupled with a simplified heat removal mechanism devoid of active cooling components, promises heightened efficiency and effectiveness in both battery enclosures and vehicle battery lifespans. This approach not only maintains the weight-saving benefits of composites but also optimises thermal management for enhanced performance.

7 References

[1] A. A. Pesaran, "Battery Thermal Management in EVs and HEVs: Issues and Solutions", Accessed: Mar. 23, 2022. [Online]. Available: http://www.ctts.nrel.gov/BTM.

[2] H. Liu, Z. Wei, W. He, and J. Zhao, "Thermal issues about Li-ion batteries and recent progress in battery thermal management systems: A review," *Energy Convers Manag*, vol. 150, pp. 304–330, Oct. 2017, doi: 10.1016/J.ENCONMAN.2017.08.016.

[3] R. G. Anderson, "Requirements for Improved Battery Design and Performance," *SAE Technical Papers*, Feb. 1990, doi: 10.4271/900842.

[4] J. Gomez, R. Nelson, E. E. Kalu, M. H. Weatherspoon, and J. P. Zheng, "Equivalent circuit model parameters of a high-power Li-ion battery: Thermal and state of charge effects," *J Power Sources*, vol. 196, no. 10, pp. 4826–4831, May 2011, doi: 10.1016/J.JPOWSOUR.2010.12.107.

[5] B. Dickinson, J. Baer, O. A. Velev, and D. Swan, "Performance, management and testing requirements for hybrid electric vehicle batteries," *SAE Technical Papers*, 1998, doi: 10.4271/981905.

[6] T. F. Sharpe and R. S. Conell, "Low-temperature charging behaviour of lead-acid cells," *Journal of Applied Electrochemistry 1987 17:4*, vol. 17, no. 4, pp. 789–799, Jul. 1987, doi: 10.1007/BF01007816.

[7] "Temperature Dependent Performance of a Lead Acid Electric Vehicle Battery | 東京工業大学 附属図書館 文献データベース." https://tdl.libra.titech.ac.jp/journaldocs/en/recordID/article.bib-02/ZR000000056315?hit=-1&caller=xc-search (accessed Mar. 23, 2022).

[8] K. Onda, T. Ohshima, M. Nakayama, K. Fukuda, and T. Araki, "Thermal behaviour of small lithium-ion battery during rapid charge and discharge cycles," *J Power Sources*, vol. 158, no. 1, pp. 535–542, Jul. 2006, doi: 10.1016/J.JPOWSOUR.2005.08.049.

[9] N. H. F. Ismail, S. F. Toha, N. A. M. Azubir, N. H. Md Ishak, M. K. Hassan, and B. S. Ksm Ibrahim, "Simplified Heat Generation Model for Lithium ion battery used in Electric Vehicle," *IOP Conf Ser Mater Sci Eng*, vol. 53, no. 1, p. 012014, Dec. 2013, doi: 10.1088/1757-899X/53/1/012014.

[10] S. J. Drake *et al.*, "Heat generation rate measurement in a Li-ion cell at large C-rates through temperature and heat flux measurements," *J Power Sources*, vol. 285, pp. 266–273, Jul. 2015, doi: 10.1016/J.JPOWSOUR.2015.03.008.

[11] K. Chen, G. Unsworth, and X. Li, "Measurements of heat generation in prismatic Li-ion batteries," *J Power Sources*, vol. 261, pp. 28–37, Sep. 2014, doi: 10.1016/J.JPOWSOUR.2014.03.037.

References

[12] C. R. Pals and J. Newman, "Thermal Modeling of the Lithium/Polymer Battery II. Temperature Profiles in a Cell Stack".

[13] T. F. Fuller, M. Doyle, and J. Newman, "Simulation and Optimization of the Dual Lithium Ion Insertion Cell," *J Electrochem Soc*, vol. 141, no. 1, pp. 1–10, Jan. 1994, doi: 10.1149/1.2054684/XML.

[14] "This is a repository copy of A lumped thermal model of lithium-ion battery cells considering radiative heat transfer", doi: 10.1016/j.applthermaleng.2018.07.105.

[15] "Estimating Parameters for a Li-Ion Battery via a Lumped Model | COMSOL Blog." https://www.comsol.com/blogs/estimating-parameters-for-a-li-ion-battery-via-a-lumped-model/ (accessed Jul. 18, 2022).

[16] H. Ekström, B. Fridholm, and G. Lindbergh, "Comparison of lumped diffusion models for voltage prediction of a lithium-ion battery cell during dynamic loads," *J Power Sources*, vol. 402, pp. 296–300, Oct. 2018, doi: 10.1016/J.JPOWSOUR.2018.09.020.

[17] B. Ng, P. T. Coman, W. E. Mustain, and R. E. White, "Non-destructive parameter extraction for a reduced order lumped electrochemical-thermal model for simulating Li-ion full-cells," *J Power Sources*, vol. 445, p. 227296, Jan. 2020, doi: 10.1016/J.JPOWSOUR.2019.227296.

[18] "A Reduced-Order Lumped Model for Li-Ion Battery Packs during Operation," 2021, doi: 10.1149/1945-7111/ac2dcb.

[19] T. Wang, K. J. Tseng, J. Zhao, and Z. Wei, "Thermal investigation of lithium-ion battery module with different cell arrangement structures and forced air-cooling strategies," *Appl Energy*, vol. 134, pp. 229–238, Dec. 2014, doi: 10.1016/J.APENERGY.2014.08.013.

[20] "MATLAB - MathWorks - MATLAB & Simulink." https://www.mathworks.com/products/matlab.html (accessed Jul. 18, 2022).

[21] T. Huria, M. Ceraolo, J. Gazzarri, and R. Jackey, "High Fidelity Electrical Model with Thermal Dependence for Characterization and Simulation of High-Power Lithium Battery Cells".

[22] U. S. Kim, C. B. Shin, and C. S. Kim, "Effect of electrode configuration on the thermal behaviour of a lithium-polymer battery," *J Power Sources*, vol. 180, no. 2, pp. 909–916, Jun. 2008, doi: 10.1016/J.JPOWSOUR.2007.09.054.

[23] K. H. Kwon, C. B. Shin, T. H. Kang, and C. S. Kim, "A two-dimensional modelling of a lithium-polymer battery," *J Power Sources*, vol. 163, no. 1, pp. 151–157, Dec. 2006, doi: 10.1016/J.JPOWSOUR.2006.03.012.

[24] J. Yi, B. Koo, and C. B. Shin, "Three-dimensional modelling of the thermal behaviour of a lithium-ion battery module for hybrid electric vehicle applications," *Energies (Basel)*, vol. 7, no. 11, pp. 7586–7601, 2014, doi: 10.3390/EN7117586.

[25] R. Hsissou, R. Seghiri, Z. Benzekri, M. Hilali, M. Rafik, and A. Elharfi, "Polymer composite materials: A comprehensive review," *Compos Struct*, vol. 262, p. 113640, Apr. 2021, doi: 10.1016/j.compstruct.2021.113640.

References

[26] S. Herath, M. Jayasekara, and C. Mallikarachchi, "Parametric Study on the Homogenized Response of Woven Carbon Fibre Composites," in *2020 Moratuwa Engineering Research Conference (MERCon)*, Jul. 2020, pp. 36–41. doi: 10.1109/MERCon50084.2020.9185307.

[27] "Mechanics of Composite Materials, Second Edition (Materials Science & Engineering Series) by Robert M. Jones - PDF Drive." https://www.pdfdrive.com/mechanics-of-composite-materials-second-edition-materials-science-engineering-series-e185533223.html (accessed Nov. 01, 2022).

[28] H. Herath and H. Mallikarachchi, "Modified ply thickness for classical lamination theory for thin woven fibre composites," 2016, Accessed: Nov. 07, 2022. [Online]. Available: http://dl.lib.uom.lk/handle/123/13079

[29] "Principles of the Manufacturing of Composite Materials - Suong V. Hoa - Google Books." https://books.google.co.uk/books?hl=en&lr=&id=BiplTS70dw0C&oi=fnd&pg=PR7&dq=composite+manufacturing&ots=2G6BjQIEQ-&sig=AYZQQhhmtYEl0Zupszl2yLhyg_E&redir_esc=y#v=onepage&q=composite%20manufacturing&f=false (accessed Nov. 02, 2022).

[30] "Filament Winding - Open Molding | CompositesLab." https://compositeslab.com/composites-manufacturing-processes/open-molding/filament-winding/ (accessed Nov. 02, 2022).

[31] M. R. M. Jamir, M. S. A. Majid, and A. Khasri, "Natural lightweight hybrid composites for aircraft structural applications," *Sustainable Composites for Aerospace Applications*, pp. 155–170, Jan. 2018, doi: 10.1016/B978-0-08-102131-6.00008-6.

[32] T. F. Starr, *Pultrusion for engineers*. Accessed: Nov. 03, 2022. [Online]. Available: http://www.sciencedirect.com:5070/book/9781855734258/pultrusion-for-engineers

[33] S. Konstantopoulos, C. Hueber, I. Antoniadis, J. Summerscales, and R. Schledjewski, "Liquid composite molding reproducibility in real-world production of fiber reinforced polymeric composites: a review of challenges and solutions," *Advanced Manufacturing: Polymer & Composites Science*, vol. 5, no. 3, pp. 85–99, Jul. 2019, doi: 10.1080/20550340.2019.1635778.

[34] A. Brasington, C. Sacco, J. Halbritter, R. Wehbe, and R. Harik, "Automated fiber placement: A review of history, current technologies, and future paths forward," *Composites Part C: Open Access*, vol. 6, p. 100182, Oct. 2021, doi: 10.1016/j.jcomc.2021.100182.

[35] B. Mutnuri, "Thermal conductivity characterization of composite materials." [Online]. Available: https://researchrepository.wvu.edu/etd

[36] T. R. Tauchert, "Thermal Stresses at Spherical Inclusions in Uniform Heat Flow," *J Compos Mater*, vol. 2, no. 4, pp. 478–486, Oct. 1968, doi: 10.1177/002199836800200408.

[37] D. P. H. Hasselman, "Effect of Thermal Conductivity Mismatch on the Thermal Stresses in a Dispersed Phase-Continuous Matrix Composite Material Undergoing Steady-State Heat

Flow," *J Compos Mater*, vol. 36, no. 13, pp. 1605–1613, Jul. 2002, doi: 10.1177/0021998302036013576.

[38] N. Iwamoto, M. M. F. Yuen, and H. Fan, "Molecular modelling and multiscaling issues for electronic material applications," *Molecular Modeling and Multiscaling Issues for Electronic Material Applications*, pp. 1–258, Jan. 2012, doi: 10.1007/978-1-4614-1728-6/COVER.

[39] A. P. Mouritz, "Review of z-pinned composite laminates," *Compos Part A Appl Sci Manuf*, vol. 38, no. 12, pp. 2383–2397, Dec. 2007, doi: 10.1016/J.COMPOSITESA.2007.08.016.

[40] I. Gnaba, X. Legrand, P. Wang, and D. Soulat, "Through-the-thickness reinforcement for composite structures: A review," *Journal of Industrial Textiles*, vol. 49, no. 1, pp. 71–96, Jul. 2019, doi: 10.1177/1528083718772299/ASSET/IMAGES/LARGE/10.1177_1528083718772299-FIG2.JPEG.

[41] D. D. R. Cartié, G. Dell'Anno, E. Poulin, and I. K. Partridge, "3D reinforcement of stiffener-to-skin T-joints by Z-pinning and tufting," *Eng Fract Mech*, vol. 73, no. 16, pp. 2532–2540, Nov. 2006, doi: 10.1016/J.ENGFRACMECH.2006.06.012.

[42] K. Dransfield, C. Baillie, and Y. W. Mai, "Improving the delamination resistance of CFRP by stitching—a review," *Compos Sci Technol*, vol. 50, no. 3, pp. 305–317, Jan. 1994, doi: 10.1016/0266-3538(94)90019-1.

[43] L. Tong, A. P. Mouritz, and M. K. Bannister, *3D Fibre Reinforced Polymer Composites*. Elsevier, 2002. Accessed: Nov. 07, 2022. [Online]. Available: http://www.sciencedirect.com:5070/book/9780080439389/3d-fibre-reinforced-polymer-composites

[44] S. Zhang *et al.*, "Through-thickness thermal conductivity enhancement and tensile response of carbon fiber-reinforced polymer composites," *Compos B Eng*, vol. 165, pp. 183–192, May 2019, doi: 10.1016/J.COMPOSITESB.2018.11.114.

[45] J. Schuster, D. Heider, K. Sharp, and M. Glowania, "Thermal conductivities of three-dimensionally woven fabric composites," *Compos Sci Technol*, vol. 68, no. 9, pp. 2085–2091, Jul. 2008, doi: 10.1016/J.COMPSCITECH.2008.03.024.

[46] S. Han and D. D. L. Chung, "Increasing the through-thickness thermal conductivity of carbon fiber polymer–matrix composite by curing pressure increase and filler incorporation," *Compos Sci Technol*, vol. 71, no. 16, pp. 1944–1952, Nov. 2011, doi: 10.1016/J.COMPSCITECH.2011.09.011.

[47] L. Xia, G. L. Zhao, X. X. Huang, G. W. Wen, J. Q. Dai, and Z. H. Zhao, "Effect of graphite intercalation compounds in the interfacial zone on the mechanical and thermal properties of unidirectional carbon fiber reinforced spodumene composite," *Acta Mater*, vol. 61, no. 9, pp. 3522–3532, May 2013, doi: 10.1016/J.ACTAMAT.2013.02.046.

References

[48] W. Q. Li, Z. G. Qu, Y. L. He, and Y. B. Tao, "Experimental study of a passive thermal management system for high-powered lithium ion batteries using porous metal foam saturated with phase change materials," *J Power Sources*, vol. 255, pp. 9–15, Jun. 2014, doi: 10.1016/J.JPOWSOUR.2014.01.006.

[49] R. Kizilel, A. Lateef, R. Sabbah, M. M. Farid, J. R. Selman, and S. Al-Hallaj, "Passive control of temperature excursion and uniformity in high-energy Li-ion battery packs at high current and ambient temperature," *J Power Sources*, vol. 183, no. 1, pp. 370–375, Aug. 2008, doi: 10.1016/J.JPOWSOUR.2008.04.050.

[50] B. Mortazavi, H. Yang, F. Mohebbi, G. Cuniberti, and T. Rabczuk, "Graphene or h-BN paraffin composite structures for the thermal management of Li-ion batteries: A multiscale investigation," *Appl Energy*, vol. 202, pp. 323–334, Jun. 2017, doi: 10.1016/j.apenergy.2017.05.175.

[51] M. Li, Z. Fang, S. Wang, Y. Gu, Y. Li, and Z. Zhang, "Thermal conductivity enhancement and heat transport mechanism of carbon fiber z-pin graphite composite structures," *Compos B Eng*, vol. 172, pp. 603–611, Sep. 2019, doi: 10.1016/J.COMPOSITESB.2019.05.092.

[52] B. Mortazavi, H. Yang, F. Mohebbi, G. Cuniberti, and T. Rabczuk, "Graphene or h-BN paraffin composite structures for the thermal management of Li-ion batteries: A multiscale investigation," *Appl Energy*, vol. 202, pp. 323–334, Sep. 2017, doi: 10.1016/J.APENERGY.2017.05.175.

[53] J. Schuster, D. Heider, K. Sharp, and M. Glowania, "Thermal conductivities of three-dimensionally woven fabric composites," *Compos Sci Technol*, vol. 68, no. 9, pp. 2085–2091, Jul. 2008, doi: 10.1016/J.COMPSCITECH.2008.03.024.

[54] J. Schuster, D. Heider, K. Sharp, and M. Glowania, "Measuring and modelling the thermal conductivities of three-dimensionally woven fabric composites," *Mechanics of Composite Materials*, vol. 45, no. 2, pp. 165–174, Mar. 2009, doi: 10.1007/s11029-009-9072-y.

[55] C. Park and A. K. Jaura, "Dynamic thermal model of Li-Ion battery for predictive behavior in hybrid and fuel cell vehicles," *SAE Technical Papers*, 2003, doi: 10.4271/2003-01-2286.

[56] H. Sun and R. Dixon, "Development of cooling strategy for an air-cooled lithium-ion battery pack," *J Power Sources*, vol. 272, pp. 404–414, Dec. 2014, doi: 10.1016/J.JPOWSOUR.2014.08.107.

[57] S. K. Mohammadian, Y. L. He, and Y. Zhang, "Internal cooling of a lithium-ion battery using electrolyte as coolant through microchannels embedded inside the electrodes," *J Power Sources*, vol. 293, pp. 458–466, Oct. 2015, doi: 10.1016/J.JPOWSOUR.2015.05.055.

[58] K. Yu, X. Yang, Y. Cheng, and C. Li, "Thermal analysis and two-directional air flow thermal management for lithium-ion battery pack," *J Power Sources*, vol. 270, pp. 193–200, Dec. 2014, doi: 10.1016/J.JPOWSOUR.2014.07.086.

References

[59] J. Fan, "On the discharge capability and its limiting factors of commercial 18650 Li-ion cell at low temperatures," *J Power Sources*, vol. 117, no. 1–2, pp. 170–178, May 2003, doi: 10.1016/S0378-7753(03)00354-9.

[60] B. L. McKinney, G. L. Wierschem, and E. N. Mrotek, "Thermal Management of Lead-Acid Batteries for Electric Vehicles," *SAE Technical Papers*, Feb. 1983, doi: 10.4271/830229.

[61] S. C. Chen, C. C. Wan, and Y. Y. Wang, "Thermal analysis of lithium-ion batteries," *J Power Sources*, vol. 140, no. 1, pp. 111–124, Jan. 2005, doi: 10.1016/J.JPOWSOUR.2004.05.064.

[62] C. Lan, J. Xu, Y. Qiao, and Y. Ma, "Thermal management for high power lithium-ion battery by minichannels aluminium tubes," *Appl Therm Eng*, vol. 101, pp. 284–292, May 2016, doi: 10.1016/J.APPLTHERMALENG.2016.02.070.

[63] X. Zhang, "Thermal analysis of a cylindrical lithium-ion battery," *Electrochim Acta*, vol. 56, no. 3, pp. 1246–1255, Jan. 2011, doi: 10.1016/J.ELECTACTA.2010.10.054.

[64] X. Tong, J. A. Khan, and M. R. Amin, "ENHANCEMENT OF HEAT TRANSFER BY INSERTING A METAL MATRIX INTO A PHASE CHANGE MATERIAL," *http://dx.doi.org/10.1080/10407789608913832*, vol. 30, no. 2, pp. 125–141, 2007, doi: 10.1080/10407789608913832.

[65] Y. Huo and Z. Rao, "The numerical investigation of nanofluid based cylinder battery thermal management using lattice Boltzmann method," *Int J Heat Mass Transf*, vol. 91, pp. 374–384, Dec. 2015, doi: 10.1016/J.IJHEATMASSTRANSFER.2015.07.128.

[66] C. Y. Zhao, T. J. Lu, and H. P. Hodson, "Natural convection in metal foams with open cells," *Int J Heat Mass Transf*, vol. 48, no. 12, pp. 2452–2463, Jun. 2005, doi: 10.1016/J.IJHEATMASSTRANSFER.2005.01.002.

[67] X. Duan and G. F. Naterer, "Heat transfer in phase change materials for thermal management of electric vehicle battery modules," *Int J Heat Mass Transf*, vol. 53, no. 23–24, pp. 5176–5182, Nov. 2010, doi: 10.1016/J.IJHEATMASSTRANSFER.2010.07.044.

[68] J. Stoudmann, R. Rozsnyo, T. Mackin, and J. Dunning, "Heat Generation Modeling of Two Lithium Batteries: From the Cell to the Pack in COMSOL Multiphysics® Software".

[69] P. M. Gomadam, R. E. White, and J. W. Weidner, "Modeling heat conduction in spiral geometries," *Proceedings - Electrochemical Society*, vol. PV 2002-30, no. 10, pp. 146–159, Aug. 2005, doi: 10.1149/1.1605743/XML.

[70] "The Composition of EV Batteries: Cells? Modules? Packs? Let's Understand Properly!" https://www.samsungsdi.com/column/all/detail/54344.html (accessed May 19, 2022).

[71] "Nissan LEAF Battery Life: Your Guide to Maintenance and Care | EVgo | Electric Vehicle (EV) Charging Stations - EV Fast Chargers." https://www.evgo.com/blog/nissan-leaf-battery-life/ (accessed May 19, 2022).

References

[72]   M. N. Khan *et al.,* "Air cooled lithium-ion battery with cylindrical cell in phase change material filled cavity of different shapes," *J Energy Storage*, vol. 50, p. 104573, Jun. 2022, doi: 10.1016/J.EST.2022.104573.

[73]   K. Rumpf *et al.*, "Thermal Management of Various Battery array arrangement at various Environmental conditions for hybrid and electrical vehicles," *J Phys Conf Ser*, vol. 2178, no. 1, p. 012020, Feb. 2022, doi: 10.1088/1742-6596/2178/1/012020.

[74]   "CN101937977A - Production method for regular hexagonal prism-shaped battery case - Google Patents." https://patents.google.com/patent/CN101937977A/en (accessed May 13, 2022).

[75]   M. Broussely *et al.*, "Main aging mechanisms in Li ion batteries," *J Power Sources*, vol. 146, no. 1–2, pp. 90–96, Aug. 2005, doi: 10.1016/J.JPOWSOUR.2005.03.172.

[76]   "One-way ANOVA in SPSS Statistics - Step-by-step procedure including testing of assumptions." https://statistics.laerd.com/spss-tutorials/one-way-anova-using-spss-statistics.php (accessed May 23, 2022).

[77]   "IN2 EPOXY INFUSION RESIN-Technical Datasheet", Accessed: Nov. 28, 2022. [Online]. Available: www.easycomposites.co.uk|sales@easycomposites.co.uk

[78]   "Which Metals Conduct Heat Best? | Metal Supermarkets UK." https://www.metalsupermarkets.co.uk/which-metals-conduct-heat-best/ (accessed Nov. 29, 2022).

[79]   N. Zobeiry, J. Park, and A. Poursartip, "An infrared thermography-based method for the evaluation of the thermal response of tooling for composites manufacturing", doi: 10.1177/0021998318798444.

[80]   Price, performance, protection: EV battery enclosures, Part 1 | CompositesWorld." https://www.compositesworld.com/articles/price-performance-protection-ev-battery-enclosures-part-1 (accessed Feb. 09, 2023)

[81]   S. Santhanagopalan , Q. Zhang , K. Kumaresan and R. E. White , "Parameter Estimation and Life Modeling of Lithium-Ion Cells," *Journal of the Electrochemical Society,* vol. 155, no. 4, pp. 345-353, 2008.

[82]   M. Guo, . G.-H. Kim and . R. E. White, "A three-dimensional multi-physics model for a Li-ion battery," *Journal of power sources,* vol. 240, pp. 80-94, 2016.

[83]   M. Chen and Gabriel A. Rincon-Mora, "Accurate, Compact, and Power-Efficient Li-Ion Battery Charger Circuit," *IEEE Transactions on Circuits and Systems II: Express Briefs,* vol. 53, no. 11, pp. 1180 - 1184, 2006.

8 Appendix

- Annex 1
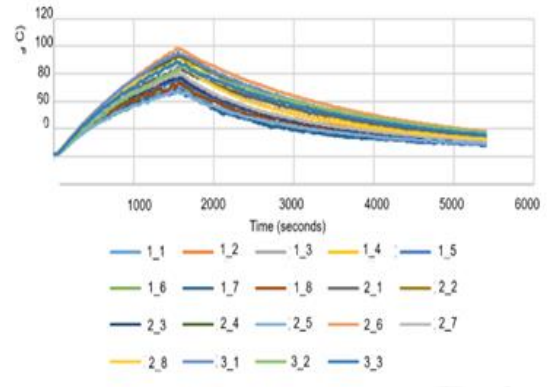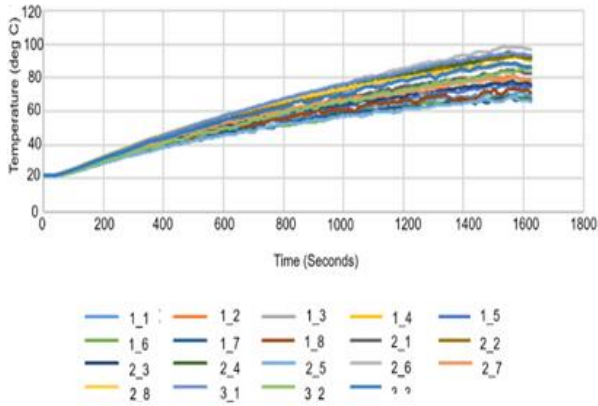
Test 01
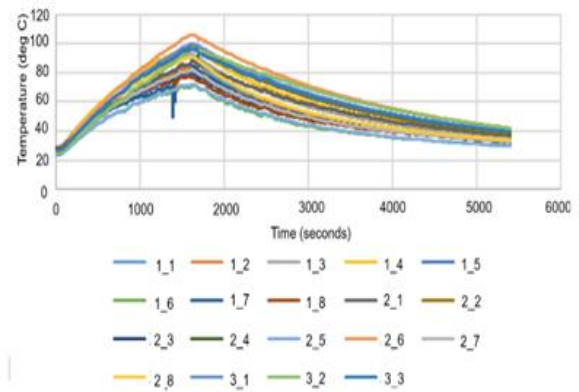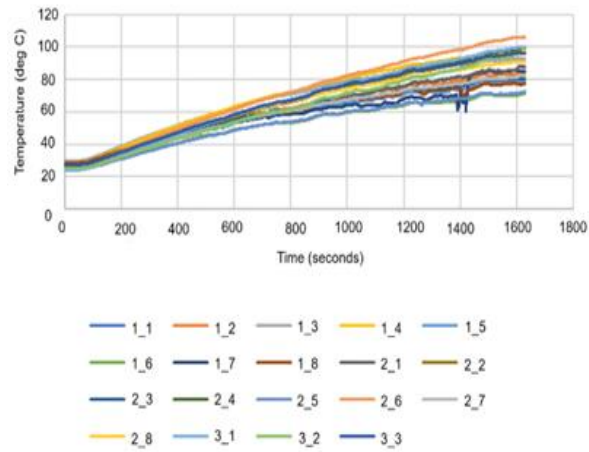
Test 02
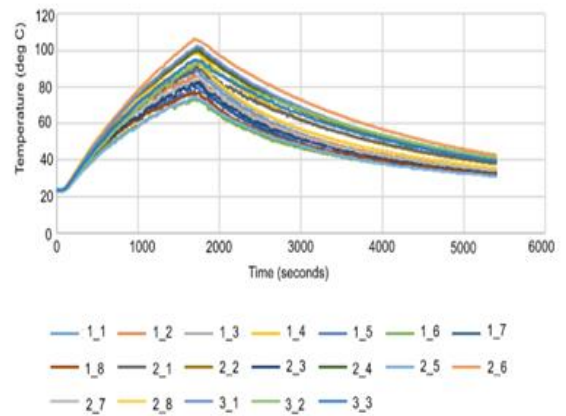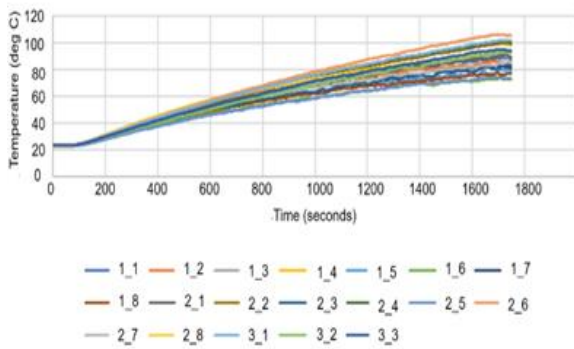
Test 03

- Annex 2
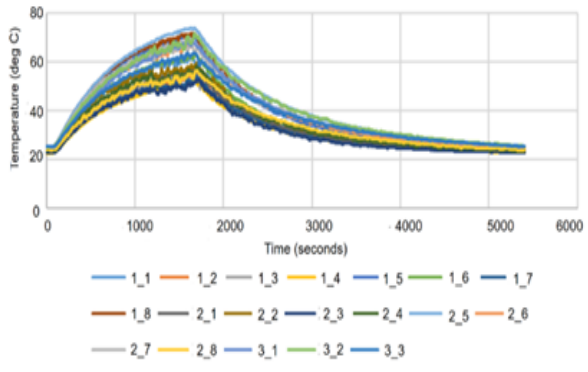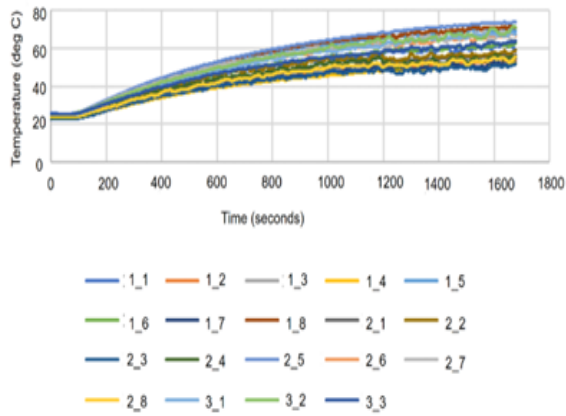
Test 01
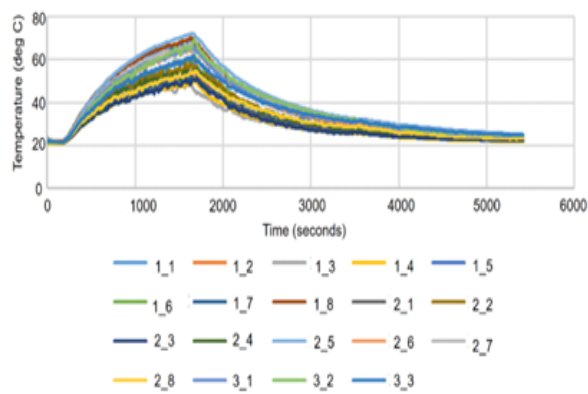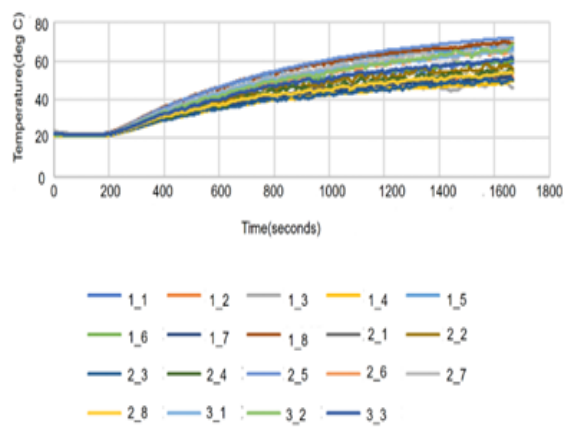
Test 02
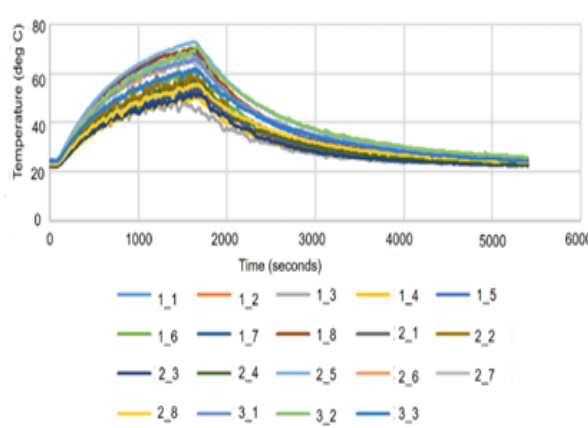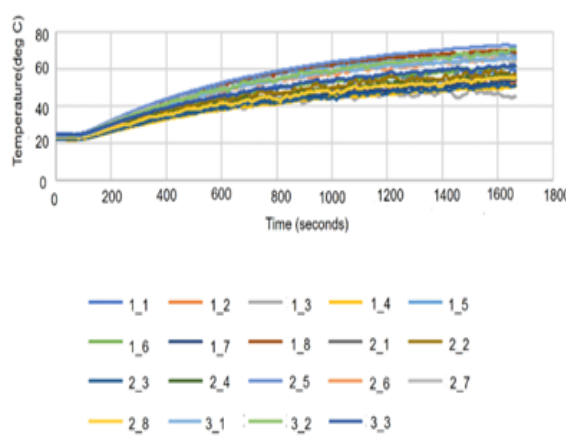
Test 03

- Annex 3
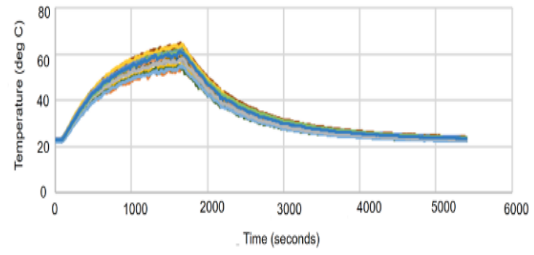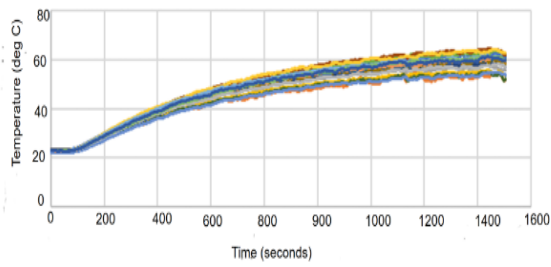
Test 01
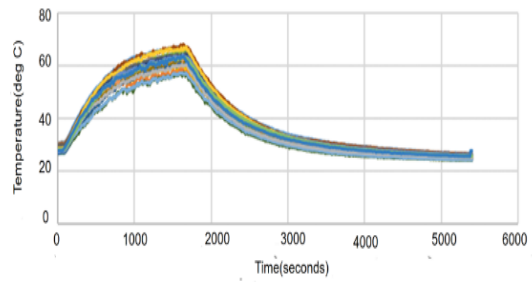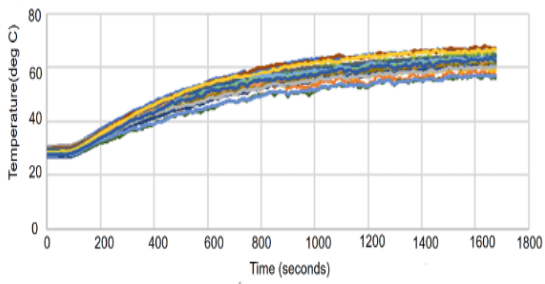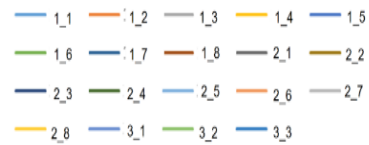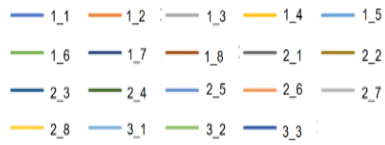
Test 02
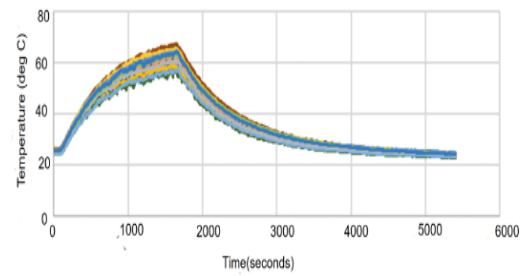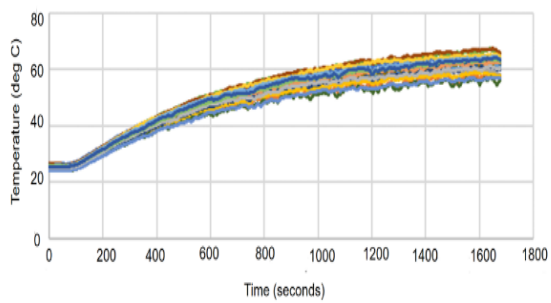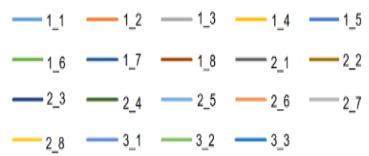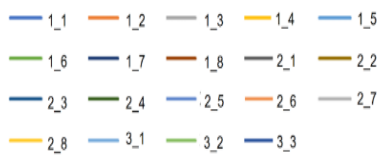
Test 03
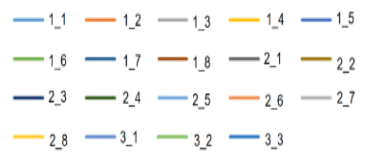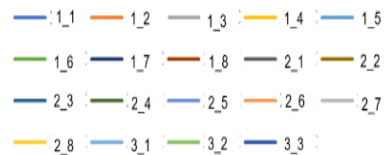
- Annex 4
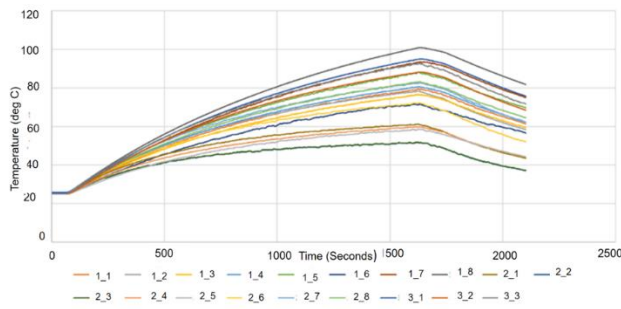
Average experimental results for no gap scenario
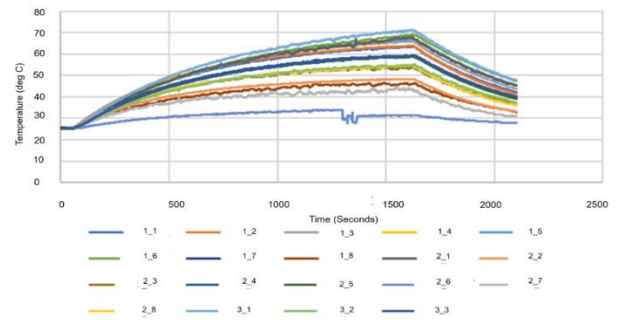
Average experimental results for standard gap scenario
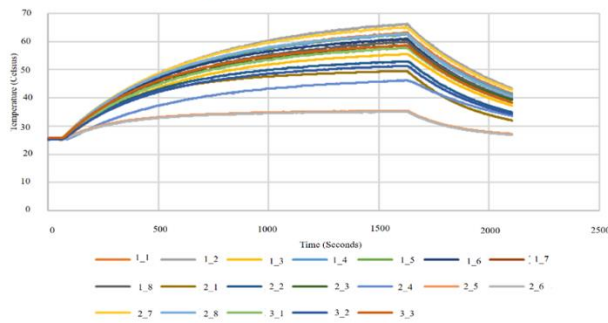
Average experimental results for double gap scenario

- Annex 5
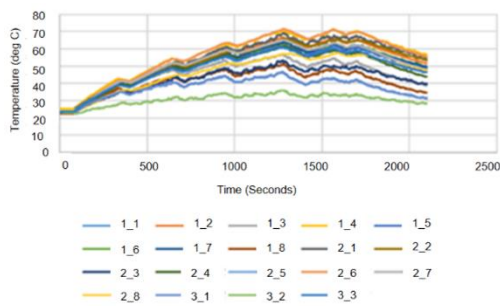
Experiment 01
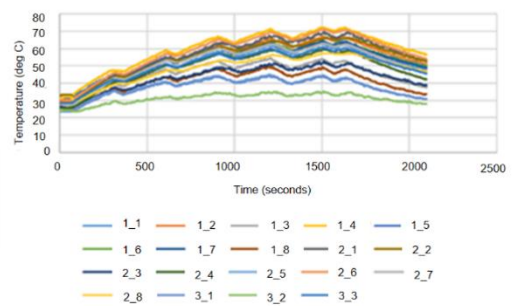
Experiment 02
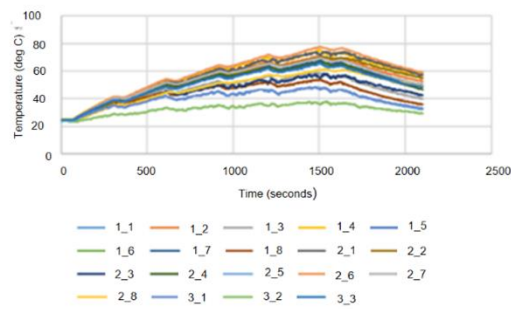
Experiment 03

No gap scenario

- Annex 6
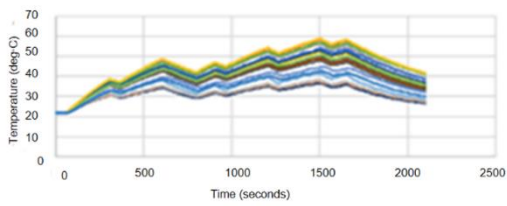
Experiment 01
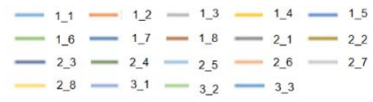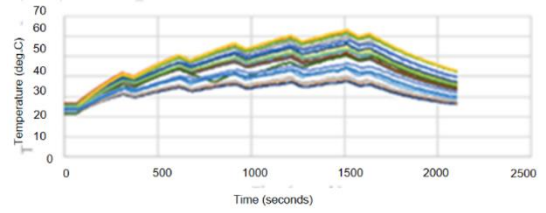
Experiment 02
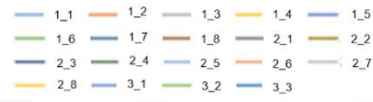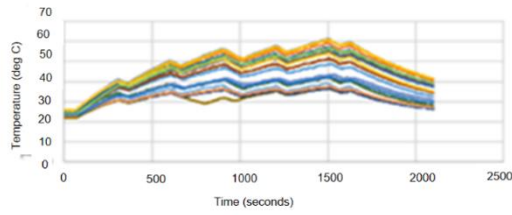
Experiment 03

Standard gap scenario

- Annex 7
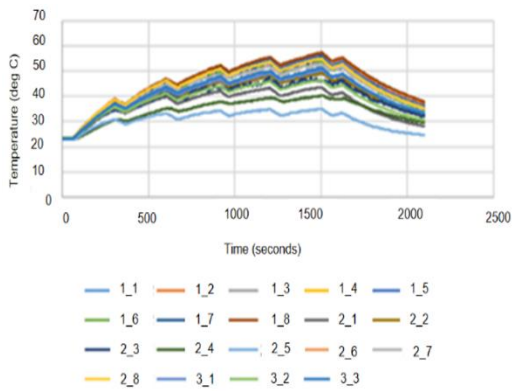
Experiment 01
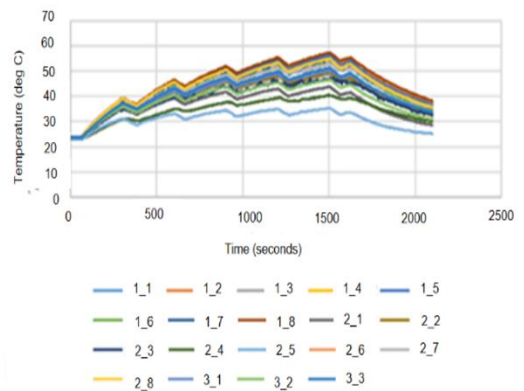
Experiment 02
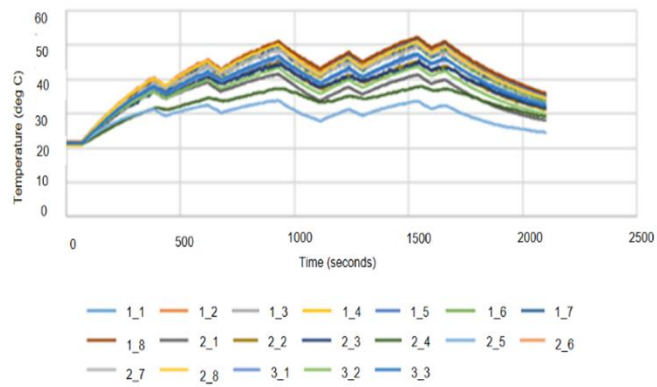
Experiment 03

Double gap scenario

- Annex 8
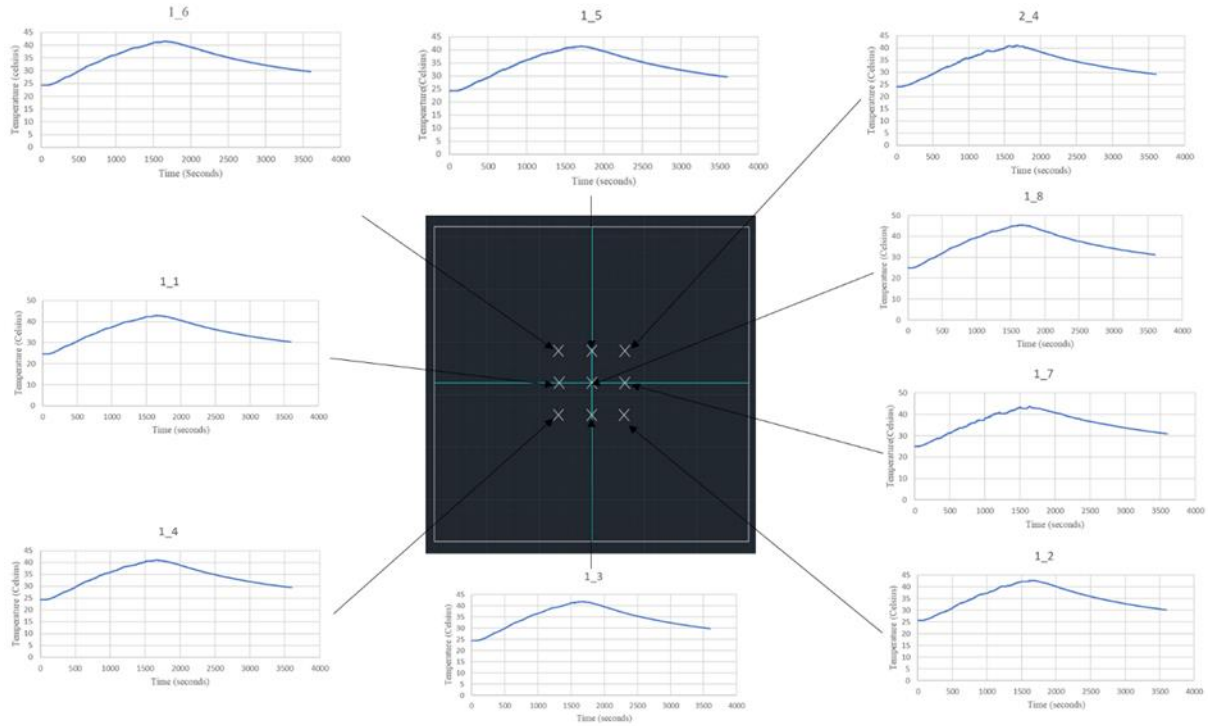
Inner side surface temperature variation (Orientation 1)
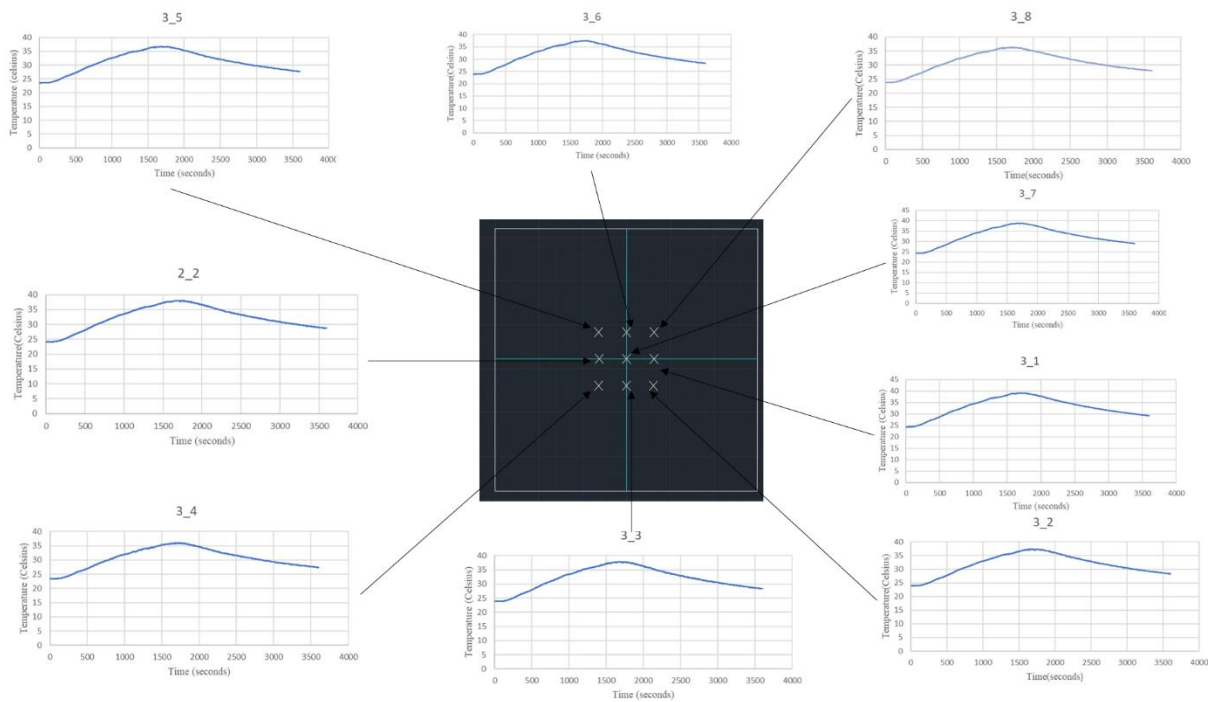
Outside surface temperature variation (Orientation 01)
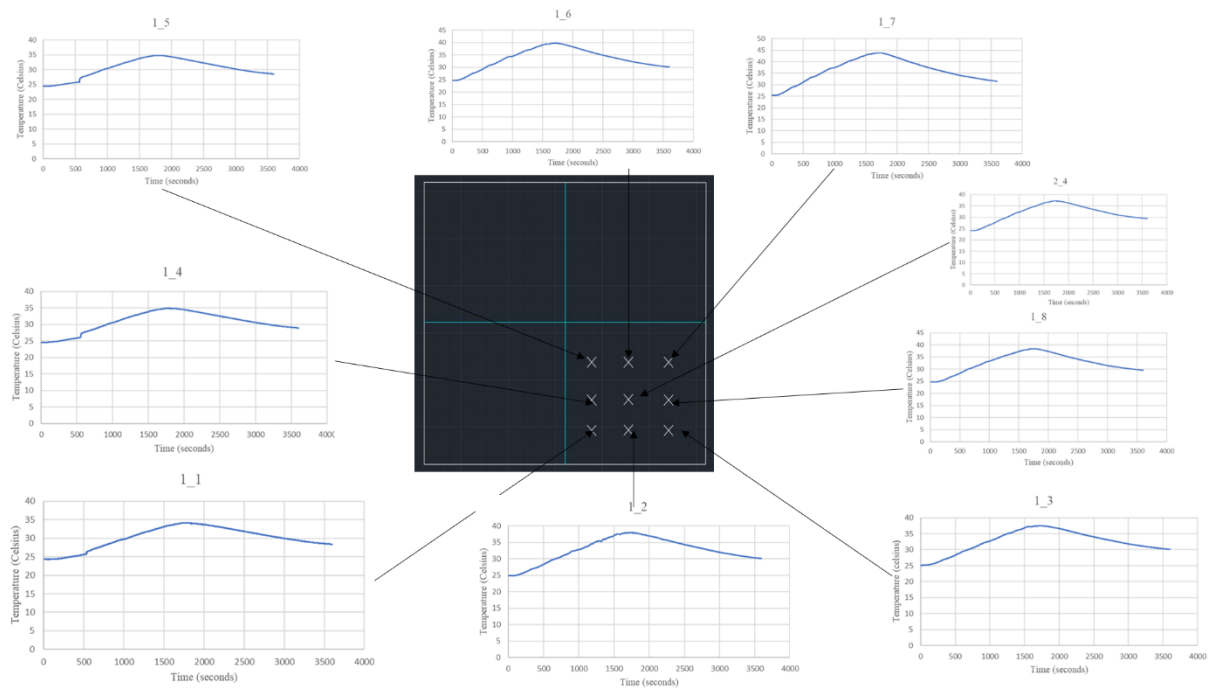
Inside temperature variation (Orientation 2)
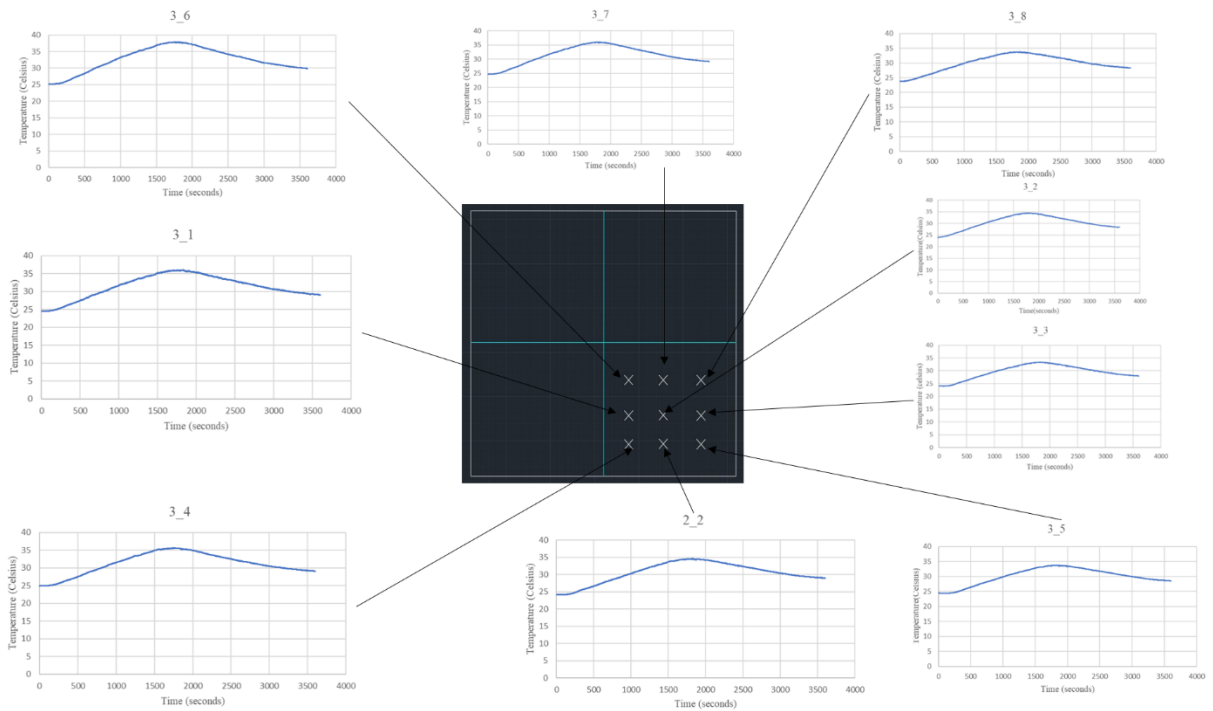
Outside temperature variation (Orientation 2)
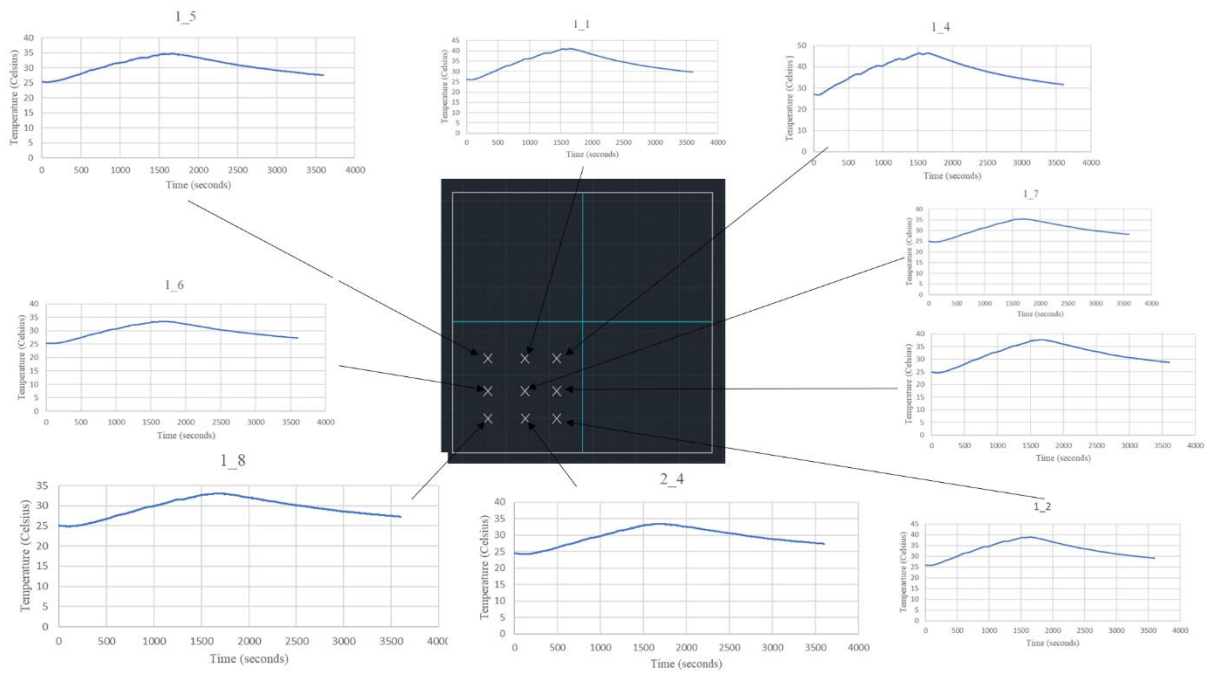
Inside temperature variation (Orientation 3)
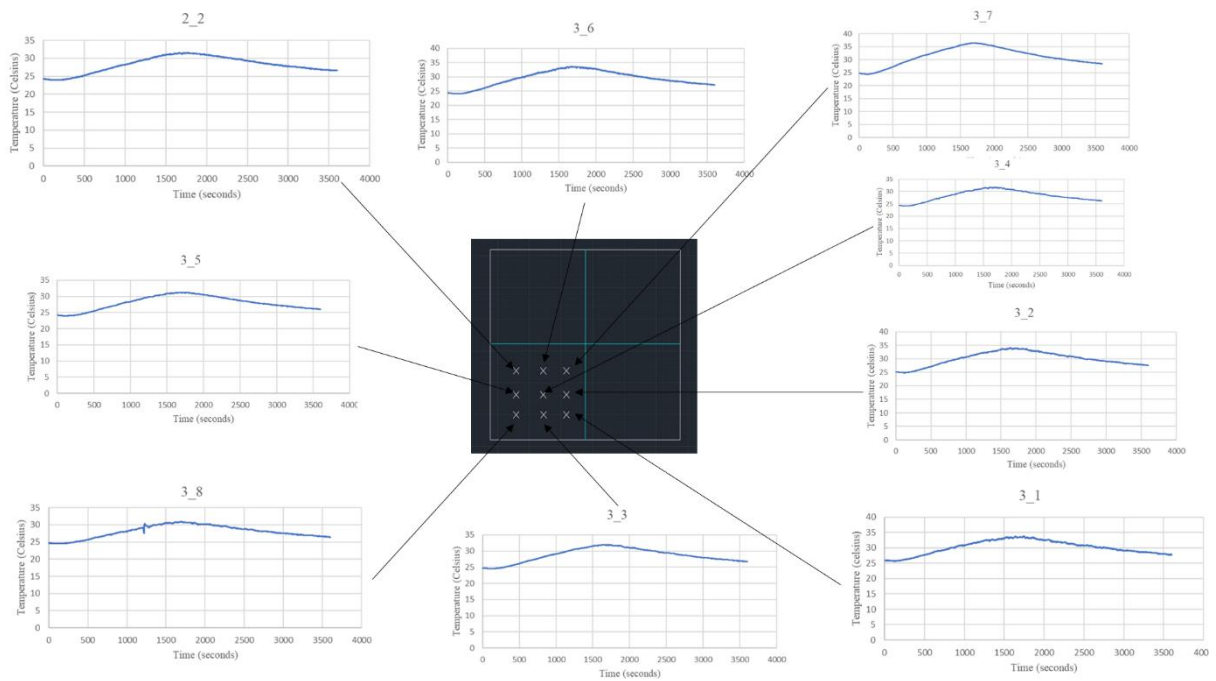
Outside temperature variation (Orientation 3)
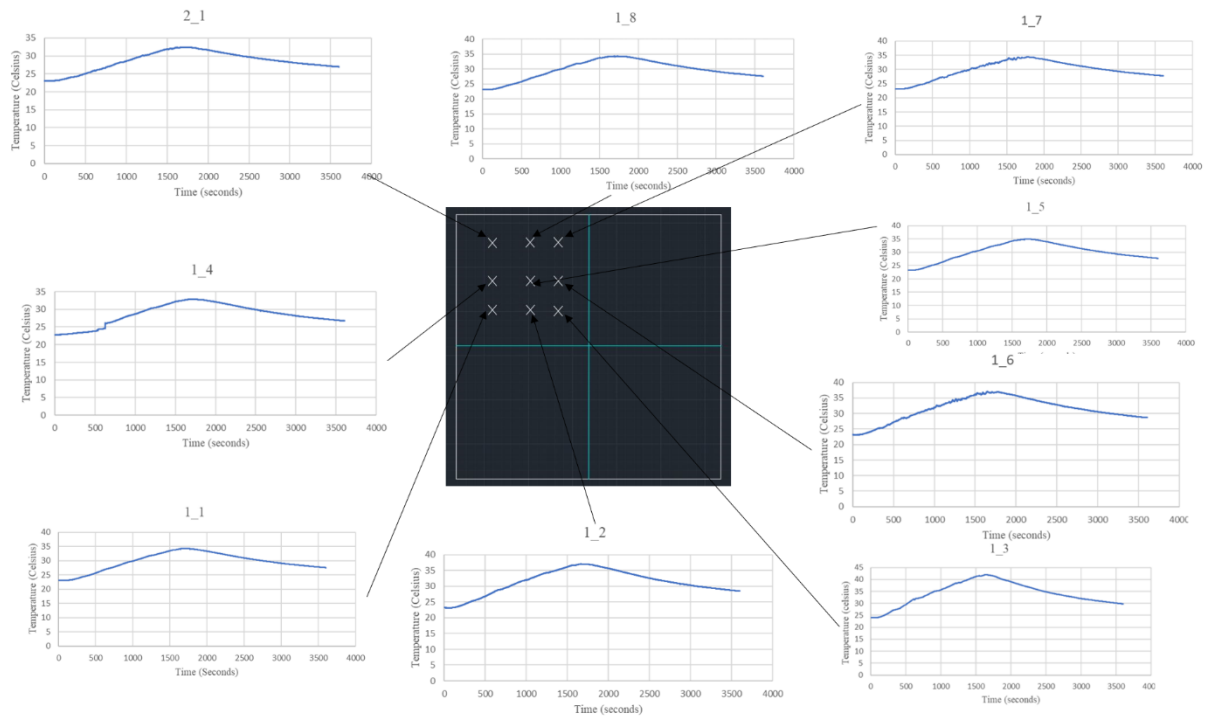
Inside temperature variation (Orientation 4)
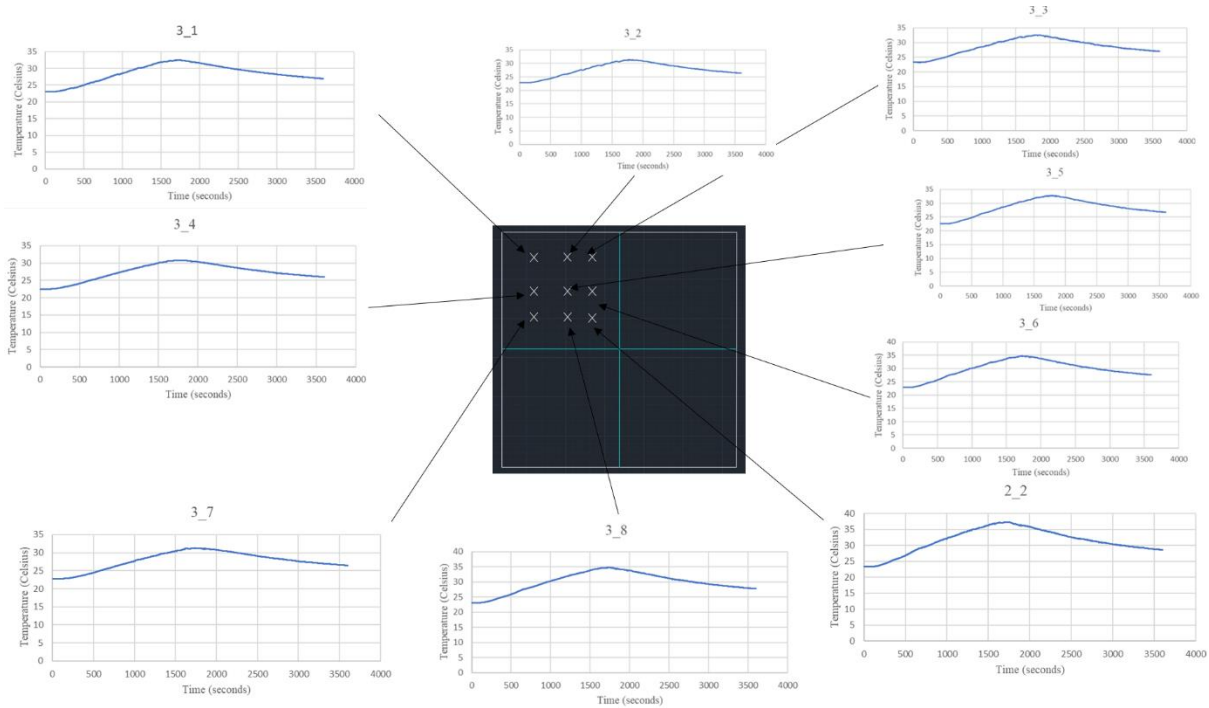
Outside temperature variation (Orientation 4)
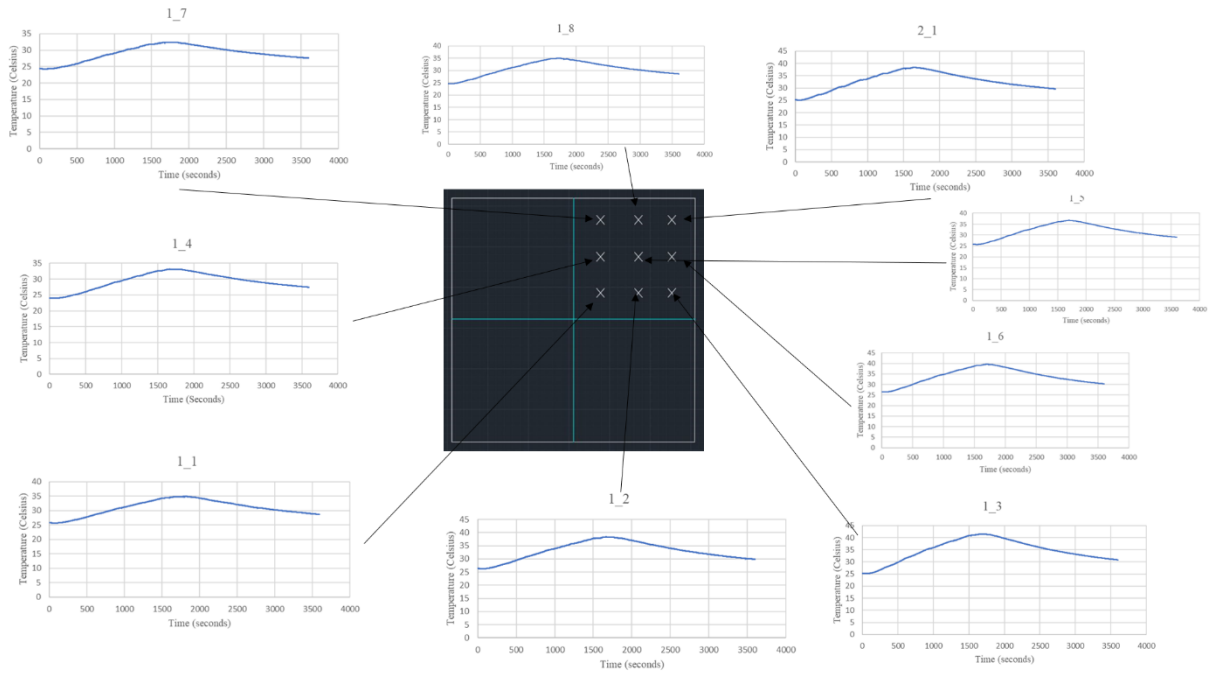
Inside temperature variation (Orientation 5)
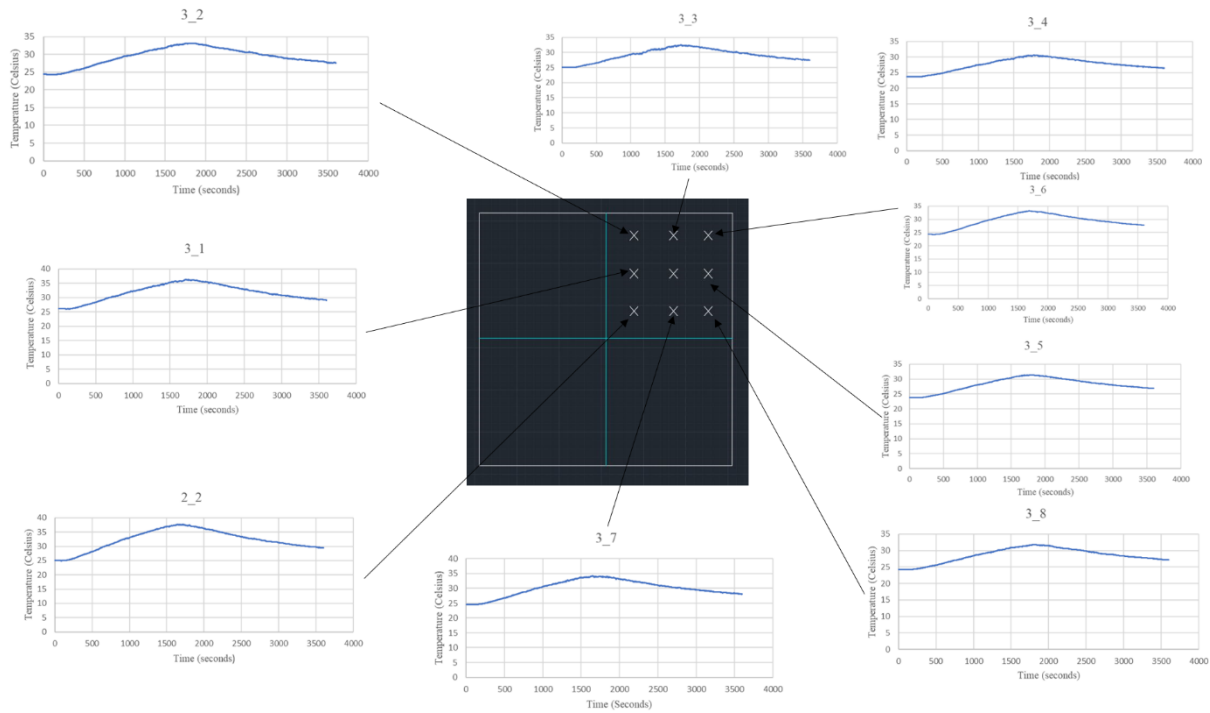
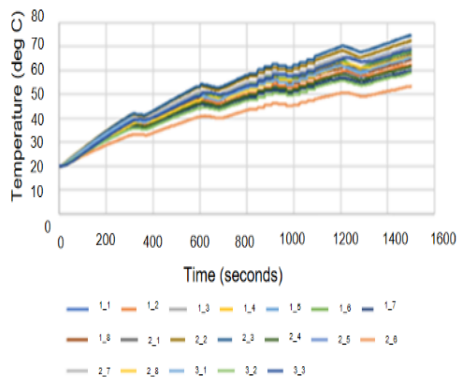Outside temperature variation (Orientation 5)
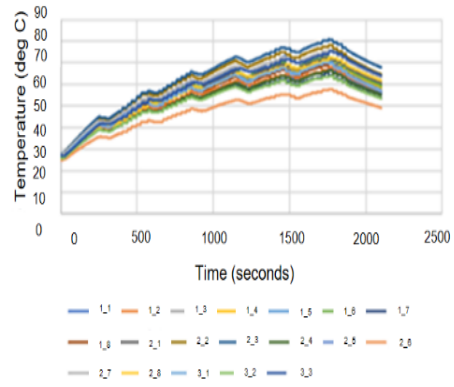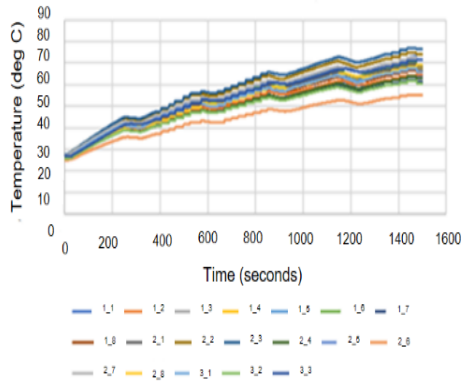
- Annex 9
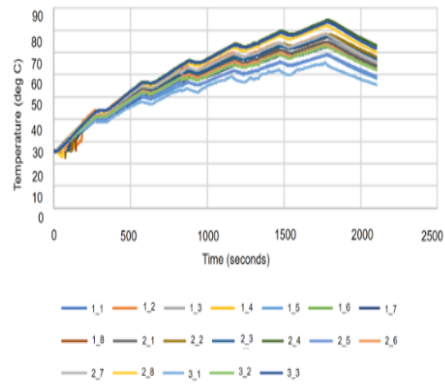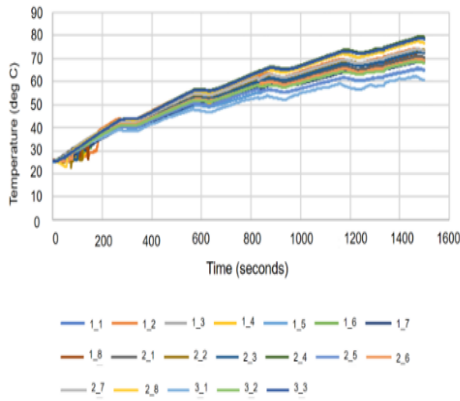
Enclosure 01
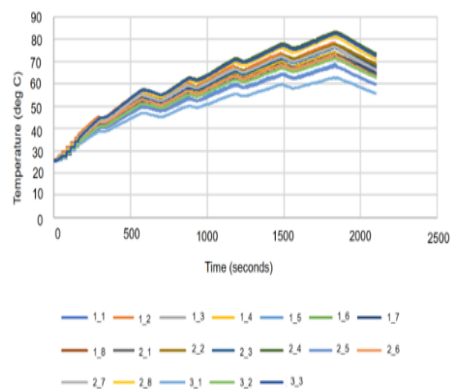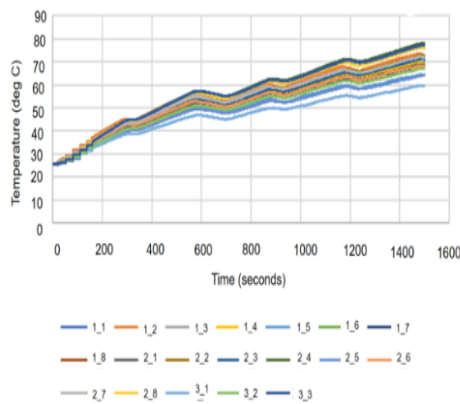
Enclosure 02
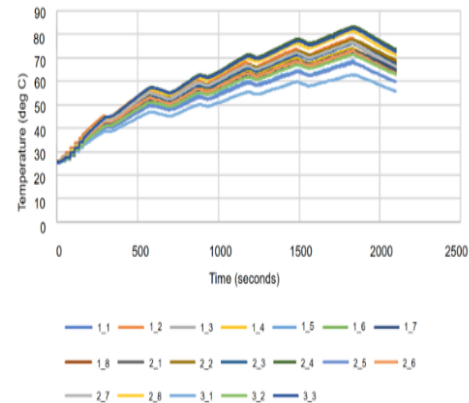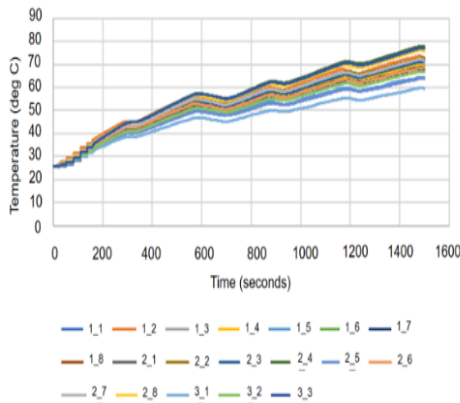
Enclosure 03

- Annex 10
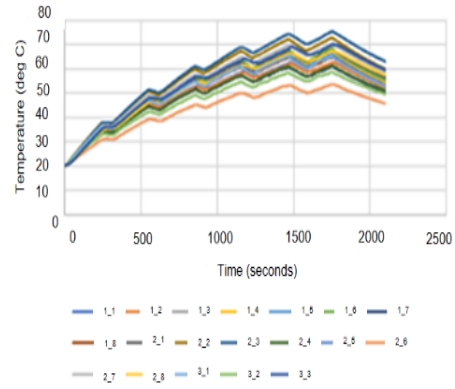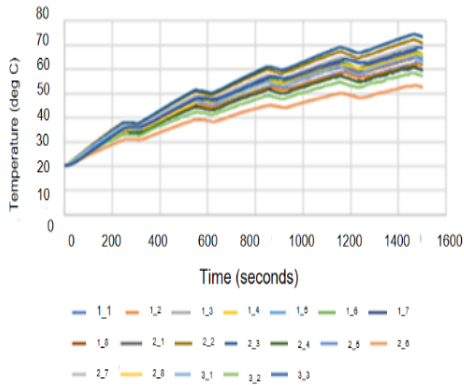
Enclosure 1

Enclosure 2

Enclosure 3